Université de Lille

iemn
Institut d'Electronique, de Microélectronique et de Nanotechnologie
UMR CNRS 8520

Université de Lille

École doctorale **ED Régionale SPI 072**
Unité de recherche **IEMN UMR CNRS 8520**

Thèse présentée par **Stephanie Signe Mamba**
Soutenue le **21 février 2018**
En vue de l'obtention du grade de docteur de l'Université de Lille

Discipline **Electronique**
Spécialité **Micro and Nano-technologies, Acoustics, Telecommunications**

Titre de la thèse

The dynamics of liquid plugs in synthetic networks under cyclic forcings : towards understanding and treatment of respiratory diseases

Thèse dirigée par	Farzam Zoueshtiagh	directeur
	Baudoin Michael	co-directeur

Composition du jury

Rapporteurs	Isabelle Cantat	professeur à l'Université de Rennes
	Anne Juel	professeur à l'University of Manchester
Examinateurs	Vincent Senez	directeur de recherche au CNRS
	Julien Favier	MCF HDR à l'Aix Marseilles Université
Directeurs de thèse	Farzam Zoueshtiagh	professeur à l'Université de Lille
	Baudoin Michael	professeur à l'Université de Lille

Université de Lille

iemn
Institut d'Électronique, de Microélectronique et de Nanotechnologie
UMR CNRS 8520

Université de Lille

École doctorale **ED Régionale SPI 072**
Unité de recherche **IEMN UMR CNRS 8520**

Thèse présentée par **Stephanie Signe Mamba**
Soutenue le **21 février 2018**
En vue de l'obtention du grade de docteur de l'Université de Lille
Discipline **Electronique**
Spécialité **Micro and Nano-technologies, Acoustics, Telecommunications**

Titre de la thèse

De la dynamique de bouchons liquides dans les réseaux synthétiques soumis à des forçages cycliques au diagnostic et traitement de maladies respiratoires

Thèse dirigée par	Farzam Zoueshtiagh	directeur
	Baudoin Michael	co-directeur

Composition du jury

Rapporteurs	Isabelle Cantat	professeur à l'Université de Rennes
	Anne Juel	professeur à l'University of Manchester
Examinateurs	Vincent Senez	directeur de recherche au CNRS
	Julien Favier	MCF HDR à l'Aix Marseilles Université
Directeurs de thèse	Farzam Zoueshtiagh	professeur à l'Université de Lille
	Baudoin Michael	professeur à l'Université de Lille

The Université de Lille and the IEMN UMR CNRS 8520 neither endorse nor censure authors' opinions expressed in the theses: these opinions must be considered to be those of their authors.

Keywords: two phase flow, cyclic forcings, taylor flow, slug, bolus, capillary tube, synthetic networks, airways reopening

Mots clés : écoulement diphasiques, forçages périodiques, bouchons liquides, bolus, tubes capillaires, réseaux synthétiques, réouverture des voies respiratoires

Life is an experimental journey
undertaken involuntarely.

Fernando Pessoa

Science never solves a problem
without creating ten more.

George Bernard Shaw

It is easier to disintegrate an atom
than a prejudice.

Albert Einstein

The dynamics of liquid plugs in synthetic networks under cyclic forcings: towards understanding and treatment of respiratory diseases

Abstract

Breathing is one of the most vital mechanism for humans. Indeed, one can live a few days without eating or drinking, but only few minutes without breathing. Owing to the complexity of the respiratory system, the mechanism of breathing is not well understood, especially in pathological conditions when airways are obstructed by mucus. The presence of liquid plugs resulting from the accumulation of mucus in the bronchial tree is a characteristic of genetic diseases like cystic fibrosis or chronic diseases like asthma or chronic bronchitis. Thus, understanding the dynamics of these plugs during the breathing cycle is essential to improve our understanding of those diseases. In this thesis, we study experimentally and theoretically, the dynamics and rupture of liquid plugs under unidirectional and cyclic forcing in a rigid capillary tube. We develop a reduced dimension model, which quantitatively reproduces the observed dynamics, unveil the underlying physics and in particular the sources of the plug instability leading to its rupture. From this model, we are able to derive the critical pressure magnitude required to reopen obstructed pathways. In addition to the study of cylindrical tubes, we investigated the cyclic dynamics of liquid plugs in rectangular channels, a geometry of the utmost interest for microfluidic systems. In this case, we show that under cyclic pressure forcing, two regimes can be observed depending on the values of the capillary number: one leading to the rupture of the plug and one to stable cyclic oscillations. Finally, in the last part of this work, we study experimentally the cyclic forcing of liquid plugs in tree structures mimicking the geometry of intermediate generation of the lung. These preliminary results show that plugs not ruptured during the first half cycle persist in the airways for a long time and oscillate until their rupture. To conclude, we must underline that the initial objective of this thesis was not to achieve a realistic description of pathological flows in the lungs, but only to develop some fundamental solid building blocks that might contribute to this goal in the future.

Keywords: two phase flow, cyclic forcings, taylor flow, slug, bolus, capillary tube, synthetic networks, airways reopening

De la dynamique de bouchons liquides dans les réseaux synthétiques soumis à des forçages cycliques au diagnostic et traitement de maladies respiratoires

Résumé

La respiration est un mécanisme essentiel de survie chez les humains. En effet, si nous pouvons survivre quelques jours sans manger et boire, nous ne pouvons survivre que quelques minutes sans respirer. Le système respiratoire est extrêmement complexe de par sa structure fractale qui induit des physiques très différentes entre les voies proximales et distales. Il n'existe à l'heure actuelle aucune modélisation réaliste du système pulmonaire en particulier dans des conditions pathologiques où les voies sont obstruées par des bouchons de mucus. Ces bouchons liquides caractéristiques de certaines maladies comme la mucoviscidose, les bronchites chroniques ou l'asthme résultent de l'accumulation de mucus dans les voies pulmonaires. Comprendre les mécanismes à l'œuvre lors de l'écoulement de ces bouchons lors d'un cycle respiratoire est donc primordial pour améliorer notre compréhension et le traitement de ces pathologies. Nous présentons dans cette thèse une première étude théorique et expérimentale de la dynamique de ces bouchons liquides dans des tubes capillaires rigides soumis à des forçages unidirectionnels et cycliques. Nous avons développé au cours de ce travail un modèle simplifié permettant de reproduire quantitativement les dynamiques observées, de comprendre la physique sous-jacente et en particulier d'identifier les sources d'instabilités qui entraînent la rupture d'un pont liquide. Ce modèle nous a permis de déterminer les pressions critiques nécessaires à la réouverture des voies pulmonaires. Ensuite, nous nous sommes intéressés à la dynamique des ponts liquides dans des tubes rectangulaires, la géométrie la plus communément rencontrée en microfluidique. Dans cette géométrie, nous avons identifié de nouveaux régimes qui n'apparaissent pas dans les géométries cylindriques, et en particulier un régime d'oscillation stable sous forçage en pression périodique. Enfin nous nous sommes intéressés à la dynamique cyclique de ponts liquides dans des réseaux synthétiques en arbres. Nos premiers résultats montrent que les ponts qui ne sont pas détruits lors du premier demi-cycle persistent très longtemps dans les voies et oscillent de manière cyclique dans une génération jusqu'à leur rupture. Pour conclure il est important de souligner que l'objectif initial de cette thèse n'était pas d'aboutir à une modélisation réaliste des écoulements pulmonaires dans des conditions pathologiques, mais simplement d'apporter des briques fondamentales solides qui pourraient y contribuer dans le futur.

Mots clés : écoulement diphasiques, forçages périodiques, bouchons liquides, bolus, tubes capillaires, réseaux synthétiques, réouverture des voies respiratoires

IEMN
Laboratoire central – Cité scientifique - Avenue Poincaré – CS 60069 – 59652 Villeneuve d Asca Cedex – France

Thanks

I wish to express my sincere gratitude to my advisors Michael Baudoin and Farzam Zoueshtiagh for supporting me and for the wise advises they gave me during my journey in the wonderful world of research.

Besides my advisors, I wish to express my gratitude to the committee members for the ideas and feedbacks. The discussions we had, gave me precious clues to improve this work.

A special thank goes to my parents: Signe Louis and Tsimbo Caroline for calling me everyday and encouraging through the most difficult times. I would also like to thank my brothers and sister: Signe Patricia, Signe Guy, Signe Louis, Signe Michel and Signe Arsene for supporting me throughout writing this thesis.

I would like to thank all the members of the AIMAN/FILMS team for the stimulating discussions and particularly for the jokes.

A special thank to Dr. Denis Bitouzé who provided the package Yathesis that was used to write this thesis.

Finally, I would like to thank very warmly some precious friends who contributed in their own way to this achievement: Josephine Fotsing, Barbara Kmer, Ralph Sindjui, Stephane Fotso, Alain Bruno Fadjie, Jean Claude Gerbedoen, Peter Favreau, Maxime seeleuthner, Manon Benedito, Frederic Mebenga, Philemon Nogning, Yvan Ngassa, Christian Kamdem, Cesaire Fotsing, Ottou Thierry...

Summary

General introduction

Basic features of the mechanism of breathing

The human respiratory system is a biological system made of 3 major parts: (i) the lungs that are pair (left and right lung) of large, air-filled organs found in the thoracic cavity of the chest, (ii) the airways, which include the nose, mouth, pharynx, larynx, trachea, bronchi, and bronchioles and (iii) the muscles of respiration in which the principal role is played by the diaphragm [1]. This

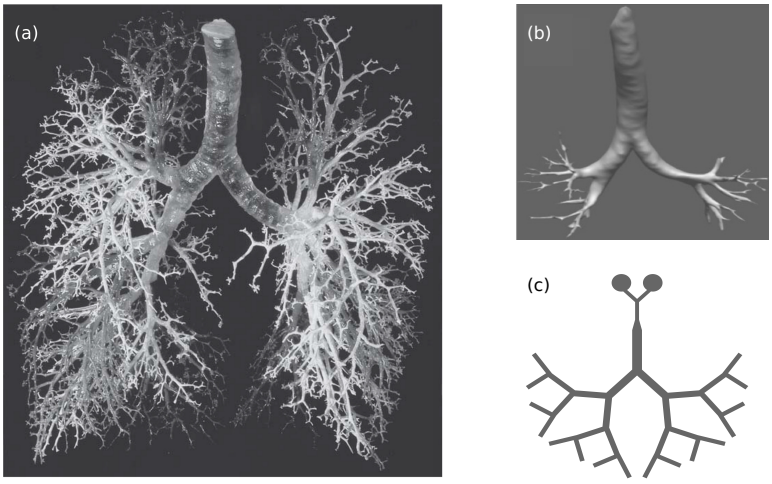

Figure 1 – Geometry of the human lung:
a) Cast of a human lung. The alveoli have been removed allowing the conducting airways to be seen [2].
b) 3D reconstruction of the first five bronchial generations of a woman lung using computerized tomography for realistic numerical simulations [3].
c) 2D symmetric model of five bronchial generations made of PDMS used for experiments.

complex system made up of organs, muscles and tissues is essentially used for gas exchange but also plays roles in the metabolization of physiological compounds, filtering the unwanted materials from the circulation, and acts as a reservoir for blood [4, 5]. The process of gas exchange in which oxygen O_2 is delivered from the lungs to the bloodstream, and carbon dioxide CO_2 is eliminated from the bloodstream to the lungs is only possible by the process of breathing, consisting of repetitive cycles of inspiration and expiration of air from the nose to about 500 millions of small alveoli sacs at a frequency of 12 to 18 breaths per mins [2]. It is therefore a cyclic process that occurs through the lung airways (see Fig. 1). Several factors as the weight, sex, age, activity and the health can affect lung capacity and therefore lung volumes during breathing. Average values of the lung volumes in normal healthy female and male adults are found in Ganong [6]:

- The tidal volume (TV): volume of air that moves into and out of the lungs during quiet breathing $0.5l$.
- The inspiratory Reserve Volume (IRV): additional volume of air that can be forced into the lungs after you breathe in the tidal volume $1.9 – 3.1l$.
- The expiratory reserve volume (ERV): additional volume of air that be be forced out at the end of a normal expiration $0.7 – 1.2l$.
- The residual volume (RV): volume of air that remains in your lungs after you force out as much as possible $1.1 – 1.2l$.
- The total lung capacity (TLC=TV+IRV+ERV+RV): the maximum volume of air that you breathe in and out of your lungs $4.2 – 6l$.

The mechanism of breathing involves not only the volumes of air that moves in and out of the lung during breathing but also the pressures that are necessary for airflow. Flow of air in the pulmonary airways occurs by bulk flow along pressure gradients created in between the atmosphere and the alveoli (alveolar pressure equal to the atmospheric pressure when there is no airflow). During a quiet breathing, these pressure gradients are created by the contraction of the

diaphragm and the abdominal muscles during inspiration and the elastic recoil of the lungs during expiration (see Fig. 2).

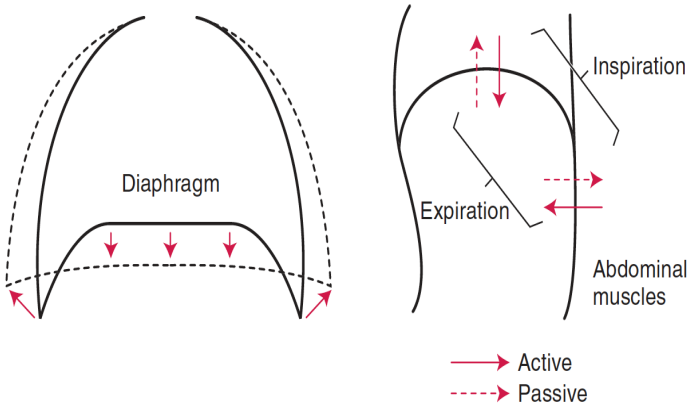

Figure 2 – Mechanics of breathing [2] .

Inspiration is an active process that starts with the contraction of the diaphragm by $1 - 1.5cm$ which increases the volume of chest by $250 - 350cm^3$. This increase in volumes lead to a decrease of the alveolar pressure below the atmospheric pressure (negative pressure) due to Boyle's law ($PV = cst$). Bulk flow of air can then occur from places of high pressure (atmosphere) to places of low pressure (lung) until the pressures get equals at the end of the inspiration. Expiration is conversely a passive process in which the muscles of respiration are relaxed because of the elastic recoil of the lung, leading to opposite pressure gradients until the pressure inside the lung and the atmosphere are equal [2]. Simulations of the alveolar pressure using flow resistance models formulation for the respiratory system [7, 8] led to Fig. 3 in which the zero is in reference to the atmospheric pressure.

The other functions of breathing include: (i) the physiological regulation, (ii) providing mechanisms for expressions and emotions, (iii) the balance of the nervous-system.

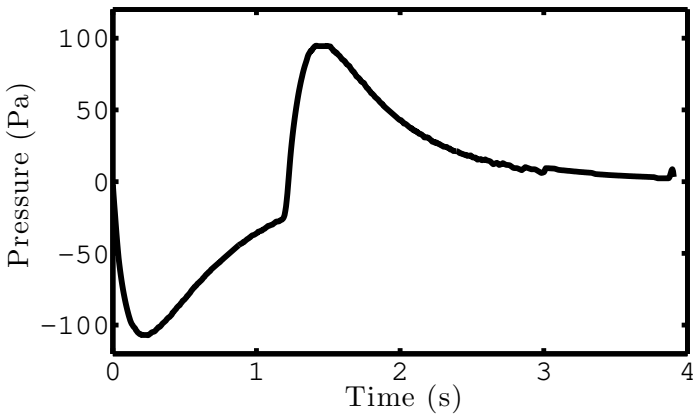

Figure 3 – Alveolar pressure during a quiet breathing cycle [8] .

Lung airways: a complex network of capillaries

Geometrical description

Lung airways consist in a network of branching pipes (Fig. 1) that display a broad range of sizes and physical interactions [9]. To fulfill its principal function of mass transport to and from the body, lungs adopt a tree like structure. This configuration is suitable for a minimal volume (about (5 – 6)l in adult), but a very large interface at its extremity for diffusional gas exchange between air and blood (about $(70 - 100m^2)$) [9, 10, 11, 12, 2]. There are more than 20 generations of branching in the lungs [10, 13, 14]. This complex network can be divided into two main regions (see Fig. 4):

- The conducting airways (generations 0–16): consisting of the trachea, the bronchi and the bronchioles. This system of connected ducts acts as low work air conduits, bringing air to the respiratory region.

- The respiratory or gas-exchanging region (generations 17-23): In this region, the diameter of the ducts is less than $0.6mm$ and alveoli start to appear in bronchioles. The number of alveoli increases as it goes further down to the lung and forms at the end section of the airways (generation 23) a clusters where gas-exchange with the blood vessels occurs by diffusion.

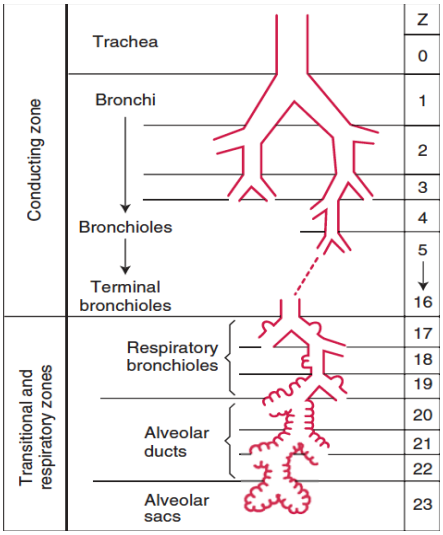

Figure 4 – Ideal model of the human airways adapted by [2] from [15]

The lung airway walls are made of elastic fibers of thickness about 10% their radius with a Young's modulus $E = 6.10^3 Pa$ and a Poisson's ratio $\nu = 0.49$ [16] leading to a very flexible material. However, variations in the physical properties the airways generations are found. While the trachea and bronchi have cartilaginous walls, those disappear in the bronchioles and alveoli where they are replaced by smooth muscles [1].

The most commonly used model of lung airways geometry is derived from measurements made by Weibel [10] from which he constructed a symmetrical model using means measurements of the airways tree in which all the airways in a generation are identical and divide dichotomously (see Fig. 4). Another model less used but more complete was proposed by Horsfield [17, 13, 14], who gave a full description of an asymmetric lung by measuring the lengths, diameters and the branching angle in all the generations on a cast of a male lung. He found quite similar values to the one of Weibel except that he counted 24 instead of 23 generations proposed by Weibel and found a number of terminal bronchioles less than half the predictions of Weibel which correspond to only one generation of dichotomous branching. Despite these discrepancies, the model of Weibel is still the most widely used since it offers a mathematical description of the evolution of the generations of the airways. Table 1 present values of this model

as well as Reynolds number ($Re = \rho V l/\mu$) associated with flows during a quiet breathing ($0.5l/s$) and vigorous breathing ($2l/s$) as reported by Pedley [9].

Generation	Diameter $d(cm)$	Length $L(cm)$	Number of alveoli(10^5)	Re
Trachea	1.8	12	0	2325-9300
1	1.22	4.76	0	1719-6876
2	0.83	1.9	0	1281-5124
3	0.56	0.76	0	921-3684
4	0.45	1.27	0	594-2376
5	0.35	1.07	0	369-1476
10	0.13	0.46	0	32-127
15	0.066	0.2	0	1.9-7.6
20	0.045	0.083	210	0.09-0.37

Table 1 – Characteristics of the airway tree and Reynolds numbers associate with two flow velocities in the airway [10, 9].

The flow in the trachea is turbulent and becomes more laminar as we go further in the bronchial tree leading to different physical interactions and therefore different models to study the airflow [12]. Using the data of this model, the characteristics of a typical symmetrical bifurcation in the respiratory region reported in [9, 18] was found to be: diameter ratio between daughter and mother branch $d_n/d_{n+1} \sim 0.79$, length to diameter ratio in a generation $L/d = 3.5$ allowing the construction of a fractal branching tree [19]. As for the mean branching angles α, they are obtained from the data of Horsfield [17] and lie between 64° in airways of diameter greater than $0.4cm$ to 100° in airways of diameter less than $0.1cm$.

It is worth mentioning that maximal physical efficiency cannot be the only criterion in the design of a bronchial tree since it is shown by Mauroy & al. [20] that an optimized fractal bronchial tree may be dangerous. This can explain the natural asymmetry of the lung where the right lung is bigger than the left one which shares space with the heart. This asymmetry propagates in the bronchial distribution creating a safety margin while keeping the physiological robustness of the lung.

Lung airway resistance

Airway resistance R is the force opposing air flow in the airway and can be expressed analogously to Ohm's Law as the pressure difference between the alveoli and the mouth or the nose, ΔP, per unit of airflow Q.

$$R = \frac{\Delta P}{Q} \tag{1}$$

Since the lung airways consist in connected cylindrical pipes, the pressure difference can be expressed in terms of Poiseuille's law (in generations where the flow is laminar):

$$\Delta P = \frac{128 \mu L Q}{\pi d^4} \tag{2}$$

With μ the dynamic viscosity, L and d respectively the length and diameter of a pipe. Therefore, the airways resistance can be expressed in terms of the diameter of the pipe:

$$R = \frac{128 \mu L}{\pi d^4} \tag{3}$$

This simple estimation of the airways resistance shows that if the diameter of the airway is halved for example as a result of asthma [21, 22] or airway obstruction by mucus [23, 24], the resistance will increase by a factor 16. In this case, the respiratory muscles will need to generate much more pressure to overcome this resistance and produce adequate airflow. Thus, diseases affecting the respiratory tract can increase dramatically airway resistance. However, most airway resistance resides in the upper airways (80%) compared to less that 20% in the airways of diameter less than $2mm$ which is rather counter-intuitive if we assume Poiseuille's law. This can be explained by the dichotomous division at each generation leading to a rapid increase of the number of bronchi and as a consequence, an increase of the total cross sectional area when we go further in the bronchial tree, thus reducing a lot the total resistance contribution of that region [2].

Mucus

The human lungs secrete a liquid known as the mucus which coats the airway walls and protects it against foreign material. This protection is essential since millions of particles flow through the airways every day [25]. These particles can be dangerous if they are in contact with the airways wall or pass through the blood system. The role of the mucus is to trap these particles and with the help of the airways cilia, move them out of the lung. The mucociliary system therefore represent the first and major protection of the airway [2].

Properties

Airway mucus is a non-homogeneous mixture containing glycoproteins $\sim 2\%$, proteins 1%, lipids 1%, inorganic salt 1%, DNA 0.02% and cellular debris in a watery matrix 95% secreted from the airways [26, 27, 28]. Mucus is a gel layer that has both solid elastic and viscous fluid properties, floating on a Newtonian layer of low viscous fluid. In addition to its viscoelastic properties [29, 30, 31], the non-Newtonian mucus exhibits other properties as Bingham plastic of finite yield stress ($\sim 500 - 600 dyn.cm^{-2}$) [32, 33], shear-thinning, and thixotropy [34]. The mucus layer is no uniformly distributed in the airway tree. In the conducting airway, the mucus thickness is on the order of $(5 - 10)$ microns [9, 35], while in the respiratory region, it is approximately $(2 - 4\%)$ of the airway radius [36, 37]. The properties of mucus also changes as we go further in the bronchial tree, becoming Newtonian in the respiratory region because the concentration of proteins that are responsible for the non-Newtonian properties of the mucus reduces [18, 12]. This Newtonian mucus is typically characterized by a surface tension $\sigma = 20 mN.m^{-1}$, a dynamic viscosity $\mu = 10^{-3} kg.m^{-1}.s^{-1}$ and a density $\rho = 10^{3} kg.m^{3}$ [38, 16].

Production and transport

The goblet cells together with the submucosal glands produce the mucus of the conducting airways [39, 40], at a rate of $\sim 10 mL/day$ in a adult normal lung [41]. The mucus that is secreted needs to be transported out of the airways towards the stomach where it is destructed: this is known as mucociliary transport. The

transport of mucus through the airways is done by the activity of moving cilia [29, 42].

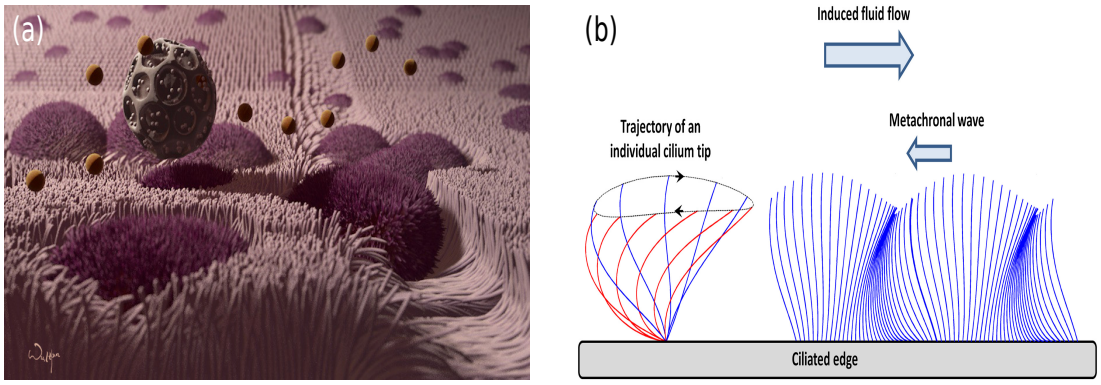

Figure 5 – Mucociliary clearance:
(a) 3D representation of the cilia motion in the lung from the Johns Hopkins school of medicine
(b) Motion of cilia during their active stroke adapted by [42] from [43]

Each ciliated cell has 200 to 300 uniformly spaced cilia of about $6\mu m$ in length [44], with a surface density around $(5-8)$ cilia/μm^2 [45] . The cilia beat in a synchronized, asymmetric, wavelike manner responsible for the net fluid flow [46, 42]. During their active motion, the cilia that are immersed into the Newtonian layer, with only their tips in contact with the mucus layer, propel the mucus at a rate of $\sim 3mm.min^{-1}$ [47] out of the airways (see Fig. 5). The coordinate motion of the cilia in the mucus gel create a surface that undulate in a wavelike manner known as metachronal wave [48, 49, 50].

The efficiency of such a system is highly dependent of the rheology of mucus in particular the depth of the Newtonian layer [51, 18, 52, 53]and the motion and interactions between the cilia and the mucus [54, 42]. Cilia are quite numerous in the trachea and large bronchi but their presence reduce as we go further in the bronchial tree, even disappearing in the respiratory region. The mucus clearance in this region is ensured by the mechanism of breathing or by cough allowing to reach speeds up to $200m.s^{-1}$ [55]. Cough is especially important when airways have accumulated abnormal amounts of mucus with altered rheological properties [56].

Pathologic mucus and lung conditions

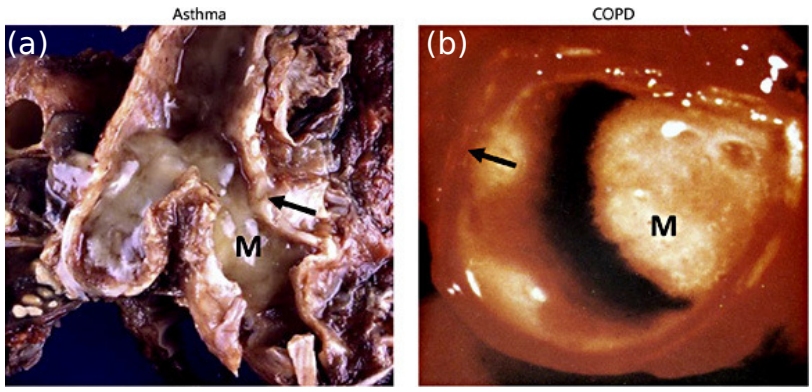

(c)

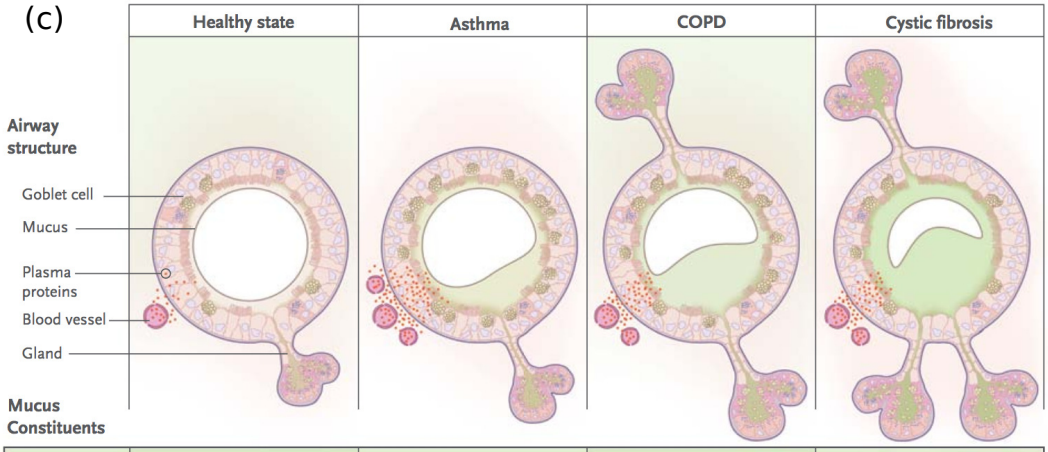

	Healthy state	Asthma	COPD	Cystic fibrosis
Mucin	X X	X X X X X	X X X X	X X X X
Plasma proteins	X	X X X X	X X	X X
Inflammatory cells	X	X X X	X X X	X X X X X
DNA		X	X X	X X X X X
Actin		X	X X	X X X X X
Bacteria			X X	X X X X X

Figure 6 – Lung conditions:
(a-b) Mucus production in asthma and COPD. Excess mucus M is seen partially occluding the large airways (arrows) of asthma and COPD patients. The excess mucus could be due to excess synthesis or hypersecretion, or both [26].
(c) Mucus characteristics of some airways diseases [24]

Healthy mucus is easily cleared by the mucociliary system whereas pathologic mucus often has altered properties such as higher viscosity and elasticity and is less easily cleared [23, 27]. The combination of mucus hypersecretion and impaired mucociliary clearance can cause a persistent accumulation of altered mucus in the airway which in turns can lead to infection and inflammation by providing an environment for microbial growth. Above a critical thickness, the accumulated mucus can form mucus plugs inside the airways (see Fig. 6) and obstruct airflow through the bronchial tree [57]. Some of the major lung conditions associated with pathologic mucus are: (i) Asthma which is a chronic lung disease triggered by allergy or pollution [58, 35, 59, 60], (ii) Cystic fibrosis which is a genetic disorder in which mucus does not clear easily from the airways [61, 62, 28], (iii) Chronic Obstructive Pulmonary Disease (COPD) characterized by a non reversible and progressive breathing limitations [32, 58, 63] and (iv) Lung cancer that affect almost any part of the lung.

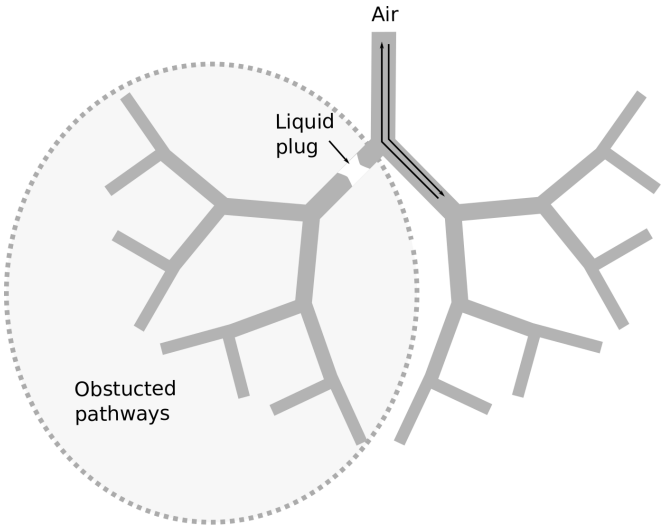

Figure 7 – Regular dichotomy model of 5 generation of the lung obstructed by a liquid plug. The obstructed pathways become part of the death volume of the lung adapted from [64].

When a mucus plug obstructs a branch of the airway, airflow cannot occur below the plug and the obstructed pathways become part of the death volume of the lung (see Fig. 7). The question of airway reopening is therefore essential for

patient suffering from airway obstruction. In the next section, we will see the mechanisms leading to the formation of liquid plugs and show different models of airway reopening.

Pulmonary surfactant

Pulmonary surfactant is a mixture of proteins and lipids secreted in the alveoli by the alveolar epithelial type II cells. This material is found in the mucus lining of the alveoli where it acts to decrease surface tension at the air–liquid interface of the alveoli. The presence of surfactant increases the stability of alveoli, although collapse can still occur in disease. It has some other functions including: (i) the reduction of the work necessary to breathe by increasing the pulmonary compliance, (ii) the prevention of the lung collapse and (iii) the lubrication of the lung [2].

A lack of surfactant in the lung result in consequences like the infant respiratory distress syndrome (IRDS) found in premature infants or the respiratory distress syndrome (RDS) in adult, that can even up to death due to the lung collapse. In these cases, surfactant replacement therapy (SRT) can be used to deliver synthetic surfactant bolus into the lung in newborn [65, 66, 67, 68],or surfactant therapy with mechanical ventilator for breathing can be used in adults [69, 70, 68].

The effect of surfactant therapy on mucus was shown to decrease the viscoelasticity of mucus in (RDS) [72], and increase the mucus flow velocities [73, 74]. It can be expected to be beneficial in the treatment of obstructive airway diseases like asthma and chronic bronchitis by enhancing the mucus clearance mechanism (see Fig. 8).

Airway closure and reopening models

Airway closure

Pulmonary airway closure by liquid (mucus) plugs can occur via various mechanisms including:

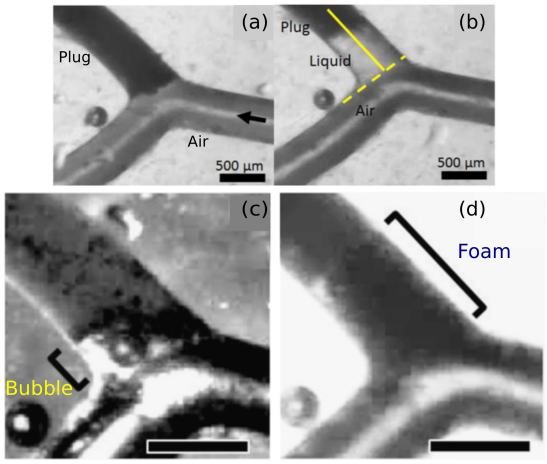

Figure 8 – Mucus clearance in a cylindrical bifurcating channel obstructed by a plug of Pig gastric mucin (PGM) mixed with de-ionized water [71]:
(a) - (b) Mucus clearance of the mixture using air flow.
(c) - (d) Addition of surfactant improved clearing effectiveness due to bubbling in $1mm$ diameter channels and foaming in $500\mu m$ diameter channels.

- Surface tension (capillary) instability of the thin liquid film lining the airways [38, 75, 12]
- The elastic collapse of the small airways [75, 12, 76, 77]
- The introduction of liquid bolus (plugs) in the larger airways during surfactant therapies [78, 68].

Capillary instability

The instability leading to the formation of mucus plug is the same mechanism explaining the destabilisation and breakup of a long falling liquid film into small drops of minimal surface area in Fig. 9a, and the formation of liquid plugs in a horizontal tube in Fig. 9b. This phenomenon known as Rayleigh-Plateau instability [80, 81, 82] is caused by capillary, inertia or gravity effects. The situation of a liquid layer lining a tube is the one observed in the lungs, therefore, we will focus on that.

A liquid layer lining the walls of a tube is an unstable configuration no matter how smooth the flow is. Lets consider an initial perturbation of wavelength L in

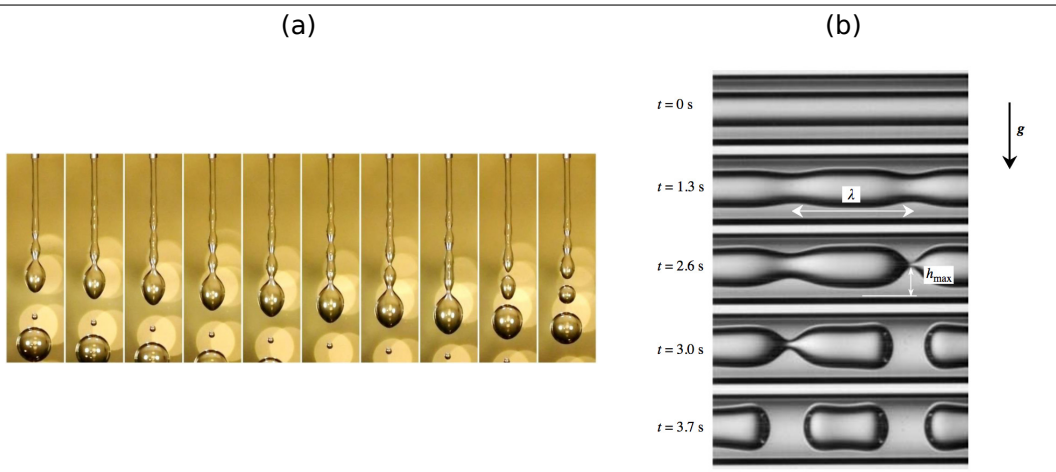

Figure 9 – Capillary instability of:
(a) A water jet film in oil [79].
(b) A liquid film lining an horizontal rigid capillary tube [57].

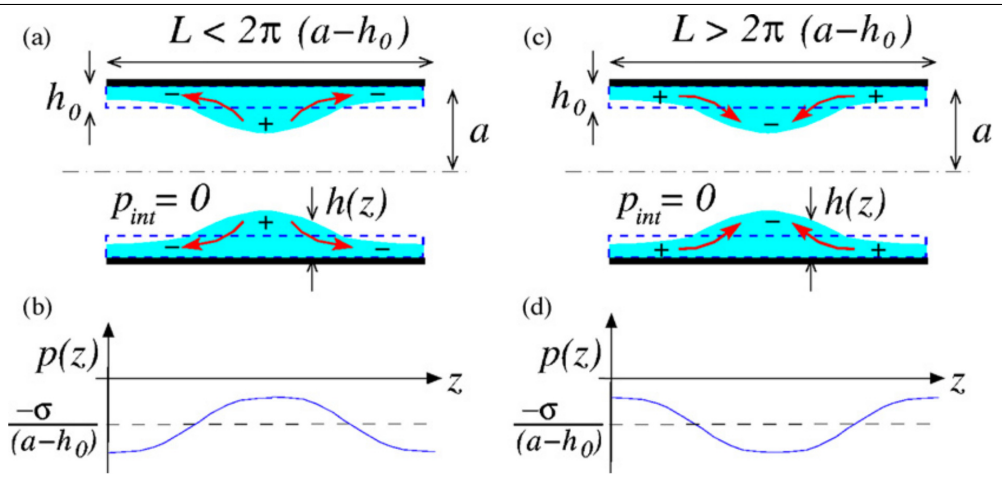

Figure 10 – Axisymmetric Rayleigh-Plateau instability of a liquid film of thickness h_0 lining a tube of radius a. The destabilisation of the liquid layer can eventually lead to the formation of a liquid plug if the wavelength of the perturbation $L > 2\,\pi(a - h_0)$, or the liquid layer will return to a uniform state if $L < 2\,\pi(a - h_0)$ [75].

the stream (see Fig 10). Once the instability is initiated, the fluid in the liquid layer continues to distribute until the system reaches a stable configuration minimizing its interfacial energy. The new equilibrium state can eventually lead

to the plugs formation if the wave length of the perturbation ($L > 2\pi(a - h_0)$). In this situation, the fluid pressure decreases in the cap, driving more fluid in this region and amplifying the perturbation, eventually leading to the formation of a liquid plug. Conversely, if the wave length ($L < 2\pi(a - h_0)$), the fluid pressure increases in the cap and a flow occur from the cap to the wall until the fluid returns to an axially stable state. From this analysis, it can be observe that for large wave lengths, a cylindrical interface is always unstable [64, 75].

The development of the Rayleigh-Plateau instability of a liquid film lining a horizontal tube when gravity effect are negligible, result in the competition between viscous and capillary effects. The most unstable mode of the liquid film destabilisation is associate with a characteristic time $\tau_{rp} = 12\mu a^4/\sigma {h_0}^3$ and a wavelength $L = 2\pi\sqrt{2}a$ [83, 84].

Elastic collapse

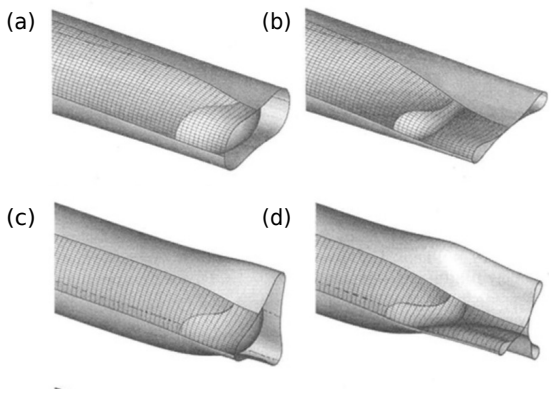

Figure 11 – Non-axisymmetric elastic instability of the airway walls[77]:
(a) - (b) Two-lobed mode collapse at low liquid surface tension.
(c) - (d) Three-lobed mode collapse at high liquid surface tension.

The low young modulus of the pulmonary airways make them easy to collapse enhancing the capillary instability of the liquid lining the airways and giving rise to a surface tension capillary-elastic instability (see Fig. 11). Airway closure due to elastic collapse tend to occur naturally in smaller airways of a normal lung at the end of expiration but reopening occurs in the early stage of inspiration [85,

18, 86, 75]. The compression load P_w exerted on the airway wall is proportional to the difference between the external pressure P_e which in this case is the pleural pressure and the pressure in the core of the fluid $P_f = P_i - \sigma/(a - h_0)$ with P_i the air pressure in the lumen [75]:

$$P_w = P_e - P_i + \frac{\sigma}{(a - h_0)} \tag{4}$$

When surface tension becomes important, the wall pressure increases, leading to the collapse of the airways. At relatively low surface tension, the collapse of the airway is dominated by the external pressure and the two lobed non-axisymmetric instability occurs. Increasing the surface tension increases the effects of the load caused by the liquid plug. This situation is favorable to generate three lobed non-axisymmetric collapse that is more likely to occur when the airway collapse over a short axial length scale due to a high surface tension [77]. Pathological conditions may give rise to permanent pulmonary collapse by changing the mucus properties or the mechanical properties of the airways.

Other studies on the walls elasticity [87, 88, 89], the non-Newtonian properties of mucus [90, 31], the presence of surfactant [91],the effects gravity [92, 93, 57], the curvature of the bronchi [94] or inertia [95] affect the development of the instability.

Airway reopening

The issue of airway reopening is critical for patients suffering from airway obstruction. Several models to study airway reopening in rigid tubes under constant pressure difference have been developed in the literature. From these studies, the central role played by the liquid lining the airway is shown: In a dry capillary tube (see Fig. 12), the propagation of the liquid plug is always accelerative since the plug always leaves liquid on the walls and does not recover liquid from its front meniscus (interface), the plug decreases in size and ruptures in an accelerative event [96]. The propagation of the plug in a liquid-lined tube can be either accelerative or decelerative depending on the initial liquid film layer h_0 [97, 98]. This ascertainment allowed the derivation of the critical

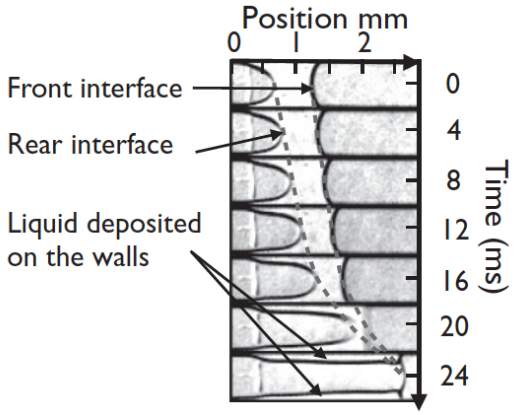

Figure 12 – Rupture of a liquid plug in a rectangular microfluidic channel showing the evolution of the front meniscus (interface) and the rear meniscus (interface) [96].

constant pressure head required to rupture a liquid plug in a liquid-lined tube [97]. Modeling of the propagation of liquid plugs also allowed to determine the mechanical stresses exerted on the walls during the propagation of a liquid plug and therefore quantify the damages on pulmonary airways [99].The effects of gravity and inertia [93] and non-Newtonian properties of the mucus [100] were also explored. In particular, the non-Newtonian properties of the fluid lead to an increase in the pressure drop necessary to drive the flow at a given speed.

In addition, walls flexibility was investigated to determine the pressure necessary to reopen obstructed pathways since the walls deform during the liquid plug formation and propagation in the airway tree [103, 104, 102, 105, 106]. In this configuration, the effect of surfactant [107] was shown to increase the normal stresses during reopening and the non-Newtonian properties of the liquid [108] lead to higher reopening driving pressure and longer reopening times (see Fig. 13).

Dissertation plan

This study was motivated by the absence of literature on the response of liquid plugs to complex driving conditions. Indeed, nearly all the model experiments

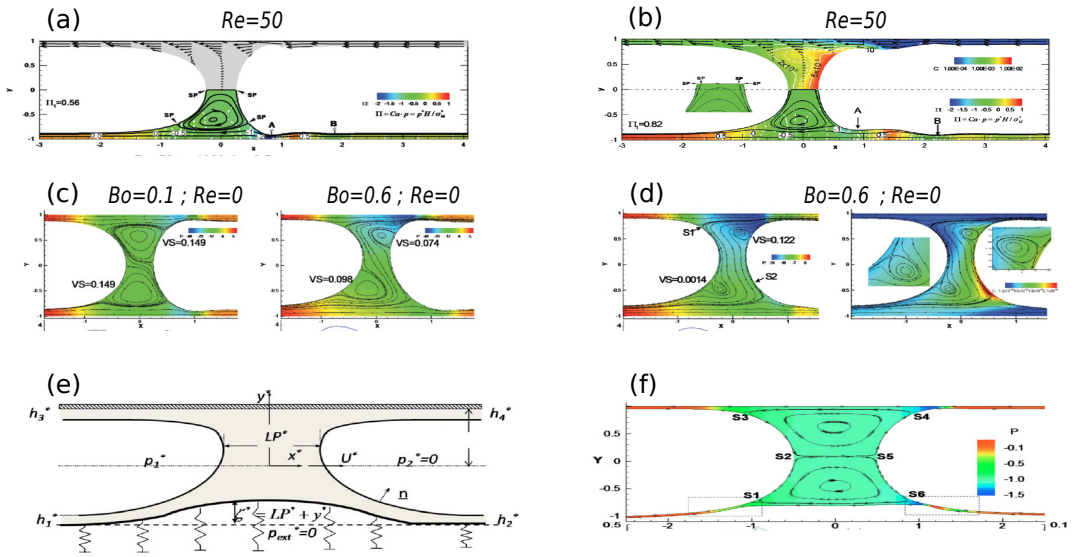

Figure 13 – Flow fields during the propagation of a liquid plug in a channel:
(a)Steady propagation of a liquid plug at $Re = 50$ without surfactant [101]
(b)Steady propagation of a liquid plug at $Re = 50$ with surfactant [101].
(c) Effect of gravity ($B_o = 0.1; 0.6$) in the unsteady propagation of a liquid plug without inertia effects [93].
(d) Effect of gravity ($B_o = 0.6$) and presence of surfactant in the unsteady propagation of a liquid plug without inertia effects [93].
(e) Model of PDMS channel with only one flexible wall [102].
(f) Propagation of a liquid plug in a flexible tube with only one flexible wall[102].

and simulations are conducted with a constant driving pressure or flow rate, which strongly differs from conditions enforced during a breathing cycle. This work aims at offering an experimental and theoretical understanding of the flow dynamics and rupture of liquid plugs under cyclic laminar forcing at a frequency close to a real breathing cycle.

The fluid that is used in the experimental sections of this work is a Newtonian fluid (Perfluorodecalin PFD) of density ρ, surface tension σ and dynamic viscosity μ close to the serous mucus. The experiments are performed in specific conditions: laminar flow ($Re < 2000$), negligible gravity effects ($Bo << 1$) and low capillary number ($Ca < 10^{-1}$). These hypothesis are valid below generation 10 of the airways for bronchioles of diameter below $1mm$ (Table 3.1).

In this work, we do not consider the presence of alveoli on the bronchi that are present in the respiratory region, the walls flexibility, the curvature of the bronchi or the presence of surfactant. We also assume that the capillary instability already occurred and the mucus plugs are already formed as in pathological conditions. We thus focus on the effects of cyclic periodic forcings mimicking a breathing cycle (see Fig. 3) on the dynamics of these plugs. Though it is an ideal model, we expect this study to open new prospects in the comprehension of mucus flow in the lung.

The first chapter of this dissertation focuses on the periodic flow rate and pressure forcing of liquid plugs in cylindrical rigid capillary tubes. Depending on the type of forcing, different behaviors are observed and the mechanisms leading to the rupture of liquid plugs are explained. In the second chapter we determine the critical pressure magnitude necessary to reopen obstructed prewetted tubes submitted to cyclic forcing. The third chapter investigates periodic forcing of liquid plugs in a rectangular channels. It is shown that the transition between two liquid film deposition regimes due to the polygonal shape of the microfluidic channel dramatically modifies the plug dynamics. And the last chapter explores periodic forcings of liquid plugs in tree-like symmetric and asymmetric networks. Different regimes are observed depending on the amplitude of the forcing and the geometry of the network. The preliminary results show that plugs not ruptured during the first half cycle persist in the airways for a long time and oscillate until their rupture.

The first chapter of this thesis was accepted for publication in the Journal of Fluid Mechanics and the third chapter is submitted to the International Journal of Multiphase Flow.

Chapter 1

Dynamics of a liquid plug in a capillary tube under periodic forcings

Abstract

In this chapter, we investigate the dynamics of a liquid plug driven by a cyclic periodic forcing inside a cylindrical rigid capillary tube. It is shown that depending on the type of forcing (flow rate or pressure cycle), the dynamics of the liquid plug can either be stable and periodic, or conversely accelerative and eventually leading to the plug rupture. In the latter case, we identify the sources of the instability as: (i) the cyclic diminution of the plug viscous resistance to motion due to the decrease in the plug length and (ii) a cyclic reduction of the plug interfacial resistance due to a lubrication effect. Since the flow is quasi-static and the forcing periodic, this cyclic evolution of the resistances relies on the existence of flow memories stored in the length of the plug and the thickness of the trailing film. Second, we show that contrary to unidirectional pressure forcing, cyclic forcing enables breaking of large plugs in confined space though it requires longer times. All the experimentally observed tendencies are quantitatively recovered from a reduced analytical model. This study not only reveals the underlying physics but also opens up the prospect for the simulation of "breathing" of liquid plugs in complex geometries and the determination of optimal cycles for obstructed airways reopening.

1.1 Introduction

Since the seminal works on gas-liquid flows in capillary tubes [109], [110] and [111], the subject have attracted much interest among different scientific communities due to their widespread occurrence in many natural and engineered fluidic systems such as pulmonary flows [12], oil extraction [112, 113], flow in porous media [114, 115, 116, 117], or microfluidic systems [118, 119, 120]. In particular, liquid plugs (also called bridges, slugs or boluses) play a fundamental role in pulmonary flows where they can form in healthy subjects [121, 122] or in pathological conditions [123, 124, 125, 126] due to a capillary or elasto-capillary instability [38, 127, 57, 75, 12, 95]. For patients suffering from pulmonary obstructive diseases, these occluding plugs may dramatically alter the distribution of air in the lungs, hence leading to severe breathing difficulties.

Conversely, liquid plugs can be used for therapeutic purpose [128, 69]: boluses of surfactant are injected inside the lungs of prematurely born infants to compensate for their lack and improve ventilation [67, 129]. A thorough understanding of liquid plugs dynamics is therefore mandatory to improve both treatments of patients suffering from obstructive pulmonary diseases and of prematurely born infants.

When a liquid plug moves inside a cylindrical airway at low capillary number, deformation of the front and rear menisci occurs near the walls and leads to interfacial pressure jumps at the front and rear interfaces. This deformation also leads to the deposition of a liquid film on the walls. From a theoretical point of view, Bretherton [111] was the first to provide an estimation of the pressure jump and the thickness of the liquid layer at asymptotically low capillary numbers. It's analysis was later formalized in the framework of matched asymptotic expansions [130] who extended this work to higher order developments. Later on, the dynamics of a meniscus moving on a dry capillary tube was studied both experimentally and theoretically [131, 132].

These pioneering results were later extended to unfold the effects of wall elasticity [103], the behavior at larger capillary numbers [133, 134], the effects of surfactants [135], the role of a microscopic or macroscopic precursor film [136, 137], the influence of more complex tube geometries [138, 139, 140], the

influence of gravity [92, 93] or the influence of non-Newtonian properties of the liquid [141, 142, 143, 144]. These key ingredients have then been combined with conservation laws determining the evolution of plug size and estimation of pressure jump in the bulk of the plug to provide analytical models of the unsteady dynamics of liquid plugs in capillary tubes [96, 97, 99]. In particular, [96] introduced the long range and short range interactions between plugs to simulate the collective behavior of a train of liquid plugs. These models were in turn used to determine the critical pressure head required to rupture a liquid plug in a compliant [103] or rigid prewetted capillary tube ([97]), or determine the maximum stresses exerted on the walls [99], a fundamental problem for lung injury produced by the presence of liquid plugs in the lung.

It is interesting to note that the dynamics of bubbles [111, 145, 146, 147] and liquid plugs in capillary tubes look similar from a theoretical point of view, since the interfacial pressure jumps and the deposition of a liquid film on the walls induced by the dynamical deformation of the interfaces can be calculated with the same formula. Nevertheless, there are also fundamental differences, which lead to very different dynamics: Trains of bubble are pushed by a liquid finger whose viscous resistance to the flow is generally higher than the resistance induced by the presence of the bubble. In this case, a pressure driven flow is stable and the flow rate remains essentially constant over time. In the case of liquid plugs, the resistance of the plugs to motion is higher than the one of the air in front and behind the plug. This leads to an unstable behavior with an acceleration and rupture of the plugs [96] or a deceleration and the obstruction of the airways [97].

From an experimental point of view, Bretherton's interfacial laws have been extensively verified for different systems (bubbles, liquid fingers, foams, ...). Nevertheless, there have been few attempts to compare the unstable dynamics of single or multiple plugs in capillary tubes to models accounting for the interface and bulk pressure jumps along with mass balance. Baudoin & al. [96] showed that their model was able to qualitatively predict the collective accelerative dynamics of multiple plugs in rectangular microfluidic channels. More recently, Magniez & al. [97] were able to quantitatively reproduce the acceleration and deceleration of a single liquid plug in a prewetted capillary tube. Their model

further provided the critical pressure below which the plug slows down and thickens whereas above it accelerates and ruptures. These experiments were particularly challenging owing to the complexity of controlling the prewetting film thickness and performing the experiments before the occurrence of Rayleigh-Plateau instability. Huh & al. [148] measured in realistic experiments the injury caused by the motion of liquid plugs on the human airway epithelium deposited at the surface of an engineered microfluidic airway. Later on, Zheng & al. [102] quantified the deformation of the walls induced by the propagation of a liquid plug in a flexible microchannel. Song & al. [149] employed microfluidic techniques to investigate single liquid plug flow in a tree geometry and evidenced the role of the forcing condition on the flow pattern. Finally, Hu & al. [31] studied the rupture of a mucus-like liquid plug in a small microfluidic channel.

From a numerical point of view, simulations of liquid plugs in capillary tubes are highly challenging. Indeed, the thin layer of liquid left on the walls requires either adaptive mesh or the use of Boundary Integral Methods to reduce the computational costs. Moreover, the unstable dynamics of the plugs pushed at constant pressure head leads to high variability in the associated characteristic times. Fujioka & al. [150] were the first to provide numerical simulations of the steady dynamics of a liquid plug in a two-dimensional channel. Later on, they studied the effects of surfactants [101], the unsteady propagation [151] in an axisymmetric tube, the effects of gravity [93] the role played by the tube's flexibility [102] and the motion of Bingham liquid plugs [100]. More recently, Vaughan & al. [152] studied numerically the splitting of a two dimensional liquid plug at an airway bifurcation.

In all the aforementioned theoretical, experimental and numerical studies, the liquid plugs are pushed either at constant flow rate or at constant pressure head in a single direction. These driving conditions substantially differ from the one in the lung where liquid plug will experience periodic forcing. In this chapter, we investigate both experimentally and theoretically the response of liquid plugs to cyclic and periodic pressure or flow rate forcing. The experiments are conducted in straight cylindrical glass capillary tubes and compared to an extended theoretical model based on previous developments [96, 97]. It is shown that, depending on the type of forcing (flow rate or pressure cycle), the dynamics

of the liquid plug can either be periodic with the reproduction of the same cyclic motion over time, or accelerative eventually leading to the plug rupture. In particular, this study discloses the central hysteretic role played by the liquid film deposition on the plug dynamics.

We first describe the experimental setup and the mathematical model. Thirdly, We discuss the effects of different type of forcings: pressure head and flow rate in the dynamical behavior of the liquid plug. Fourthly, we compare the efficiency of cyclic and unidirectional forcings for obstructed airways reopening. Finally, we discuss on the relevance of the proposed model to pulmonary congestion diseases.

1.2 Experimental method and model

The schematic of the experimental setup is provided in Fig. 1.1a. A perfluorodecalin liquid plug of controlled volume is injected through a needle inside a rigid horizontal cylindrical glass capillary tube (inner radius $R = 470\,\mu\text{m}$). Then, air is blown at low flow rate ($Q = 10\mu\text{l/min}$) to bring the liquid plug to the center of the channel and stopped manually when the plug reaches the target position. Thus, depending on the size of the liquid plug, the creation step can take up to 10 s. Finally, liquid plugs are moved back and forth with either pressure or flow rate cyclic forcings enforced respectively with a MFCS Fluigent pressure controller or a KdScientific 210 programmable syringe pump. For both pressure driven and flow rate driven experiments, the period of oscillation is fixed at $2T = 4$ s3, with T the duration of the motion in one direction. It is important to note that during the first half-cycle, $t \in [0, T]$, the liquid plug moves along a dry capillary tube (see Fig. 1.1b). The motion of the plug leads to the deposition of a trailing film on the walls of thickness h_r behind the rear meniscus at position $X_r(t)$. Thus, in the subsequent back and forth motion, the front interface of the liquid plug moves on walls prewetted by a layer of thickness $h_f(X_f)$ (with $X_f(t) = X_r(t) + L_p(t)$ the position of the front meniscus and $L_p(t)$ the plug length) as long as it remains on a portion of the channel already visited by the liquid plug (see Fig. 1.1c) in a previous half-cycle.

1.2.1 Experimental setup

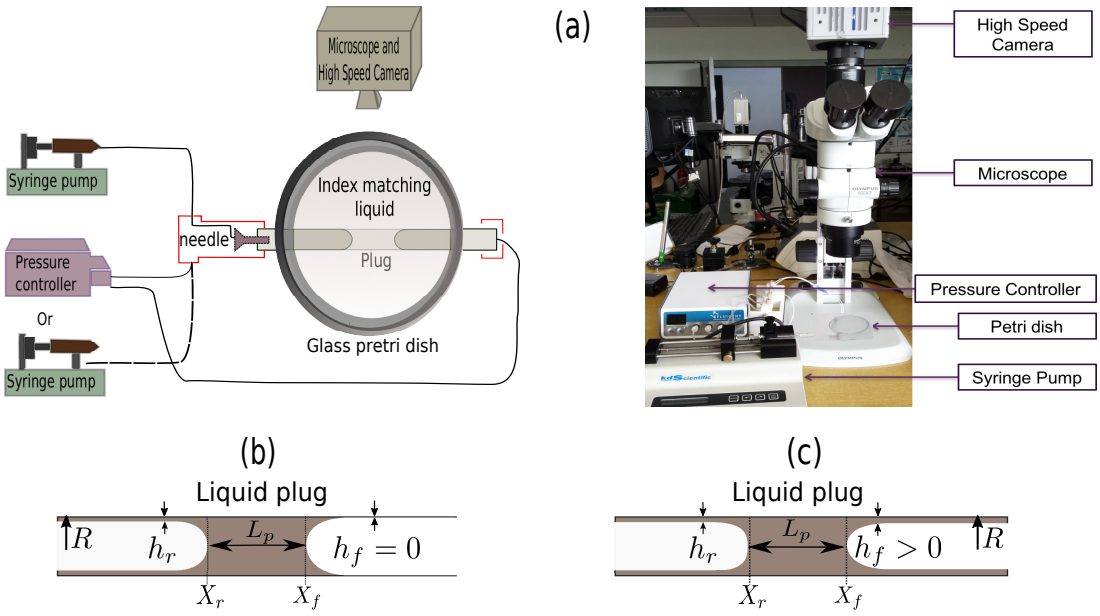

Figure 1.1 – Experimental description:
(a) Experimental setup.
(b) First half cycle : the liquid plug moves on a dry capillary tube.
(c) Following back and forth motions: the liquid plug moves on a prewetted capillary tube.

The glass capillary tubes were cleaned prior to the experiments with acetone, isopropanol, dichloromethane and piranha solutions (a mixture of sulfuric acid (H2SO4) and hydrogen peroxide (H2O2)) successively to obtain perfectly wetting surface and prevent dewetting induced by the presence of dust or organic contaminants on the surface. Perfluorodecalin (dynamic viscosity $\mu = 5.1 \times 10^{-3} Pa.s$, surface tension $\sigma = 19.3 \times 10^{-3} N/m$ and density $\rho = 1.9 \times 10^{-3} kg/m^3$) was chosen for its good wetting properties and inertness. Experiments are recorded using a Photron SA3 high speed camera mounted on a Z16 Leica Microscope at a frame rate of 125 images per second, a trigger time of $1/3000s$ and a resolution of 1024×64 pixels. To prevent image deformation due to the cylindrical shape of the capillary tube, it is immersed in an index-matching liquid. The image analysis is then performed using ImageJ software and Matlab.

1.2.2 Flow rate cyclic driving

The flow rate forcing (a) is obtained by connecting only one end (left side) of the capillary tube to a programmable syringe pump KdScientific 210. The command flow rate is a square signal with alternative motion in the right and left directions (see Fig. 1.2a). Owing to the response time of the syringe pump and compressibility effects, the actual flow rate imposed to the liquid plug may differ strongly. Thus, the imposed flow rate is monitored directly by measuring the motion of the left interface of the liquid plug. This signal is represented on Fig. 1.2b.

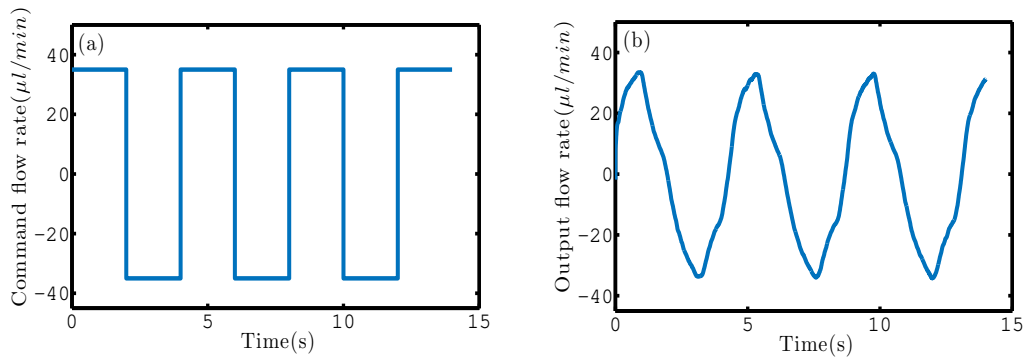

Figure 1.2 – Flow rate cyclic driving:
(a) Command flow rate ordered to the programmable syringe pump. Positive values correspond to a motion from the left to the right.
(b) Actual flow rate forcing measured by monitoring the motion of the left interface of the plug.

1.2.3 Pressure cyclic driving

The pressure driving is obtained by connecting two channels of the MFCS programmable pressure controller to both ends of the capillary tube. This pressure controller based on valve and sensors enables automated control of the driving pressure. We impose alternatively a constant command overpressure (compared to atmospheric pressure) P_1^c and P_2^c to each channel of the pressure controller while the pressure of the other channel goes down to atmospheric

pressure, as represented on Fig. 1.3a. Due to the response time of the pressure controller (resulting from the response time of the valve, and the feedback loop, the actual overpressure imposed to each side of the pressure controller (measured by an integrated pressure sensor) is represented on Fig. 1.3b. The final pressure forcing thus corresponds the difference of pressure $\Delta P_t = P_1^c - P_2^c$ between the two ends of the channel (see Fig. 1.3c).

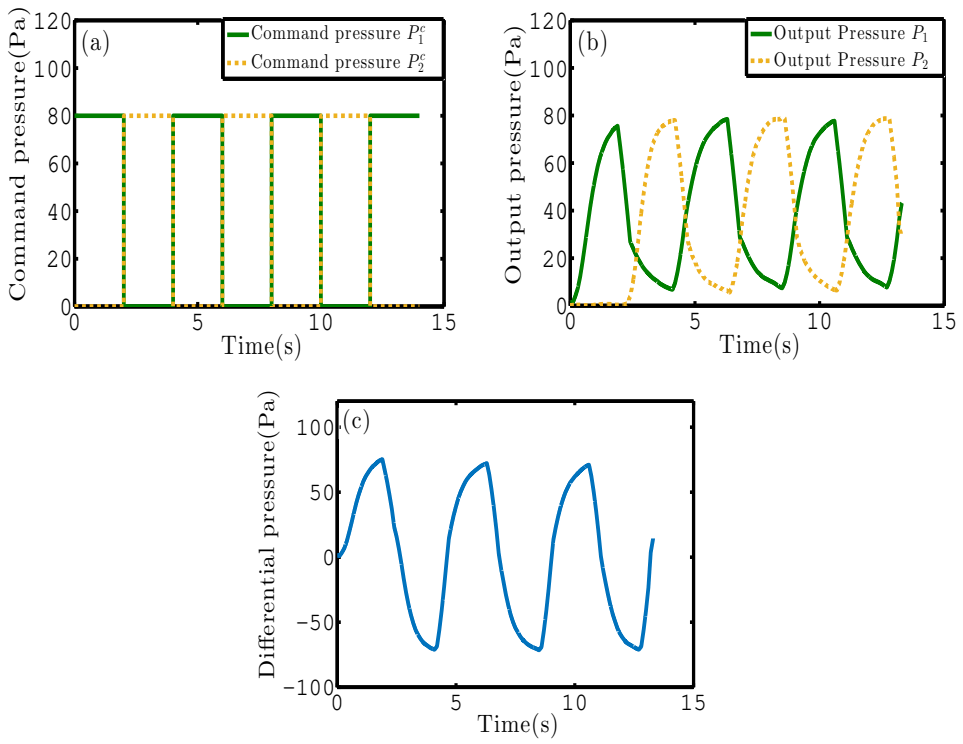

Figure 1.3 – Pressure cyclic driving:
(a) Command pressures P_1^c and P_2^c imposed via the software Maesflow to each channel of the MFCS Fluigent pressure controller, connected respectively to each extremity of the capillary tube.
(b) Resulting output pressure signals effectively imposed to each end of the capillary tube, measured with an integrated sensor. The pressure represented on these figures correspond to overpressures compared to atmospheric pressure.
(c) Pressure driving $\Delta P_t = P_1 - P_2$ imposed to the liquid plug.

1.2.4 Effects of air compressibility

In the experimental context, compressibility effects are critical for flow rate driven experiments, since they increase the response time of the syringe pump (difference between the piston motion and the actual motion of the fluid in the capillary). To reduce this response time, the syringes are filled with water. Moreover, since the imposed flow rate is measured directly by monitoring the displacement of the left interface, compressibility effects are accounted for in the forcing condition. For pressure driven experiments however, the pressure is homogenised at the speed of sound (extremely rapidly) and the response time is mainly due to the valve and sensors response time. Thus, the pressure measured at the exit of the pressure controller with integrated pressure sensors is almost identical to the pressure imposed at both side of the capillary tube (if we neglect the pressure losses due to the air flow in the tubes compared to the pressure losses due to the presence of the liquid plug).

1.3 Mathematical model

1.3.1 Dimensional analysis of the problem

The characteristic parameters in this problem are the radius of the tube R, the surface tension σ, the liquid density ρ and viscosity μ , and the characteristic speed U of the liquid plug. From these parameters, one can derive the characteristic convection time $\tau_c = R/U$, the characteristic viscous diffusion time $\tau_v = \rho R^2/\mu$, the Reynolds number $Re = \rho UR/\mu$ (comparing inertia to viscous diffusion), the capillary number $Ca = \mu U/\sigma$ (comparing viscous diffusion to surface tension), the Bond number $Bo = \Delta\rho g R^2/\sigma$ (comparing gravity effects to surface tension) and finally the Weber number $We = \Delta\rho U^2 R/\sigma$ (comparing inertia to surface tension). Table 1.1 summaries the maximum values of these key dimensionless parameters based on the maximal velocity of the liquid plug $U_m = 28mm/s$ observed in the present experiments.

Based on the order of magnitude of these dimensionless parameters, a few primary insights can be drawn. The low Bond number and the horizontal

position of the tube suggest weak effect of gravity in this problem. The flow in the bulk of the plug remains laminar owing to the moderate values of the Reynolds number. In addition, Aussillous & Quéré [133] studied the impact of inertia on the deposition of a trailing liquid film behind a moving liquid plug. From dimensional analysis and experiments, they introduced a critical capillary number Ca_c (equal to 3.6×10^{-1} in the present case) above which the effect of inertia becomes significant. In the present experiments, the capillary number is two order of magnitude smaller than this critical value and thus inertia can be neglected in the film deposition process. Finally, Kreutzer & al. [153] studied numerically the influence of inertia on pressure drops at liquid/air interfaces. They showed that inertia plays no role for $Re < 10$ at capillary numbers comparable to the present study. Thus, inertial effects can safely be neglected here. Furthermore, the weak capillary and Weber numbers indicate that surface tension is globally dominant over viscous stresses and inertia. Nevertheless, it is to be emphasized that viscous effects must still be accounted for close to the walls, in the so-called "dynamic meniscus" that is the part of the meniscus deformed by viscous stresses. Finally, since the convection and viscous diffusion times τ_c and τ_v are two orders of magnitude smaller than the duration of the pressure or flow rate cycles, unsteady term in Navier-Stokes equation can be neglected and the flow can be considered as quasi-static.

Another phenomenon that may occur during the plug motion is the destabilisation of the trailing liquid film due to a Rayleigh-Plateau instability. The characteristic time associated with the most unstable mode [83, 84] is given by :

$$\tau_{RP} = \frac{12\mu R^4}{\sigma h^3}$$

The smallest destabilisation times is thus obtained for the thickest fluid layer. In the experiments conducted in this chapter, the thickness of the liquid film remains typically smaller than 5% of the tube radius leading to $\tau_{RP} = 13$ s, whose value remains significantly larger than the period of the plug motion ($2T = 4$ s). In addition, this time grows rapidly ($\propto 1/h^3$) when the thickness of the layer is decreased ($\tau_{RP} = 58$ s for $h/R = 3\%$) and thick films are only deposited close to the plug rupture in the pressure driven experiments so that the destabilisation

parameters	Formula	Maximum value
τ_c	R/U	$1.7 \times 10^{-2}\ s$
τ_v	$\rho R^2/\mu$	$8.2 \times 10^{-2}\ s$
Re	τ_d/τ_c	4.9
Ca	$\mu U/\sigma$	7.4×10^{-3}
Bo	$\Delta\rho g R^2/\sigma$	2.1×10^{-1}
We	$\Delta\rho U^2 R/\sigma$	3.6×10^{-2}

Table 1.1 – Values of the key parameters associated with the maximal velocity U_m

of the trailing film is expected to play a minor role in the following experiments.

1.3.2 Model: pressure driven forcing

In this context, the liquid plug dynamics can be predicted from a quasi-static pressure balance and a mass balance. We thus adapted a visco-capillary quasi-static model previously introduced by Magniez & al. [97] to include the motion on both dry and prewetted portions of the tube and also the memory effects resulting from a trailing liquid film deposition. Assuming that the pressure losses in the gas phase are negligible compared to that induced by the liquid plug, the total pressure jump ΔP_t across a liquid plug can be decomposed into the sum of the pressure jump induced by the presence of the rear interface ΔP^{int}_{rear}, the front interface ΔP^{int}_{front} and the flow in the bulk of the plug ΔP^{bulk}_{visc}:

$$\Delta P_t = \Delta P^{bulk}_{visc} + \Delta P^{int}_{rear} + \Delta P^{int}_{front} \tag{1.1}$$

In the experiments, ΔP_t corresponds to the driving pressure head.

Viscous pressure drop

Since the flow is laminar, the viscous pressure drop in the bulk of the plug can be estimated from Poiseuille's law:

$$\Delta P^{bulk}_{visc} = \frac{8\mu L_p U}{R^2} \tag{1.2}$$

with L_p, the plug length, that is to say the distance between the front and rear meniscus $L_p(t) = X_f(t) - X_r(t)$ as described in Fig. 1.1 and $U = dX_r/dt$ the liquid plug velocity. This expression relies on two approximations: (i) it assumes a Poiseuille flow structure and thus neglects the fluid recirculation occurring close to the menisci and (ii) it assumes the same speed for the rear and front interfaces. The validity of the first approximation has been tested with direct numerical simulations performed with a Volume of Fluid (VOF) method.

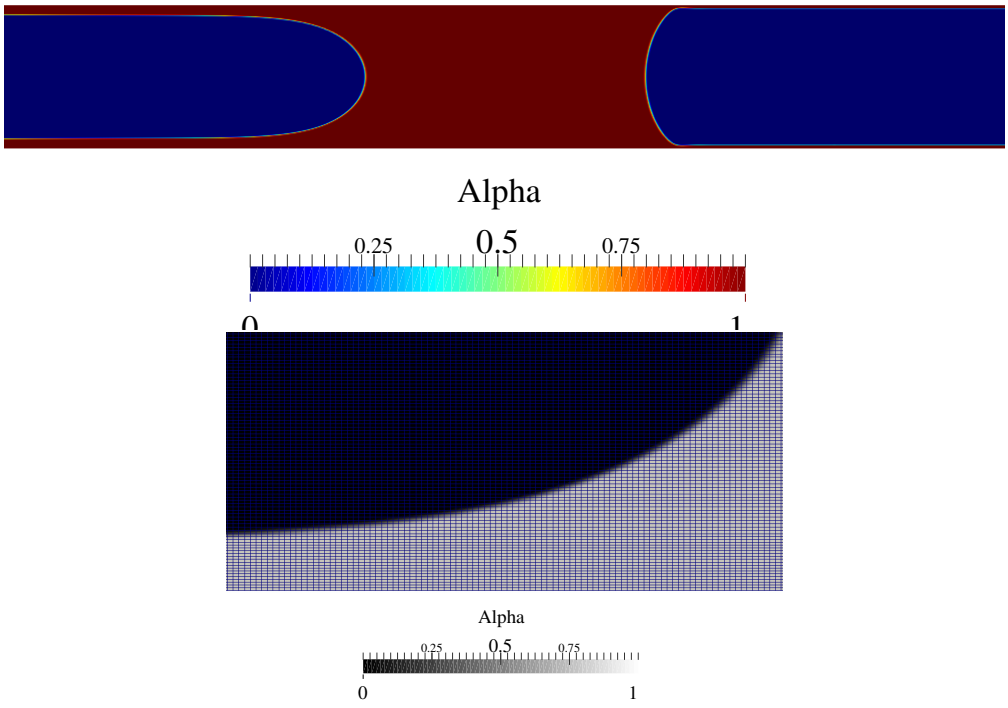

Figure 1.4 – Configuration simulated with the VOF code Openfoam: a liquid plug is pushed at constant flow rate with an air finger inside a prewetted capillary tube. Up: Phase volume fraction α. The air is represented in blue ($\alpha = 0$) and the liquid in blue ($\alpha = 1$). Down: Zoom on the edge of the liquid plug to show the precision of the mesh.

Equation (1.2) relies on the assumption that the flow inside the liquid plug is a Poiseuille flow. In a Poiseuille flow, the liquid velocity is maximum at the center of the tube and decreases down to 0 at the walls. This flow structure is not compatible with the boundary conditions imposed by the two menisci:

a constant velocity all over the liquid/air interface (in absence of interfacial deformation). Therefore, fluid recirculation will occur at the edges of the plug to match this boundary condition. For long plugs this recirculation is expected to play a minor role. Thus Equation (1.2) should give a correct approximation of the pressure drop inside long plugs. However the accuracy of this approximation should decrease as the length of the plug drops. To test the validity of equation (1.2), we performed 2D direct numerical simulations of a flow rate driven liquid plug in a capillary tube with the Openfoam Volume of Fluid (VOF) code (see Fig. 1.4). This code was modified to include a regularisation technics by Hoang & al. [154], which reduces parasitic currents. The evolution of the viscous pressure drop as a function of the plug size was evaluated by pushing a liquid plug at a constant flow rate corresponding to $Re = 2$ and $Ca = 5 \times 10^{-2}$ in a prewetted tube (layer of thickness corresponding to 4% of the tube diameter D). The properties of the liquid are the same as the one used in the experiments. A 825 000 points structured mesh was used with a refinement close to the walls (see Fig. 1.4). Fig. 1.5 shows the computed pressure drop inside the liquid plug and the air. Since the input flow rate leads to a deposition of a trailing film thicker than the prewetting film, the length of the plug shrinks, which enables the evaluation of the pressure drop for various plug lengths with a single numerical simulation. The comparison between Poiseuille's law and simulations is shown on Fig. 1.6 (left) with a zoom on small values of the plug length on Fig. 1.6 (right). This comparison shows that the discrepancy between the formula remains weak (below 4.5% for plugs with sizes $L_p > D$) but increases up to 25% for plugs whose size lies between $1/4D$ and D.

As expected, the accuracy of this approximated formula decreases with the size of the plug. Nevertheless, the difference between approximated and computed values remains below 4.5% for plugs larger than the tube diameter and below 25% for plugs larger than 1/4 of the tube diameter. The approximation is therefore consistent for large plug. The larger discrepancy observed for smaller plugs is not critical since in this case the interfacial pressure drops at the rear and front interfaces are largely dominant over the viscous one. We verified the consistency of the second approximation experimentally by measuring the difference between the front and rear interface speeds. These measurements

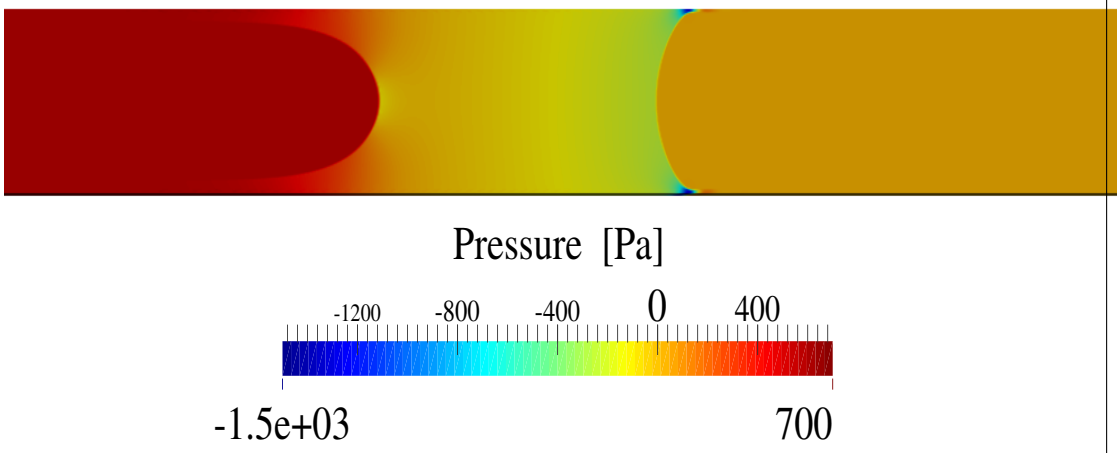

Figure 1.5 – Pressure variation (in Pa) inside the plug and the air in the configuration represented on 1.4.

show that the speed of the two menisci only differ by a few percent. The reason is that the evolution of the plug size dL_p/dt remains much smaller than the plug velocity dX_r/dt for the essential part of the plug dynamics. In the following, we keep this assumption (front and rear interfaces velocities approximatively equal) to evaluate the interfacial pressure jump).

Interfacial pressure drops

Since the Capillary, Bond and Reynolds numbers are small and the flow is quasi-static (see section 1.3.1), the pressure drop across the rear interface Fig. 1.7 of the moving liquid plug can be estimated from Bretherton's formula [111] :

$$\Delta P^{int}_{rear} = \frac{2\sigma}{R}(1 + 1.79(3Ca)^{2/3}) \tag{1.3}$$

Finally, the Laplace pressure drop across the front meniscus depends on the apparent dynamic contact angle θ^a_d according to the formula (in the limit of low capillary number and thus θ^a_d):

$$\Delta P^{int}_{front} = -\frac{2\sigma cos\theta^a_d}{R} \approx -\frac{2\sigma(1-\theta^{a\,2}_d/2)}{R} \tag{1.4}$$

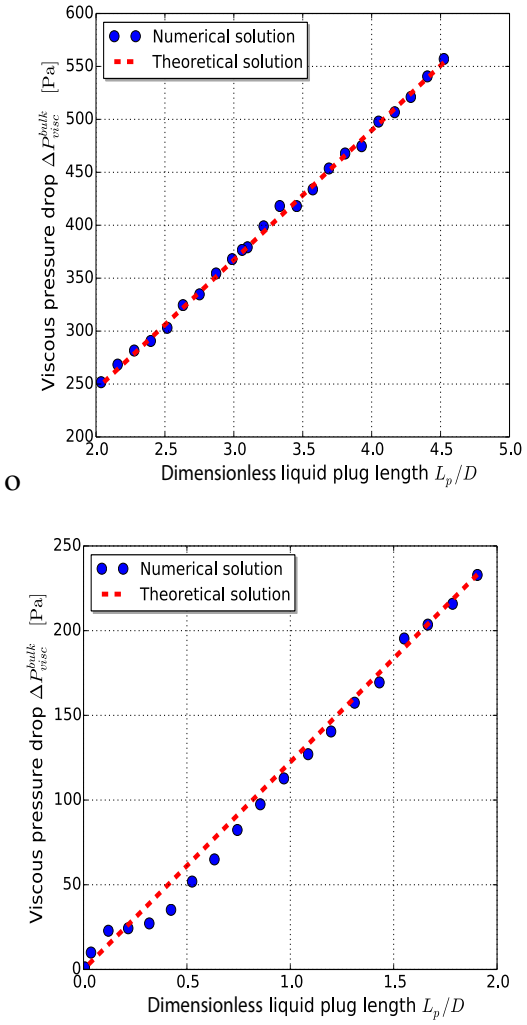

Figure 1.6 – Comparison of the simulated pressure drop ΔP_{visc}^{bulk} (blue dots) and Poiseuille law (red dashed line) as a function of the plug dimensionless plug length L_p/D, with D the tube diameter. Left: evolution for large plug. Right: zoom for small plugs.

Choosing the Laplace pressure jump $2\sigma/R$ as the characteristic pressure scale, and the tube radius R as the characteristic length scale, the dimensionless pressure jump across the liquid plug becomes:

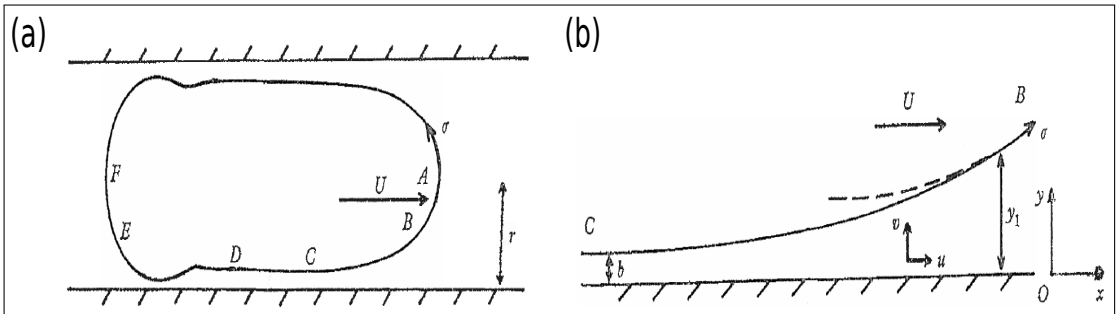

Figure 1.7 – The motion of a bubble in a tube by Bretherton [111]:
(a) Motion of a long bubble in a capillary tube filled with liquid. The rear and front interfaces of the bubble are respectively the front and rear interfaces of the plug.
(b) Transition regions at the rear meniscus of the plug.

$$\Delta\tilde{P}_t = 4\tilde{L_p}Ca + 1.79(3Ca)^{2/3} + \frac{\theta_d^{a\,2}}{2} \tag{1.5}$$

A tilde indicates dimensionless functions.

In order to achieve a closed set of equation, two additional equations must be derived. They are (i) the relation between the apparent dynamic contact angle of the front meniscus θ_d^a and the capillary number Ca and (ii) an equation determining the evolution of the plug length $\tilde{L_p}$. The first relation depends on the wetting state of the tube walls ahead of the liquid plug:

When the liquid plug moves on a *dry substrate* Fig. 1.8a, this relation is given by Hoffman-Tanner's law valid at low capillary numbers:

$$\theta_d^a = ECa^{1/3} \tag{1.6}$$

with E a numerical constant of the order of $(4-5)$ for a dry cylindrical capillary tube as reported by Hoffman [131] and Tanner [132]. For a liquid plug moving on a *prewetted substrate* Fig. 1.8b, θ_d^a can be calculated from Chebbi's law [137], which can be simplified at low capillary number through a second order Taylor

expansion by Magniez & al [97]:

$$\theta_d^a = \frac{-1+\sqrt{1+4CD}}{2C} \tag{1.7}$$

with:

$$A = (3Ca)^{-2/3}\tilde{h_f} \tag{1.8}$$

$$B = (3Ca)^{1/3} \tag{1.9}$$

$$C = \frac{1}{log(10)}\left(\frac{b_1}{2} + b_2 log_{10}(A) + \frac{3b_3}{2}\left[log_{10}A\right]^2\right)B \tag{1.10}$$

$$D = \left(b_0 + b_1 log_{10}(A) + b_2\left[log_{10}(A)\right]^2 + b_3\left[log_{10}(A)\right]^3\right)B \tag{1.11}$$

$$b_0 \approx 1.4,\ b_1 \approx -0.59,\ b_2 \approx -3.2\times10^{-2},\ \text{and}\ b_3 \approx 3.1\times10^{-3} \tag{1.12}$$

Since $CD \ll 1$ at low capillary number (in the present experiments $CD < 5\times10^{-2}$), this equation can further be simplified into:

$$\theta_a^d = D = FCa^{1/3} \tag{1.13}$$

with $F = 3^{1/3}\left(b_0 + b_1 log_{10}(A) + b_2\left[log_{10}(A)\right]^2 + b_3\left[log_{10}(A)\right]^3\right)$.

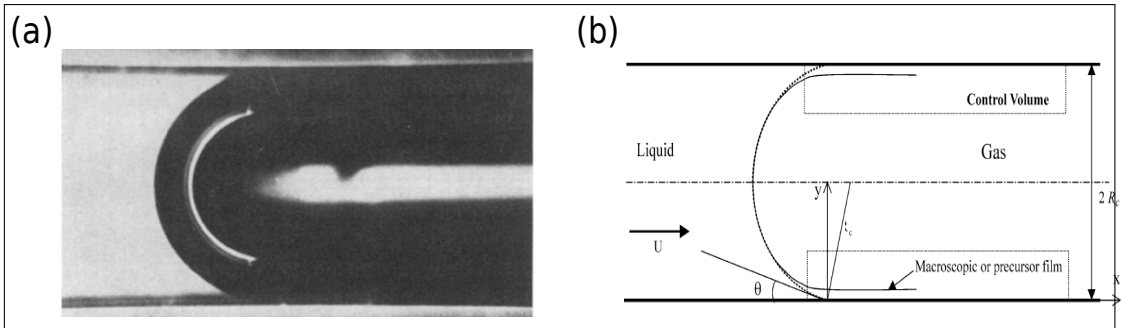

Figure 1.8 – Front gas-liquid meniscus:
(a) Along a dry substrate by Hoffman [131].
(b) Along a prewetted substrat showing the contact angle θ by Chebbi [137].

The next step is to determine the dimensionless plug length $\tilde{L_p}$. A simple

mass balance between the fluid collected from the fluid layer lying ahead the plug (of thickness h_f) and the trailing liquid film (of thickness h_r) deposited behind the plug gives:

$$dV = (\pi R^2 - \pi(R-h_f)^2)dX_f - (\pi R^2 - \pi(R-h_r)^2)dX_r \tag{1.14}$$

with $V = \pi R^2 L_p$ the volume of the plug. Finally, with $dX_r = Udt$ and $dX_f = \frac{(R-h_r)^2}{(R-h_f)^2}dX_r$, we obtain:

$$\frac{dL_p}{dt} = \left[\frac{(R-h_r)^2}{(R-h_f)^2} - 1\right]U \tag{1.15}$$

Using the capillary time scale, $\mu R/\sigma$, as the characteristic time scale, this equation can be rewritten in the dimensionless form:

$$\frac{d\tilde{L_p}}{d\tilde{t}} = \left[\frac{(1-\tilde{h_r})^2}{(1-\tilde{h_f})^2} - 1\right]Ca \tag{1.16}$$

Liquid film deposition

The last essential point is to determine the thicknesses of the liquid film lying in front and left behind the liquid plug h_r and h_f respectively. The thickness of the trailing film can be calculated from an extension of Bretherthon's law introduced by Aussillous & Quéré [133] (see Fig. 1.9). This thickness only depends on the velocity of the plug U, that is to say in dimensionless form only on the capillary number Ca:

$$\tilde{h_r} = \frac{1.34Ca^{2/3}}{1 + 2.5 \times 1.34Ca^{2/3}} \tag{1.17}$$

Finally, the thickness $\tilde{h_f}$ depends on the history of the plug motion. Indeed, the capillary tube is initially dry. Thus, for a cyclic motion, the liquid film lying ahead of the plug at position X_f^N during the half-cycle N comes from the deposition of a trailing film behind the plug at the same position $X_r^{N-1} = X_f^N$ during the half cycle $N-1$. In order to determine $\tilde{h_f}$, the thickness of the liquid film deposited on the walls must therefore be kept in memory and then taken as

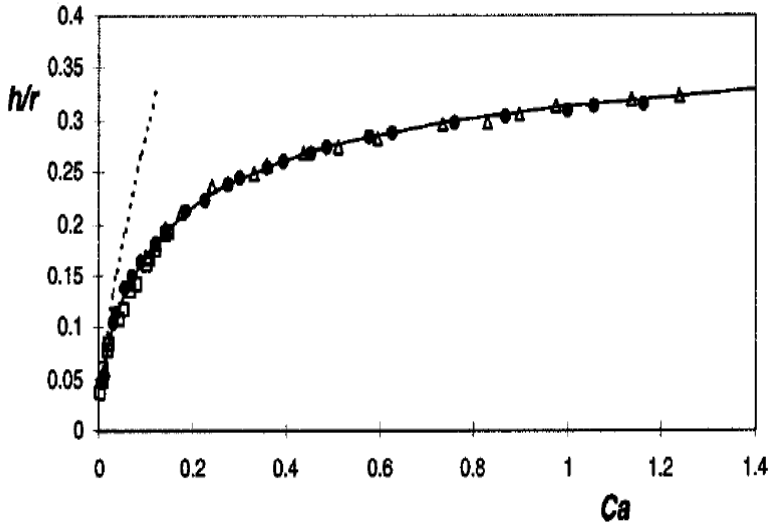

Figure 1.9 – Liquid film thickness h/r deposited at the rear interface of liquid plug moving along a capillary tube as a function of the capillary number Ca. The straight dashed line is the prediction of Bretherton's law [111] valid at low capillary number ($Ca < 10^{-3}$) and the full line is the extended formula proposed by Aussillous & Quéré [133] valid at high capillary number.

an entry when the plug moves back to the same location. If the plug moves to a location never visited before, then the tube is dry, $\tilde{h_f} = 0$ and the pressure jump for the front interface corresponds to the dry version.This analysis shows that the liquid film acts as a memory of the liquid plug motion. Nevertheless, each back and forth motion of the liquid plug prescribes new values of the liquid film thickness. This means that this memory is a short term memory whose lifetime is a half cycle.

To summarize, the complete nonlinear system of equations that need to be

solved to determine the evolution of the plug is:

$$\Delta\tilde{P}_t = \begin{cases} 4\tilde{L_p}Ca + \left(3.72 + \frac{E^2}{2}\right)Ca^{2/3}, & \text{if } dry \\ 4\tilde{L_p}Ca + \left(3.72 + \frac{F^2}{2}\right)Ca^{2/3}, & \text{if } prewetted \end{cases} \tag{1.18}$$

$$F = 3^{1/3}\left(b_0 + b_1 log_{10}(A) + b_2\left[log_{10}(A)\right]^2 + b_3\left[log_{10}(A)\right]^3\right) \tag{1.19}$$

$$A = (3Ca)^{-2/3}\tilde{h_f} \tag{1.20}$$

$$\frac{d\tilde{X_r}}{d\tilde{t}} = Ca, \quad \tilde{X_f} = \tilde{X_r} + \tilde{L_p} \tag{1.21}$$

$$\frac{d\tilde{L_p}}{d\tilde{t}} = \left[\frac{(1-\tilde{h_r})^2}{(1-\tilde{h_f})^2} - 1\right]Ca \tag{1.22}$$

$$\tilde{h_r} = \frac{1.34Ca^{2/3}}{1 + 2.5 \times 1.34Ca^{2/3}} \tag{1.23}$$

$\tilde{h_f}(\tilde{X_f})$ is obtained from the memory of the liquid film deposition (1.24)

At each change of flow direction, the front meniscus becomes the rear meniscus and vice versa. The pressure balance in the dry and prewetted tubes share a relatively similar expression, but the coefficient E remains constant while F depends both on Ca and $\tilde{h_r}$. This system of equations is solved numerically with a first order Euler explicit method. Since the dynamics is accelerative, an adaptive time step refinement is used. It consists in keeping the spatial displacement over a time step constant: $\Delta\tilde{t} = \Delta\tilde{x}/Ca$ with $\Delta\tilde{x}$ constant. Convergence analysis on $\Delta\tilde{x}$ was performed for the calculations presented in this chapter.

1.3.3 Validation of the model for unidirectional pressure forcing in a dry capillary tube

Magniez & al. [97] validated the constitutive laws summarized in the previous section through careful comparison with experiments of the motion of liquid plugs in *prewetted* capillary tubes driven by a constant pressure head. This section is dedicated to the validation of the constitutive laws for the motion of liquid plugs in *dry* capillary tubes driven by an unidirectional pressure driving

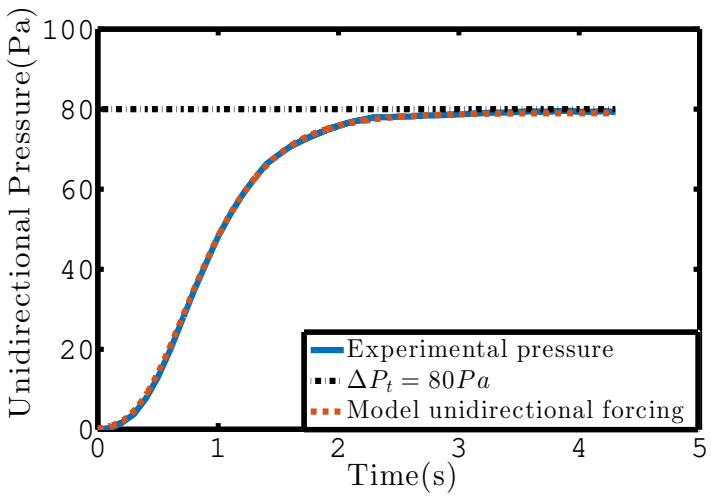

Figure 1.10 – Unidirectional pressure forcing imposed by the pressure controller. Blue solid line: pressure magnitude measured with an integrated pressure sensor. Red dashed line: approximation of the pressure driving by the so-called Gompertz function $\Delta P_t = 78\exp(-6\exp(-3t))$ used in the simulations as the driving pressure head since it fits well with the experimental signal. Black dashed-dotted line: asymptote $\Delta P_t = 80$ Pa when $t \to \infty$.

(represented on Fig. 1.10) and in particular the determination of the Hoffman-Tanner constant E (an essential parameter in the analytical model). om

In such configuration (Fig. 1.11), the deposition of a trailing film behind the plug leads to the reduction of the plug length (see Fig. 1.11b) and eventually its rupture when the front and rear interface meet (see Fig. 1.11a at time $t = 3$ s). This process is unsteady and highly accelerative as seen on Fig. 1.11c. From $t = 0$ to $t = 2$ s, this acceleration is mostly related to the increase in the pressure head (see Fig. 1.10). After $t = 2$ s, the acceleration goes on and is even exacerbated close to the plug rupture, while the pressure head reaches a plateau. This behavior can be understood by rewriting equation 1.18 under a form reminiscent of Ohm's law: $\Delta\tilde{P}_t = \tilde{R}_t Ca$, with $\tilde{R}_t = (\tilde{R}_v + \tilde{R}_i^r + \tilde{R}_i^f)$ the dimensionless global resistance to the flow, $\tilde{R}_v = 4\tilde{L_p}$, $\tilde{R}_i^f = E^2/2\ Ca^{-1/3}$ and $\tilde{R}_i^r = 3.72\ Ca^{-1/3}$ the viscous, front and rear interface resistances respectively. From this form of the pressure balance, we see that the reduction of the plug length $\tilde{L_p}$ leads to a reduction of the viscous

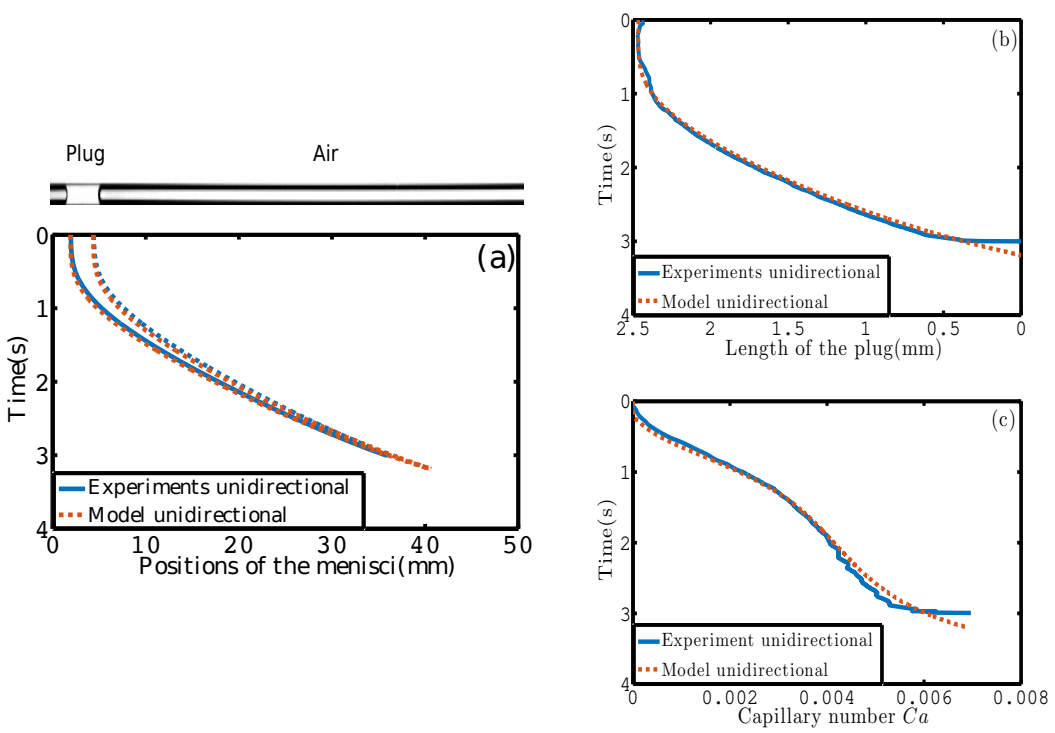

Figure 1.11 – Temporal evolution of a liquid plug of initial length $L_0 = 2.5mm$ pushed with a unidirectional driving pressure (represented on Fig. 1.10) in a dry capillary tube.
(a) Position of the rear and front meniscus.
(b) Evolution of the plug length.
(c) Evolution of the plug dimensionless speed, i.e. the capillary number Ca.
Blue curves correspond to experiments and the red dashed curves are obtained from simulations of equations 1.18 to 1.24.

resistance $\tilde{R_v}$ and thus, at constant pressure driving $\Delta\tilde{P_t}$, to an increase of the capillary number. This increase in the capillary number is strengthened by a decrease of the interfacial resistance $\tilde{R_i} = \tilde{R_i^f} + \tilde{R_i^r}$, since $\tilde{R_i}$ is proportional to $Ca^{-1/3}$. Finally, the increase of the trailing film thickness with the capillary number (equation 1.23) implies that the whole process (fluid deposition and plug motion) accelerate progressively as can be seen on Fig. 1.11. It is important to note that in these experiments the acceleration of the plug does not rely on inertial effects (which can be neglected according to the dimensional analysis

provided in section 1.3.1) but rather on the intimate relation between the plug size and velocity.

Many experiments have been performed for different initial plug lengths and compared with the numerical solutions of equations (1.18) to (1.24) (dry version with $\tilde{h_f} = 0$). In the simulations, a Gompertz function $\Delta P_t = 78\exp(-6\exp(-3t))$ was used as the driving pressure head due to its excellent match with the pressure head measured experimentally at the exit of the the pressure controller with an integrated pressure sensor (see Fig. 1.10, blue line corresponds to experimental signal and red line to best fit with Gompertz function). The complex shape of the pressure head is the result of the pressure controller response time (the command is a constant pressure $P_o = 80\ Pa$ starting at $t = 0$). The only adjustable parameter in the model is the Hoffman-Tanner constant E appearing in equation (1.18). The best fit between experiments and theory was achieved for $E = 4.4$, a value close to the coefficient 4.3 obtained by Bico & Quéré [155] in their experiments on falling of liquid slugs in vertical dry capillary tubes. With this value, an excellent prediction of the plug dynamics is achieved for all experiments (see e.g. Fig. 1.11 where blue solid lines correspond to experiments and red dashed lines to simulations). In particular, this model enables a quantitative prediction of the rupture length, defined as the portion of the tube $L_d = max(X_f) - min(X_r)$ visited by the liquid plug before its rupture (see Fig. 1.12a), and the rupture time, which is the total time elapsed between the beginning of the experiment and the plug rupture (see Fig. 1.12b).

1.4 Cyclic forcing of liquid plugs

This section is dedicated to the dynamics of liquid plugs under cyclic forcing. In the first subsection, the influence of the forcing configuration (pressure of flow rate) is examined. The second subsection enlightens the fundamental role played by hysteretic effects resulting from fluid deposition on the walls.

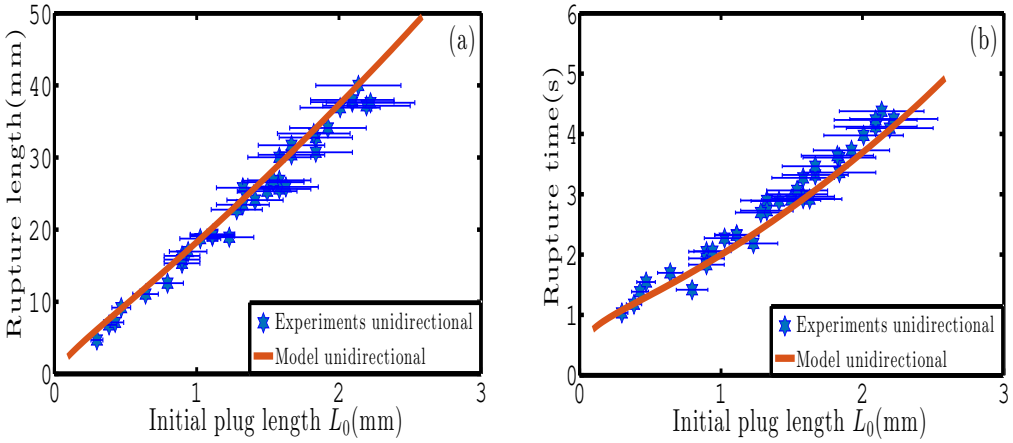

Figure 1.12 – Evolutions of liquid plugs pushed with a unidirectional pressure head of the form $\Delta P_t = 60\exp(-6\exp(-3.5t))$ in a dry capillary tube as a function of the initial plug length L_0:
(a) Evolution of the rupture length.
(b) Evolution of the rupture time.
The blue stars represent experiments. The red curve is obtained numerically by simulating the evolution for 107 initial plug lengths.

1.4.1 Influence of the driving condition: pressure head versus flow rate

In this first subsection, the responses of liquid plugs to two types of forcings are compared: (i) a cyclic flow rate imposed by a syringe pump (represented on Fig. 1.13a, blue line) and (ii) a pressure cycle imposed by a pressure controller (represented on Fig. 1.13b, blue line). These forcings have a complex temporal shape owing to the response time of the syringe pump and pressure controller. In section 1.2, we describe precisely how this forcing conditions are obtained. The pressure forcing is well approximated by the following analytical expression, which is a combination of Gompertz functions (see Fig. 1.13b, red dashed line):

$$\begin{cases} \Delta P_t = 78\exp(-6\exp(-3t)) \text{ for } t \in [0, T] \\ \Delta P_t = (-1)^n (P_c - P_d) \text{ for } t \in [n, (n+1)T] \\ P_c = 78\exp(-3\exp(-3(t-nT))) \\ P_d = 78\exp(-1.4(t-nT))\exp(-0.02 * \exp(-1.4 * (t-nT))) \end{cases} \tag{1.25}$$

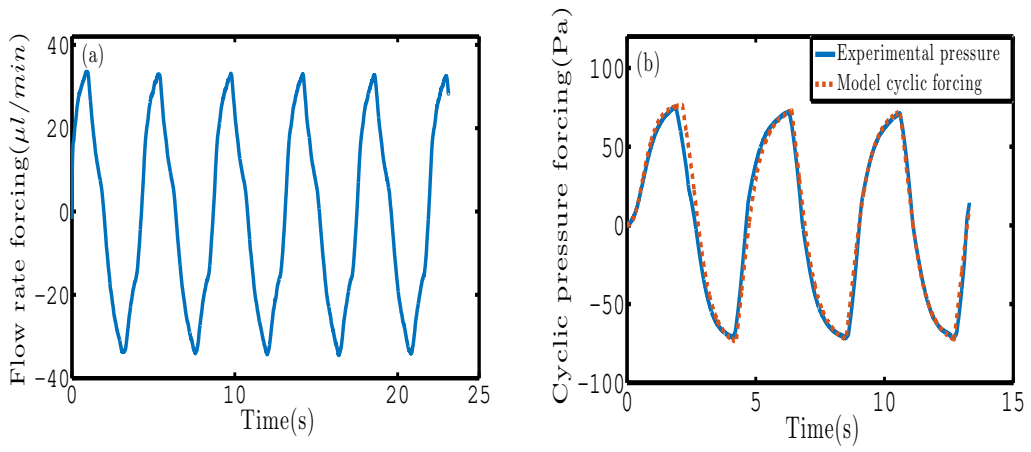

Figure 1.13 – Cylic driven forcings imposed experimentally with respectively a syringe pump and a pressure controller:
(a) Flow rate forcing.
(b) pressure cyclic forcing.
Blue solid line: experimental values measured with sensors. Red dashed line: fit of the pressure cyclic forcing measured experimentally with the analytical expression: $\Delta P_t = 78\exp(-6\exp(-3t))$ for $t \in [0,T]$, $\Delta P_t = (-1)^n(P_c - P_d)$ for $t \in [nT,(n+1)T]$ with $P_c = 78\exp(-3\exp(-3(t-nT)))$ and $P_d = 78\exp(-1.4(t-nT))\exp(-0.02\exp(-1.4*(t-nT)))$, $T = 2.15$ s the half period and $n \in \mathbb{N}^*$.

with $T = 2.15$ s the half period and $n \in \mathbb{N}^*$ for cyclic forcing.

Two extremely different behaviors are evidenced in these two cases: For a cyclic *flow rate* forcing (see Fig. 1.14a, b, c), the liquid plug dynamics is periodic and stable (see phase portrait on Fig. 1.15a). Indeed, the plug velocity and positions are directly imposed by the motion of the syringe pump, thus: $U(t+2T) = U(t)$ (see Fig. 1.14b) and $X_r(t+2T) = X_r(t)$ (see Fig. 1.14a). Moreover, since (i) the film deposition process solely depends on the plug velocity and (ii) the fluid recovery at half cycle N depends on the fluid deposition at half cycle $N-1$, the mass balance is null over each cycle and the evolution of the plug size is also periodic: $L_p(t+2T) = L_p(t)$ (see Fig. 1.14c). It is interesting to note that the initial wall wetting condition plays little role in this process; it only affects the mass balance during the first half cycle and thus determines the plug size $L_p((2n+1)T)$ with $n \in \mathbb{N}$. This wetting condition is indeed erased by the backward motion during the second half cycle and the plug evolution is then

only dictated by the temporal shape of the flow rate cycle.

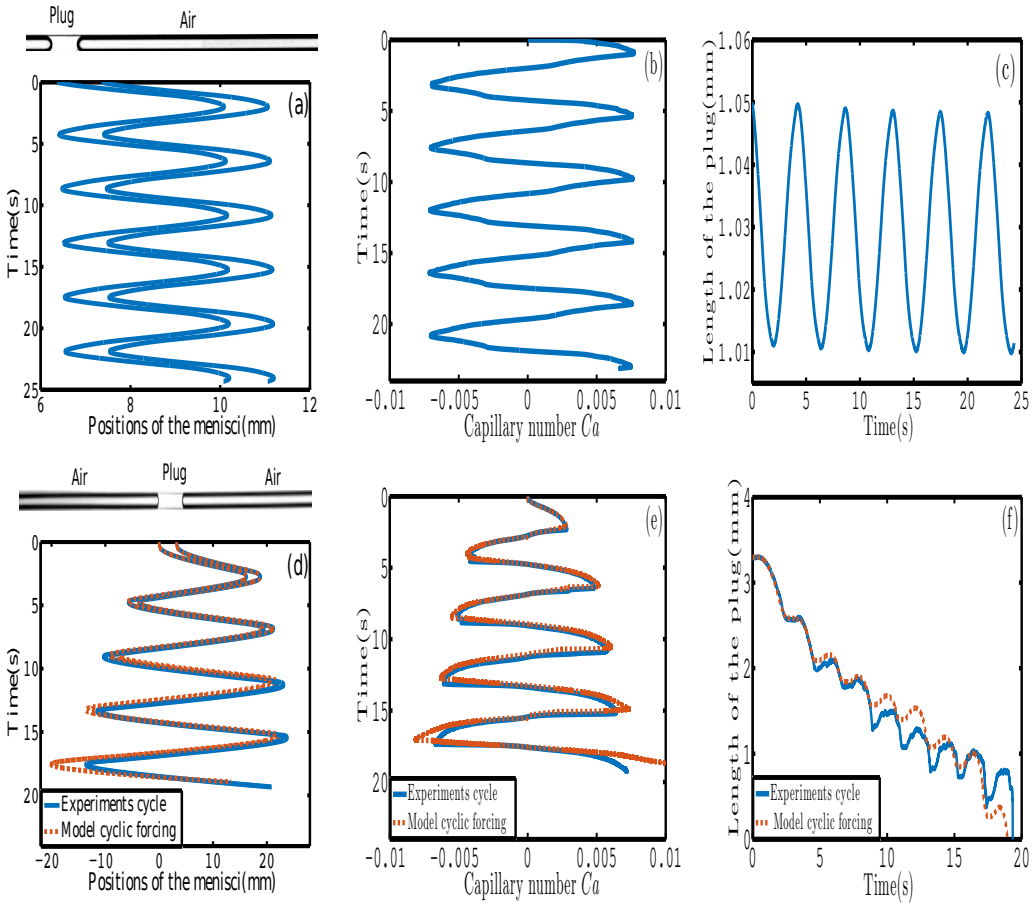

Figure 1.14 – Temporal evolutions of a liquid plug under two types of cyclic driving:
(a), (b), (c) Temporal evolution of a single liquid plug of initial length $L_0 = 1.05$ mm pushed with the cyclic flow rate forcing represented on Fig. 1.13a. (a) Positions of the menisci. (b) Evolution of the dimensionless velocity of the left meniscus (capillary number). (c) Evolution of the plug length.
(d), (e), (f) Temporal evolution of a single liquid plug of initial length $L_0 = 3.3$ mm pushed with the pressure cyclic forcing represented on Fig. 1.13d. (d) Position of the menisci. (e) Evolution of the dimensionless velocity of the left meniscus (capillary number). (f) Evolution of the plug length.
In all these figures blue lines represent experiments and red dashed lines simulations obtained from equations (Fig. 1.18) to (1.24).

The liquid plug undergoes a very different evolution for a periodic *pressure*

forcing (see Fig. 1.14d, e, f). In this case, the plug velocity and position are no more enforced by the driving condition and depend only on the evolution of the resistance of the plug to motion. For the forcing condition represented on Fig. 1.13b, it is observed that (i) the plug travels on a longer portion of the tube at each cycle (see Fig. 1.14d), (ii) the dimensionless velocity of the plug (the capillary number) is no more cyclic but increases progressively at each cycle, $U(t+2T) > U(t)$ (see Fig. 1.14e) and (iii) the size of the plug diminishes ($L_p(t+2T) < L_p(t)$), eventually leading to its rupture (see Fig. 1.14f). These phenomena are of course related since a larger plug velocity leads to more liquid deposition and thus a diminution of the plug size. Conversely, the cyclic diminution of the plug size leads to a decrease in the viscous resistance (the same process as described in subsection 1.3.3). Nevertheless this sole mechanism is not sufficient to explain the cyclic acceleration of the plug evidenced in the phase portrait (see Fig. 1.15b) as demonstrated in the next sections.

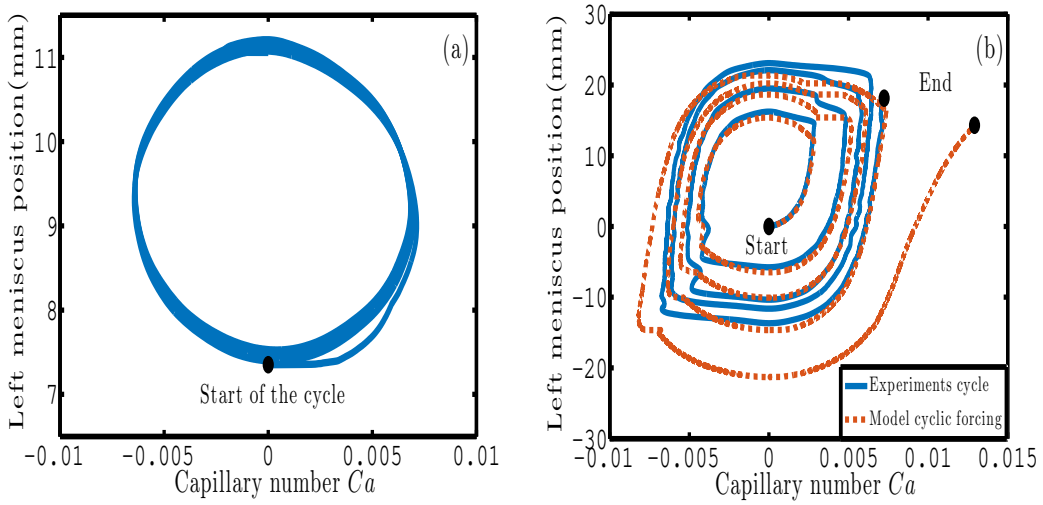

Figure 1.15 – Phase portrait showing the evolution of the position of the left meniscus as a function of the capillary number Ca:
(a) Cyclic flow rate forcing.
(b) cyclic pressure forcing.
The blue curves correspond to experiments and the red dashed line to simulations.

1.4.2 Memory effects and hysteretic behaviour

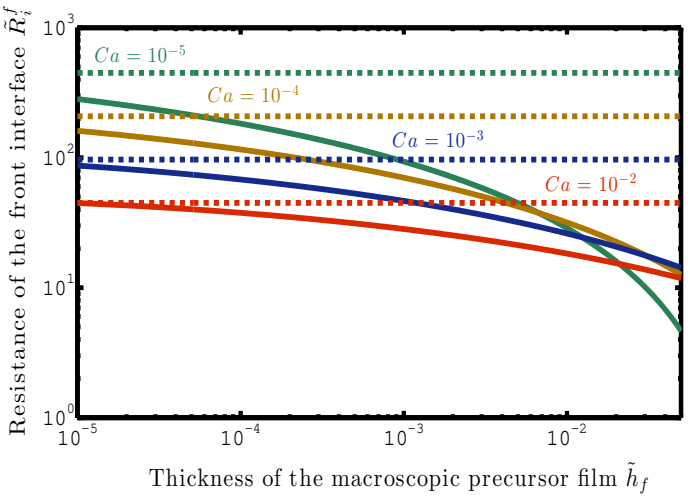

Figure 1.16 – Solid lines: dimensionless front interface resistance $\tilde{R}_i^f$ at different capillary numbers Ca as a function of the prewetting film thickness $\tilde{h}_f$. Dashed lines: dimensionless front interface resistance for dry capillary tubes. These curves show (i) that the interfacial resistance is systematically lower for prewetted capillary tubes than for dry capillary tubes and (ii) that for prewetted capillary tubes, the interfacial resistance decreases with the thickness of the prewetting film $\tilde{h}_f$

In this section, the model introduced in section 1.3.2 (equations (1.18)to (1.24)) is used to analyse the origin of the departure from a periodic evolution for a pressure forcing and in particular analyse the contributions of the different terms. Indeed, this model quantitatively reproduces the liquid plug dynamics (see Fig. 1.14d, e, f, red dashed lines, Fig. 1.15 and Fig. 1.12 for comparisons of the simulations and experiments for a large set of initial conditions).

The response of a liquid plug to a cyclic forcing is periodic since (i) the plug velocity is enforced and does not rely on the evolution of the plug resistance to motion and (ii) the liquid deposition on the walls, and thus the size of the plug solely depends on the plug velocity. This leads to a zero mass balance at each cycle.

For pressure driven cyclic forcing, the departure from this periodic behavior

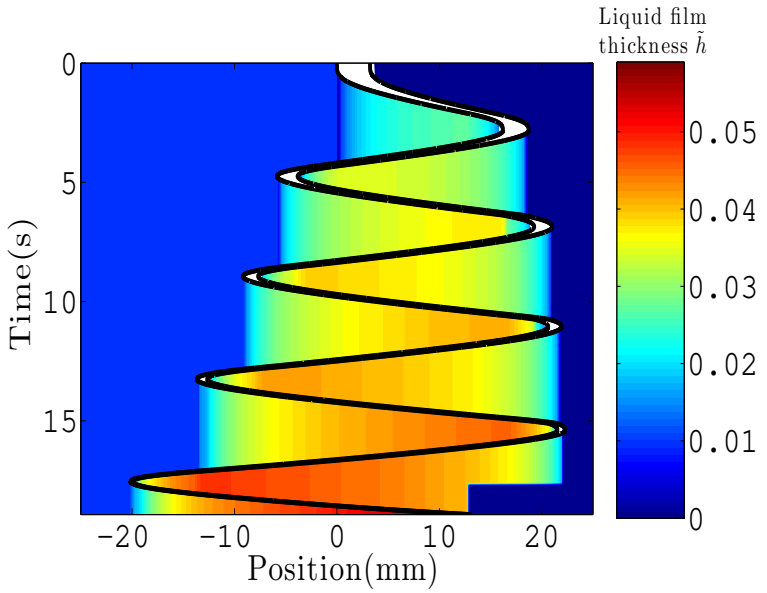

Figure 1.17 – Spatiotemporal diagram showing the evolution of the thickness of the liquid film deposited on the walls obtained from simulations of equations (1.18)to (1.24) with the same initial and forcing conditions as Fig. 1.14. The dimensionless film thickness $\tilde{h} = h/R$ is represented in color at each time and position in the tube.

thus relies on the evolution of the plug resistance at each cycle due to the existence of flow memories since the flow is quasi-static. *A first memory*, which is already at hand in unidirectional pressure forcing is simply the evolution of the plug length. Indeed, the plug size at a given time t depends on the history of the plug velocity at times $t^* < t$. In turn, the plug length modifies the viscous resistance $\tilde{R_v} = 4\tilde{L_p}$ and thus the plug velocity. The mass balance which is relatively simple for a unidirectional driving in a dry tube (the liquid left at time t on the walls only depends on the velocity of the plug at time t) becomes much more complex for a cyclic forcing. Indeed, at each back and forth motion, the liquid plug leaves on the walls a film layer whose thickness keeps a memory of the plug velocity during the corresponding half-cycle (since $\tilde{h_r}$ depends on Ca). Thus, the mass balance both depends on the velocity of the plug at time t and its velocity at the same position in the previous cycle. The progressive

transfer of mass from the liquid plug to the liquid film is clearly evidenced on Fig. 1.17. This graph shows that both the portion of the tube covered by the liquid film and the film thickness increase at each cycle. This graph also exhibits the complexity of the mass transfer: While the size of the plug gradually decreases at each cycle, its evolution is not monotonous during a half-cycle. Indeed, when the flow direction is changed the plug moves at first slowly (due to the response time of the pressure controller) and thus the thickness of the liquid film deposited on the walls behind the plug is smaller than the one in front of the plug, leading to a growth of the liquid plug. Then the plug accelerates and progressively the tendency is inverted leading to a reduction of the plug size. The transition between the growing and decreasing phases correspond on the graph to the times when the thickness (color) on each side of the plug is the same.

A second memory originates from the lubrication of the plug motion by the liquid film, i.e. the reduction of the front interface resistance $\tilde{R}_i^f = (F^2/2)Ca^{-1/3}$ as the thickness of the prewetting film $\tilde{h_f}$ is increased (see equation 1.20 and Fig. 1.16). Indeed, during the first half cycle the liquid plug moves on a dry capillary tube and leaves a liquid film behind it on the walls whose thickness increases with the speed of the liquid plug (see Fig. 1.17). This liquid film lubricates the passage of the plug during the back motion, leading to a drastic reduction of the front interface resistance (see Fig. 1.16) and thus, a higher plug speed. Then the same mechanism is reproduced during the following cycles: Since the speed is increased at each cycle, the plug leaves more liquid on the walls, leading again to a reduction of the interfacial resistance through a lubrication effect.

Of course, these two memory effects are coupled. To quantify the relative contribution of these two effects, we simulated the plug behavior when the viscous resistance $\tilde{R}_v$ is kept constant (see Fig. 1.18b) and when the front interface resistance $\tilde{R}_i^f$ is kept constant (see Fig. 1.18c). The simulations show that in these two cases the plug acceleration and rupture still occurs but that the rupture time is substantially increased. This tendency is confirmed on Fig. 1.19 where we compared the time necessary for the plug to rupture (called the "rupture time") to simulations for a large number of initial plug sizes when the whole model is considered (red solid line), when the first memory effect

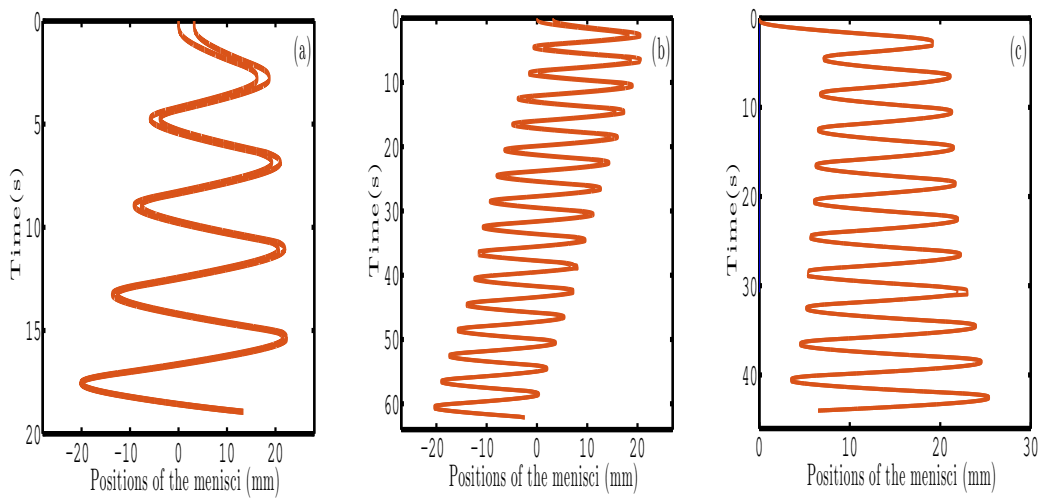

Figure 1.18 – Simulations with equations (1.18) to (1.24) of the positions of the menisci of a liquid plug of initial of size $L_0 = 3.3$ mm pushed with the cyclic pressure driving represented on 1.13(b):
(a) Complete models (equations (1.19) and (1.20)).
(b) The viscous resistance interface is kept constant $\tilde{R}_v = cste$.
(c) The front interface resistance is kept constant ($F = E$).

(length effect) is discarded (purple dashed line) and when the second memory effect (lubrication effect) is discarded (green dashed-dotted line). While the complete model quantitatively reproduces the tendencies, the other two simulations largely overestimate the rupture time.

This analysis also shows the central role played by the initial wetting condition: The successive accelerations at each half-cycle all originate from the transition between a dry and a prewetted capillary tube during the first cycle, which led to a massive acceleration of the plug in the back motion. In theory, the opposite behavior (plug cyclic slow down and growth) might be observed in a prewetted capillary tube depending on the thickness of the prewetting film and the amplitude of the pressure driving as was already observed by Magniez & al. [97] for unidirectional constant pressure forcing.

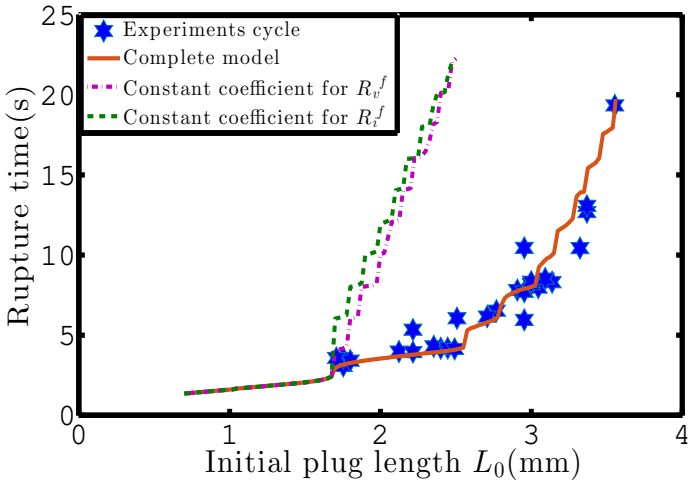

Figure 1.19 – Rupture time of liquid plugs pushed with a cyclic pressure driving given by equation (1.25) as a function of their initial lengths L_0. Blue stars correspond to experiments, the red solid curve to simulations with the complete model, the purple dashed-dotted line to simulations when the viscous resistance $\tilde{R}_v$ is kept constant and the green dashed-dotted line to simulations when the front interface resistance $\tilde{R}_i^f$ is kept constant and thus lubrication effects are discarded.

1.5 Cyclic motion vs direct rupture of the plug under pressure forcing

In this last section, we compare experimentally and theoretically the time and space required to break a liquid plug with either a unidirectional or a cyclic pressure forcing with the same magnitude. The two driving conditions used for this comparison are represented respectively on Fig. 1.10 and Fig. 1.13b. As previously mentioned, their temporal evolution can be approximated respectively by the Gompertz function $\Delta P_t = 78\exp(-6\exp(-3t))$ and the equations (1.25).

Figure 1.20 compares theoretically the dynamics of liquid plugs of increasing sizes for unidirectional and cyclic pressure driving. This figure shows (i) that plug rupture and thus airways reopening is obtained in a longer time but in a more confined space with a cyclic forcing compared to a unidirectional pressure

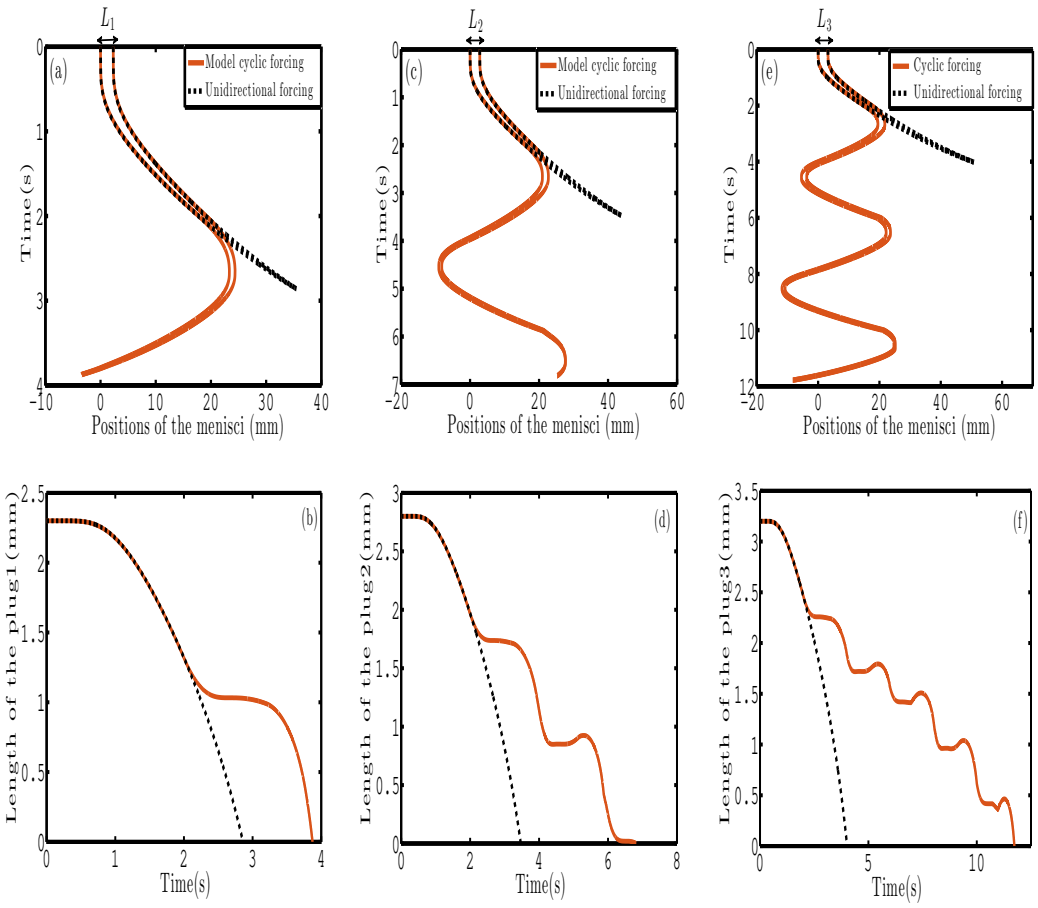

Figure 1.20 – Spatiotemporal evolution of plugs of initial lengths L_1 = 2.2 mm (a,b), L_2 = 2.8 mm (c,d) and L_3 = 3.2 mm (e,f) pushed either with a unidirectional pressure driving (black dotted line) or with a cyclic pressure driving (red solid line):
(a), (c), (e): Position of the rear and front menisci.
(b), (d), (f): Evolution of the plug size.

forcing and (ii) that the difference between these two driving conditions increases with the number of cycles and hence with the initial size of the liquid plug. This tendency has been verified experimentally and theoretically on a large number of initial plug lengths. The results are summarized in Fig. 1.21. Figures 1.21(a) and (b) show respectively the rupture length (the portion of the tube visited by the liquid plug before its rupture) and the rupture time (the time required for the plug to rupture) as a function of the plug initial length, L_0. In these

two figures, the blue stars and the solid red line correspond respectively to experiments and simulations for a *cyclic* pressure driving, while the black dots corresponds to simulations with a *unidirectional* pressure driving. The successive cycles are highlighted with different colors. This figure shows again excellent agreement between experimental data and numerical predictions for up to 5 cycles (Fig. 1.21), underlining that the model summarized in equations (1.18) to (1.24) captures the main physics.

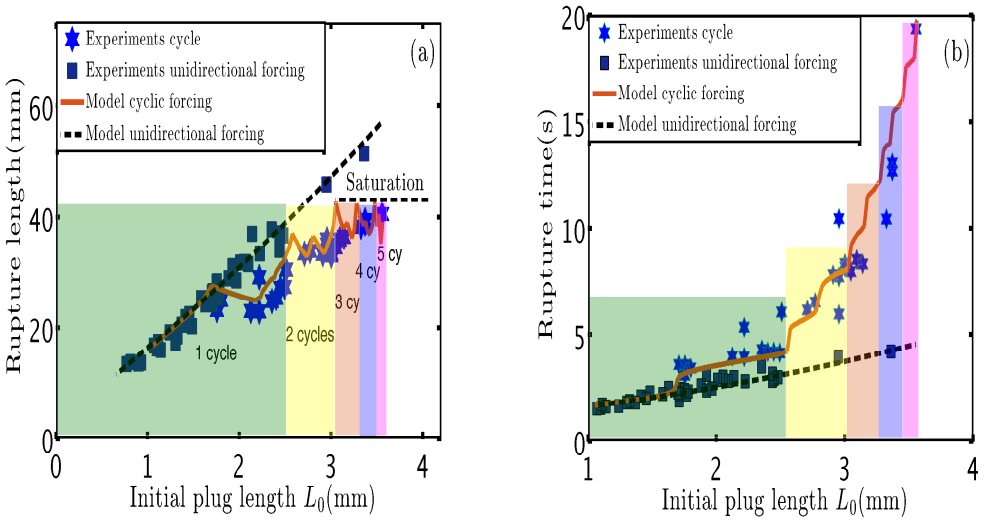

Figure 1.21 – Evolutions of liquid plugs pushed with a cyclic pressure driving given by equation (1.25) as a function of their initial lengths L_0:
(a) Evolution of the rupture length.
(b) Evolution of the rupture time.
Blue stars correspond to cyclic experiments and the red solid curve to simulations. The black dashed line and the blue square dots correspond respectively to simulations and experiments for a unidirectional pressure driving.

As long as the liquid plug breaks during the first half cycle, the cyclic forcing (red solid line) and the unidirectional forcing (black dotted line) are of course equivalent. When the plug starts going back (for initial length $L_0 \approx 1.7$ mm) brutal changes in the tendencies are observed: the rupture length starts decreasing (see Fig. 1.21a), while the increase in the rupture time is on the contrary exacerbated (see Fig. 1.21b). For larger plug lengths, the number of cycles required to achieve plug rupture increases rapidly. Since each change in the plug

flow direction is associated with some sharp fluctuations of the rupture length, this increase in the number of cycles leads to a saturation of the rupture length (see Fig. 1.21a). This is very different from the relatively linear trend predicted by our simulations (black dots) and observed experimentally on Fig. 1.12 for a unidirectional forcing. This saturation means that there is a maximal distance that a liquid plug can travel regardless of its size for a prescribed pressure cycle. An interesting point is that, despite this confinement, the plug rupture remains possible due to the hysteretic effects that enable a progressive acceleration of the liquid plug at each cycle, even if the liquid plug moves on the same portion of the tube.

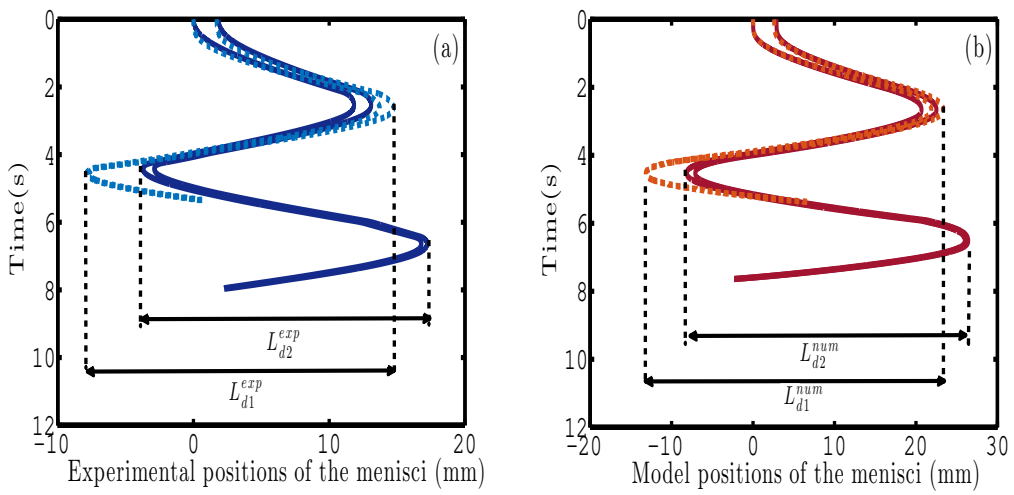

Figure 1.22 – Rupture lengths of two liquid plugs of close initial lengths pushed with a cyclic pressure driving:
(a) Experimental investigation.
(b) numerical investigation.
The initial length of the plug in dashed lines $L_1 = 2.5$ mm is smaller than the initial length of the plug in solid line $L_2 = 2.85$ mm but nevertheless travels on a larger distance $L_{d1} > L_{d2}$ before its rupture.

To understand the decrease in the rupture length observed when the flow direction is changed, we plotted the experimentally observed (Fig. 1.22a) and numerically predicted (see Fig. 1.22b) spatiotemporal diagrams of the evolution of two plugs with initial lengths $L_1 = 2.5$ mm and $L_2 = 2.85$ mm in a region

where the rupture length is decreasing when the initial plug length is increased. The experiments were performed with a different pressure driving magnitude $P_o = 60$ Pa than for Fig. 1.21. So the positions of these two points in the rupture length graph are represented on Fig. 1.23 (encircled points). In Fig. 1.22 the dashed lines corresponds to $L_1 = 2.5mm$ and the solid lines to $L_2 = 2.85$ mm. The experimental (Fig. 1.22a, blue line) and numerical trends (Fig. 1.22b, red line) are similar. These figures show that the largest plug requires less space to break than the smallest plug $L_{d1} > L_{d2}$. The origin of this rather counterintuitive behavior again lies in memory effects. Since these two plugs are pushed with the same pressure head, the smallest plug with the lowest bulk resistance moves faster, leaves more liquid on the walls than the bigger one and thus goes further during the first half-cycle. When the sign of the pressure head is inverted, the smallest liquid plug will move on a more prewetted channel and thus (i) it will travel faster (since lubrication effects reduce its resistance to motion) and (ii) it will recover more liquid, thus slowing down the plug size decrease through the mass balance. The combination of these two effects enables the plug to reach a deeper location in the tube.

On the other hand, a comparison between unidirectional and cyclic forcing indicates that more time is required to break liquid plugs for cyclic motion than straight motion (see Fig. 1.21b). This is simply the result of the mass balance. As the liquid plug moves back and forth on prewetted capillary tubes, it recovers some liquid while it doesn't when it moves only on a dry capillary tube. This slows down the plug size evolution.

Finally, a comparison of the evolutions of the rupture time and rupture length on Fig. 1.21 shows that the rupture time undergoes an exponential-like growth when the rupture length approaches the saturation zone (for length $L_o > L_s$) with $L_s \approx 2.4$ mm. To confirm this trend, we performed some numerical simulations of the rupture time and rupture length for three different time periods (see Fig. 1.24). For each period, the evolution is relatively similar and the semilog graph in Fig. 1.24b, indeed underlines that the rupture time follows an exponential growth (rupture time $\propto e^{x/L_c}$) for initial plug lengths larger than a critical length L_s. We calculated both the critical saturation length L_s and the characteristic

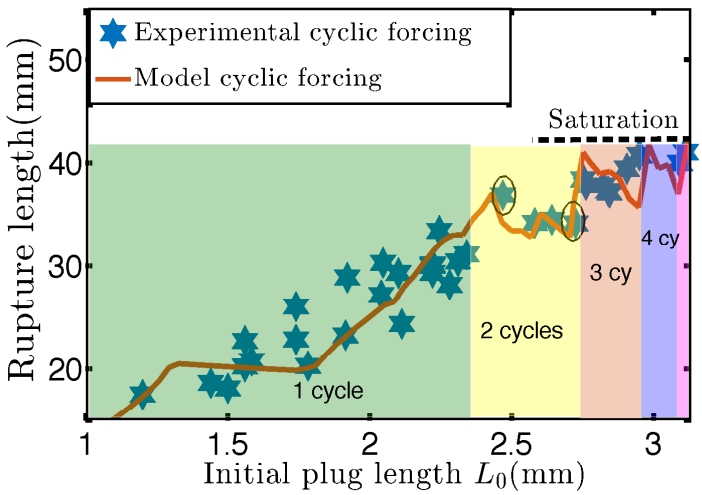

Figure 1.23 – Rupture length of a liquid plug pushed with a cyclic pressure driving given by the analytical function $\Delta P_t = 59\exp(-6\exp(-3.5t))$ for $t \in [0,T]$, $\Delta P_t = (-1)^n(P_c - P_d)$ for $t \in [nT,(n+1)T]$ with $P_c = 59\exp(-2.2\exp(-3.5(t-nT)))$ and $P_d = 59\exp(-1.1(t-nT))\exp(-0.06\exp(-1.1*(t-nT)))$, $T = 2.1$ s the half period and $n \in \mathbb{N}^*$. Blue stars correspond to experiments, the red curve is the result from our simulations. The encircled experimental points correspond to plugs of initial lengths $L_1 = 2.5$ mm and $L_2 = 2.85$ mm, whose evolutions are compared in Fig. 1.22.

length L_c for the three time periods $T = 2$s, 4s and 6s and found the values:

$$\text{Critical saturation lengths:} \quad L_{s2} \approx 1.6mm, \;\; L_{s4} \approx 2.4mm, \;\; L_{s6} \approx 3.4mm \quad (1.26)$$

$$\text{Characteristic lengths:} \quad L_{c2} \approx 0.6mm, \;\; L_{c4} \approx 0.7mm, \;\; L_{c6} \approx 0.8mm \quad (1.27)$$

These two factors depend on the time period T. This means that for each time period and pressure forcing, the rupture time becomes exponentially long when $L_o - L_s \gg L_c$ and the pressure driven plug dynamics asymptotes a stable periodic propagation.

As a conclusion of this section, large liquid plug breaking is achieved in a more confined space but in longer time with a cyclic forcing than with a unidirectional pressure forcing. Moreover, the rupture times grows exponentially when the plug initial length exceeds a critical length L_s, whose value depends on the

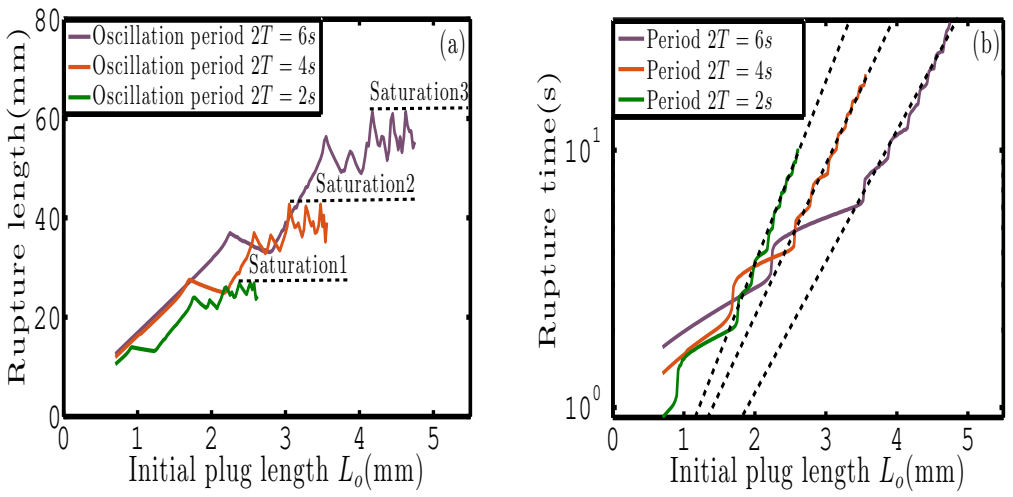

Figure 1.24 – Evolutions of liquid plugs pushed with a cyclic pressure driving given by equation (1.25) as a function of their initial lengths L_0 for 3 different time periods T = 2s, 4s and 6s:
(a) Evolution of the rupture length.
(b) Evolution of the rupture time.

cycle period. In this regime, the liquid plug dynamics becomes quasi-periodic.

1.6 Conclusion

Despite its occurence in practical situations such as pulmonary flows in pathological conditions, the specificity of the response of liquid plugs to cyclic driving has not been studied so far experimentally and theoretically. The present results show that the dynamics and rupture of a liquid plug strongly depends on the type of forcing. A flow rate cyclic forcing results in periodic oscillations of the plug and no rupture. On the contrary, a pressure cyclic forcing enables airway reopening through a progressive acceleration of the liquid plug dynamics and reduction of its size. This departure from a periodic response originates from two memory effects which decrease the resistance of the plug to motion at each cycle: (i) the cyclic reduction of the plug size which reduces the viscous resistance and (ii) a lubrication effect which reduces the front interface resistance. These two

coupled effects are strongly connected to the thickness of the liquid film lying on the walls, which keeps a memory of previous plug displacements. In addition, this study shows that the rupture of a liquid plug with a prescribed pressure cycle is a spatially bounded phenomenon regardless of the initial plug length. In other words, large plug can be ruptured in a limited space with a cyclic forcing, while more and more space is required to break plugs of increasing size with a unidirectional forcing. The trade-off is that more time is nevertheless required and that this time grows exponentially above a critical length, which depends on the cycle period and the applied pressure.

The analysis of the underlying physics was achieved through a comparison of extensive experimental data to a reduced dimension model. This model quantitatively predicts the plug behavior for the numerous pressure cycles studied in this chapter. Moreover it is in principle valid for any pressure cycle in the visco-capillary regime (low capillary, Reynolds and Bond numbers). Combined with constitutive laws for the plug divisions at bifurcation, it might serve as a basis to simulate cyclic plug dynamics in more complex geometries, or even the dynamics of mucus plugs in distal pulmonary airways. In this last case however, complementary elements such as the influence of walls elasticity, the non-Newtonian fluid properties of mucus, or the presence of an initial mucus layer on the walls should be implemented to achieve realistic simulations. In particular, it is envisioned that the presence of a prewetting film on the walls might lead to either plug ruptures or persistent occlusions as was demonstrated by Magniez & al. [97] for unidirectional driving. Complete models of plug dynamics would open tremendous perspectives, such as the "virtual testing" of new strategies to improve airways clearance for patients suffering from chronic obstructive pulmonary disease or cystic fibrosis. But it might also open perspectives to design robust pressure controllers that enable stable control of liquid plugs. Indeed, the instability to breaking is a major drawback to manipulate plugs with pressure controllers.

Chapter 2

Critical pressure necessary for airway reopening

Abstract

In this chapter, we investigate theoretically and numerically the critical pressure necessary to reopen prewetted obstructed airways under complex (non-constant) driving conditions. For realistic cyclic driving, it is shown that depending on the thickness of the prewetting liquid film and the magnitude of the pressure driving, the behavior of the plug can be either accelerative with a progressive decrease of its length at each cycle and eventually leading to its rupture or conversely, decelerative associated with plug growths and therefore, worsening of the airway obstruction. In particular, we are able to identify pressure thresholds for the transition between these two regimes for physiologically relevant forcing. This study allows a deeper comprehension of liquid plugs response to breathing cycles and underlines the importance of considering a complete geometry model of the pulmonary tree including interactions in the network through bifurcations and the wall properties.

2.1 Method

In this chapter, we consider a liquid plug of initial length L_0 driven by a time dependent pressure head ΔP_t in a capillary tube of radius R prewetted by an initial liquid film of thickness h_0. X_r and X_f correspond to the positions of the rear and front interfaces (menisci), with $L_p(t) = X_f - X_r$ the plug length at time t, and h_f and h_r to the thicknesses of the wetting film in front and behind the plug.

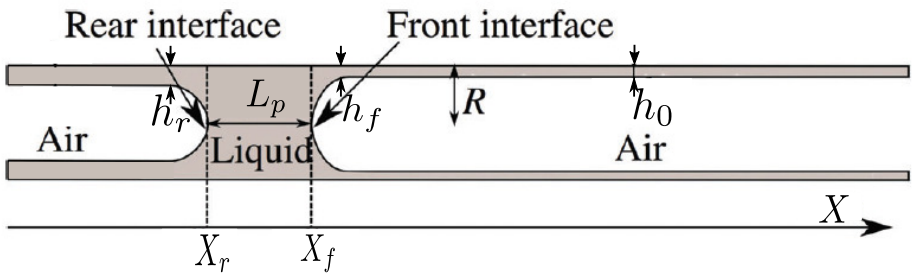

Figure 2.1 – Sketch of a liquid plug in a prewetted capillary tube adapted from [97].

This theoretical study is based on the model developed in chapter 1 in the case of a prewetted capillary tube, which can be written under dimensionless form [97]:

$$\Delta \tilde{P}_t = 4\tilde{L_p}Ca + \left(3.72 + \frac{F^2}{2}\right)Ca^{2/3} \tag{2.1}$$

$$\frac{d\tilde{X}_r}{d\tilde{t}} = Ca, \quad \tilde{X}_f = \tilde{X}_r + \tilde{L_p} \tag{2.2}$$

$$\frac{d\tilde{L_p}}{d\tilde{t}} = \left[\frac{(1-\tilde{h_r})^2}{(1-\tilde{h_f})^2} - 1\right]Ca \tag{2.3}$$

$$\tilde{h_r} = \frac{1.34Ca^{2/3}}{1 + 2.5 \times 1.34Ca^{2/3}} \tag{2.4}$$

with $F = 3^{1/3}\left(b_0 + b_1 log_{10}(A) + b_2 [log_{10}(A)]^2 + b_3 [log_{10}(A)]^3\right)$ and $A = (3Ca)^{-2/3}\tilde{h_f}$

2.2 Constant unidirectional pressure driving

The response of a liquid plug driven by a constant pressure difference in a prewetted channel was investigated experimentally, theoretically and numerically in [151, 98, 97]. The plug dynamics strongly depends on the thickness of the prewetting liquid film h_0 and the magnitude of the pressure driving. Two important regimes can be distinguished as shown experimentally and theoretically by [97]:

- A regime of *acceleration*, wherein the liquid plug leaves more liquid on the walls behind it than it recovers from the prewetting film ($\tilde{h_r} > \tilde{h_f} = \tilde{h_0}$). In this case, the length of the plug decreases, eventually leading to its rupture.
- A regime of *deceleration*, in which the plugs leaves less liquid on the walls behind it than it recovers from the prewetting film ($\tilde{h_r} < \tilde{h_f} = \tilde{h_0}$). In this case, the plug size increases and the plug slows down.

The transition between the two regimes occurs at a critical pressure $\Delta\tilde{P_c}$ related to an equal balance between the precursor and the trailing liquid films thickness ($\tilde{h_r} = \tilde{h_f} = \tilde{h_0}$) leading to ($d\tilde{L_p}/d\tilde{t} = 0$). A critical capillary number was derived from equation 1.23 by Magniez & al. [97]) in this case:

$$Ca_c = \left(\frac{\tilde{h_f}}{1.34(1 - 2.5\tilde{h_f})} \right)^{3/2} \tag{2.5}$$

Since the evolution of the plug is monotonous, equation 2.5 combined with equation 2.1 enables to predict the pressure necessary for airway reopening depending on the precursor liquid film thickness: $\Delta\tilde{P_c} = \Delta\tilde{P_t}(Ca_c, \tilde{L_0}, \tilde{h_0})$. If the driving pressure is greater than the critical pressure ($\Delta\tilde{P_t} > \Delta\tilde{P_c}$), we observe an acceleration of the liquid plug and conversely, if the driving pressure is smaller than the critical pressure, ($\Delta\tilde{P_t} > \Delta\tilde{P_c}$) we observe a deceleration of the liquid plugs as shown in Fig 2.3.

The evolution of the critical pressure $\Delta\tilde{P_c}$ as a function of the prewetting film thickness $\tilde{h_0}$ is represented on Fig. 2.2 for an initial length $L_0 = 5R$.

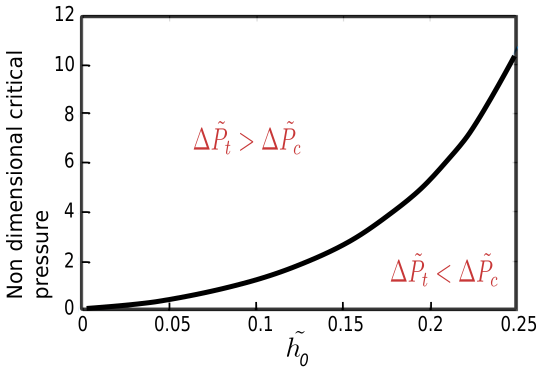

Figure 2.2 – Critical pressure for the transition of regimes of a liquid plug of initial length $\tilde{L_0} = 5$ in a capillary tube covered with prewetting liquid films of different thickness $\tilde{h_0}$.

The acceleration regime is characterised by the temporal reduction of the plug length (see Fig 2.3b), which further reduces the viscous resistance leading to a highly accelerative evolution (see Fig 2.3c). Since the critical pressure $\Delta\tilde{P}_c = \Delta\tilde{P}_t(Ca_c)$ depends linearly on the plug length (Eq. 2.1), this leads to a reduction of the critical pressure away from the driving pressure (see Fig 2.3d). This regime eventually leads to the plug rupture (see Fig 2.3a). As we keep the initial liquid film thickness constant $\tilde{h_0} = 0.04$, a reduction of the driving pressure leads to a deceleration regime when $\Delta\tilde{P}_c < \Delta\tilde{P}_t$, characterised by an increase in the plug length (Fig 2.3f), inducing an increase in the viscous resistance which in turns slows down the plug (see Fig. 2.3) and increases the critical pressure. For constant pressure driving, the critical pressure always evolve away from the pressure driving, so that no transition can occur between the acceleration and deceleration regimes.

To investigate physiologically relevant regimes, we must consider complex cyclic driving such as the one represented on Fig. 2.4. Such complex signal has a time-dependent amplitude and is cyclic. To understand the role play by these two components of the signal, we will first study the response of liquid plugs to time-dependent unidirectional pressure driving and then cyclic driving with constant magnitude. Finally, we will study the response of liquid plugs to

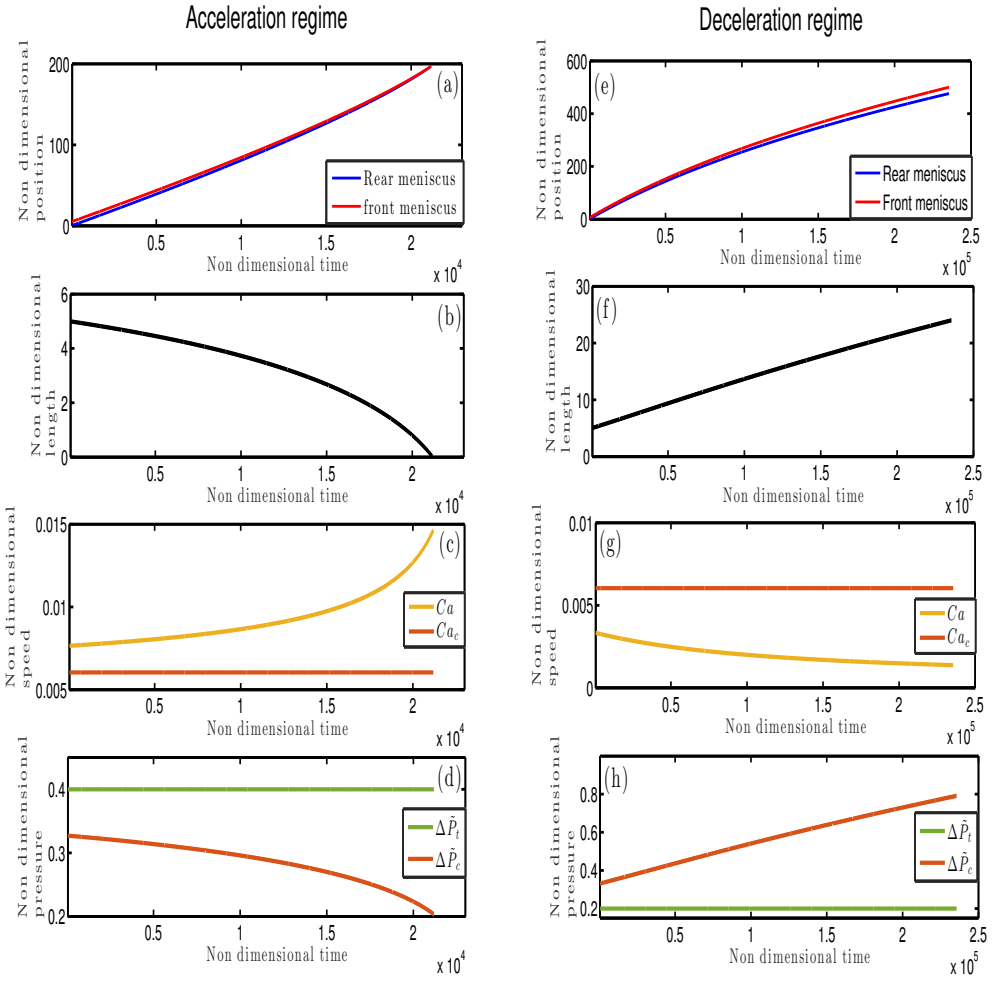

Figure 2.3 – Temporal evolution of the dynamics of a liquid plug of initial length $\tilde{L_0} = 5$ in a capillary tube prewetted by a liquid film of thickness $\tilde{h_0} = 0.04$ under the driving pressure $\Delta\tilde{P} = 0.4$ in the acceleration regime and $\Delta\tilde{P}_t = 0.2$ in the deceleration regime:
(a-e) Position of the menisci.
(b-f) Evolution of the length of the plug.
(c-g) Evolution of the non dimensional speed of the plug Ca.
(d-h) Evolution of the pressure.
The critical capillary number and the critical pressure appear in red in Figure (c-g) and (d-h)respectively.

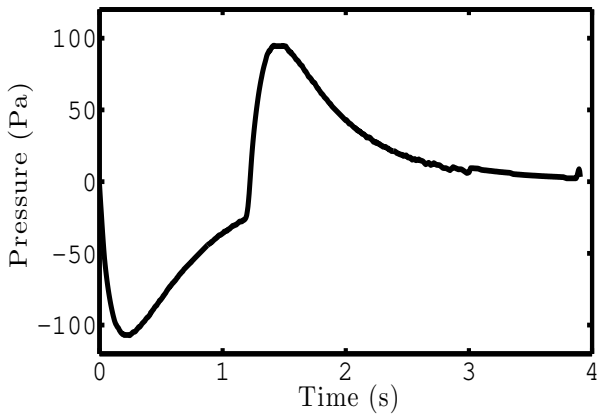

Figure 2.4 – Alveolar pressure during a quiet breathing cycle [8].

realistic pressure driving.

2.3 Time dependent unidirectional pressure driving

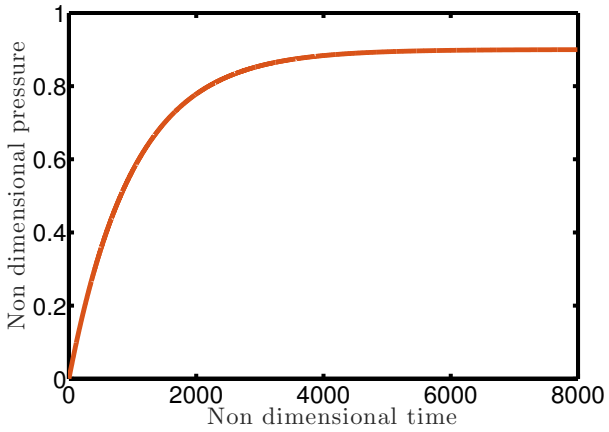

Figure 2.5 – Unidirectional time dependent pressure driving $\Delta\tilde{P}_t = \tilde{P}_0(1 - exp(-\tilde{t}/\tilde{\tau}))$ with $\tilde{P}_0 = 0.9$ and $\tilde{\tau} = 10^3$.

In this section we consider a simple time dependent exponential driving of the form $\Delta\tilde{P}_t = \tilde{P}_0(1 - exp(-\tilde{t}/\tilde{\tau}))$ in which $\tilde{t}$ and $\tilde{\tau}$ are respectively the non dimensional values of the time and transient time. The asymptotic value $\tilde{P}_0$ is

reached when $t \to \infty$ as shown in Fig. 2.5.

2.3.1 Transition between different flow regimes

An increase in the magnitude $\tilde{P_0}$ of the pressure driving while keeping the transient time $\tilde{\tau}$ and the initial prewetting liquid film thickness $\tilde{h_0}$ constant leads to the observation of three different flow regimes as shown in Fig. 2.6: (i) a *deceleration regime*, (ii) an intermediate regime, that we call *induced deceleration regime* and (i) an *acceleration regime*.

The *deceleration regime* occurs when the magnitude $\tilde{P_0}$ is lower than the initial critical pressure $\tilde{P}_{co}(\tilde{h}_0, \tilde{L}_0)$ (see Fig. 2.6d). In this case, and despite the progressive increase in the driving pressure, the liquid plug always remain in the *deceleration regime* which is characterised by a low capillary number compared to the critical capillary number (see Fig. 2.6c) and a plug growth (see Fig. 2.6a, b). In this regime, we recover the behavior already observed at constant driving pressure: a critical pressure increasing over time principally due to the plug growth, while the critical capillary number remains constant because it solely depends on the prewetting liquid film thickness $\tilde{h}_0$.

The so-called *induced deceleration regime* occurs at moderate magnitude $\tilde{P_0}$ in which, though the magnitude slightly overcomes the initial critical pressure $\tilde{P}_{co}$, it is not enough to reverse the tendency, and the plug remains in the deceleration regime. This regime is explained by the evolution of the critical pressure during the transient regime (between $\tilde{t} = 0$ and $\tilde{t} = 5\tilde{\tau}$). Within this time period, the driving pressure remains below the critical pressure, the liquid plug grows, which in turns increases the critical pressure (see Fig. 2.6d). Thus, when the maximum driving pressure is reached $\Delta\tilde{P}_t = \tilde{P_0}$, it remains below the new value of the critical pressure and the acceleration regime is never reached.

Finally, the *acceleration regime* occurs when the pressure driving magnitude $\tilde{P_0}$ significantly overcomes the initial critical pressure. This regime is characterised at first by a slight plug growth and a low capillary number when ($\tilde{t} < 2\tilde{\tau}$) and is rapidly followed by an increase in the capillary number and a diminution of the plug length, which eventually leads to the plug rupture.

The transient region makes more complex the prediction of the transition

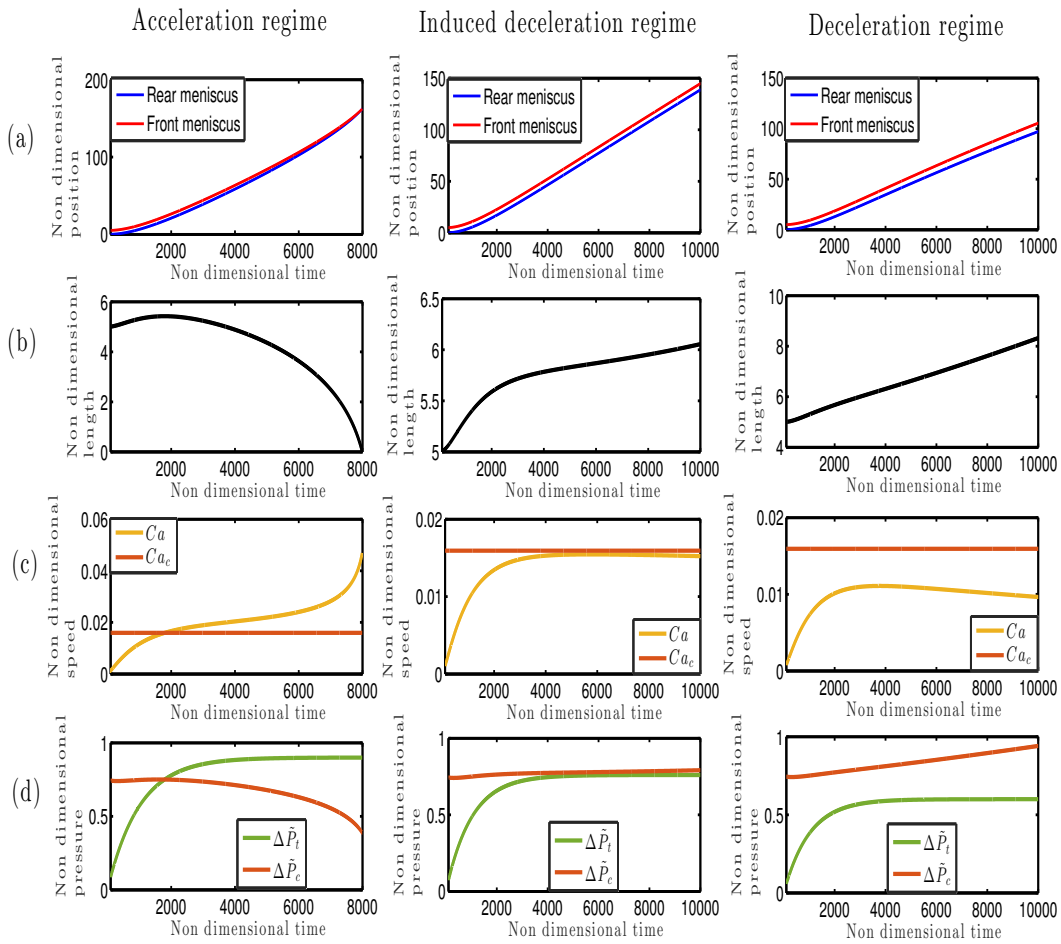

Figure 2.6 – Temporal evolution of a liquid plug of initial length $\tilde{L_0} = 5$ in a capillary tube prewetted by a liquid film of dimensionless thickness $\tilde{h_0} = 0.07$ under a driving pressure of the form $\Delta\tilde{P}_t = \tilde{P}_0(1 - exp(\tilde{t}/10^3))$. Left column: pressure magnitude $\tilde{P}_0 = 0.9$, acceleration regime. Center column: $\tilde{P}_0 = 0.76$, induced deceleration regime. Right column: $\tilde{P}_0 = 0.6$, deceleration regime.
(a) Positions of the rear and front menisci.
(b) Evolution of the plug length.
(c) Evolution of the non dimensional speed of the plug Ca.
(d) Evolution of the pressure.
The critical capillary number and the critical pressure appear in red in figures (c) and (d) respectively.

between the acceleration and deceleration regime. However, the magnitude of the pressure driving $\tilde{P_0}$ and the initial prewetting liquid film thickness $\tilde{h_0}$ still remain the key parameters.

2.3.2 Influence of the main parameters

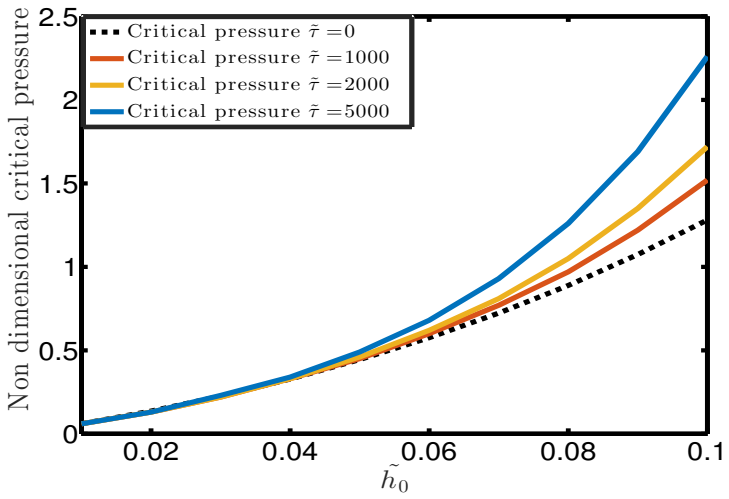

Figure 2.7 – Critical pressure for the transition between the acceleration regime and the deceleration for $\tilde{\tau} = 0, 1000, 2000, 4000$.

The influence of the prewetting liquid film $\tilde{h_0}$ and the transient time $\tilde{\tau}$ are presented in Fig. 2.7, in which the critical pressure is plotted as a function of the prewetting liquid film thickness $\tilde{h_f}$ for four transient times pressure driving ($\tilde{\tau} = 0, 1000, 2000, 4000$).

As expected, the critical pressure is lower for constant pressure driving ($\tilde{\tau} = 0$) and further increases when the transient time $\tilde{\tau}$ is increased. Indeed, the critical pressure is increased during the transient region owing to the increase in the plug size. However, at low values of the prewetting liquid film ($h_0 < 0.04$), all the curves converge, which means that the effects of the transient time can be neglected. Indeed, the evolution of the critical pressure during the transient time is linked to the increase in the plug size within this time period, which is lowered when the prewetting film is thin.

2.4 Cyclic rectangular pressure driving

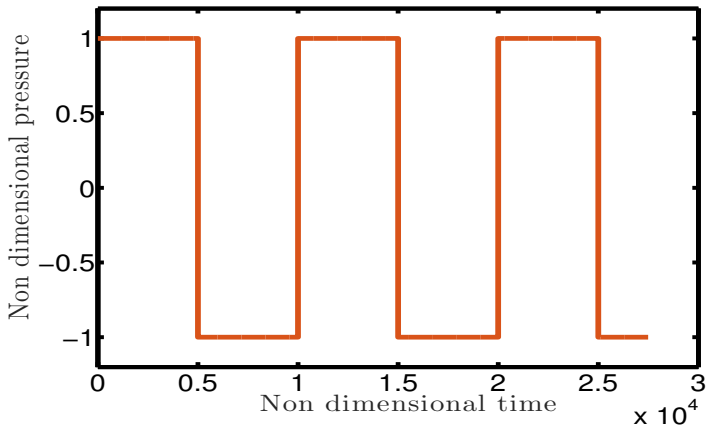

Figure 2.8 – Rectangular cyclic pressure driving of magnitude $\Delta\tilde{P}_t = 1$ and period $\tilde{T} = 10^4$.

In this section, we investigate the effect of cyclic pressure forcing on the dynamics of the plug. To isolate the effect of the change in the flow direction, we consider a signal of constant magnitude (see Fig 2.8).

2.4.1 Flow regimes

Three regimes are observed when a plug is driven by a cyclic pressure driving of constant magnitude (see Fig. 2.9):

(i) A *rupture acceleration regime* at high pressure magnitude leading to the plug rupture.

(ii) A *saturated acceleration regime* at intermediate pressure magnitude characterised by a diminution of the plug length, which however tends towards a saturation value. In this situation, the plug starts accelerating but since the pressure magnitude ($\Delta\tilde{P}_t = 0.45$) is close to the critical pressure introduced in the previous section, the liquid plug reaches a situation of equal mass balance between the liquid film recovered from the prewetting film and left behind it ($\tilde{h_f} = \tilde{h_r}$) all over the successive cycles. Thus the plug dynamics eventually converges toward a stable periodic oscillating state with a constant value of the

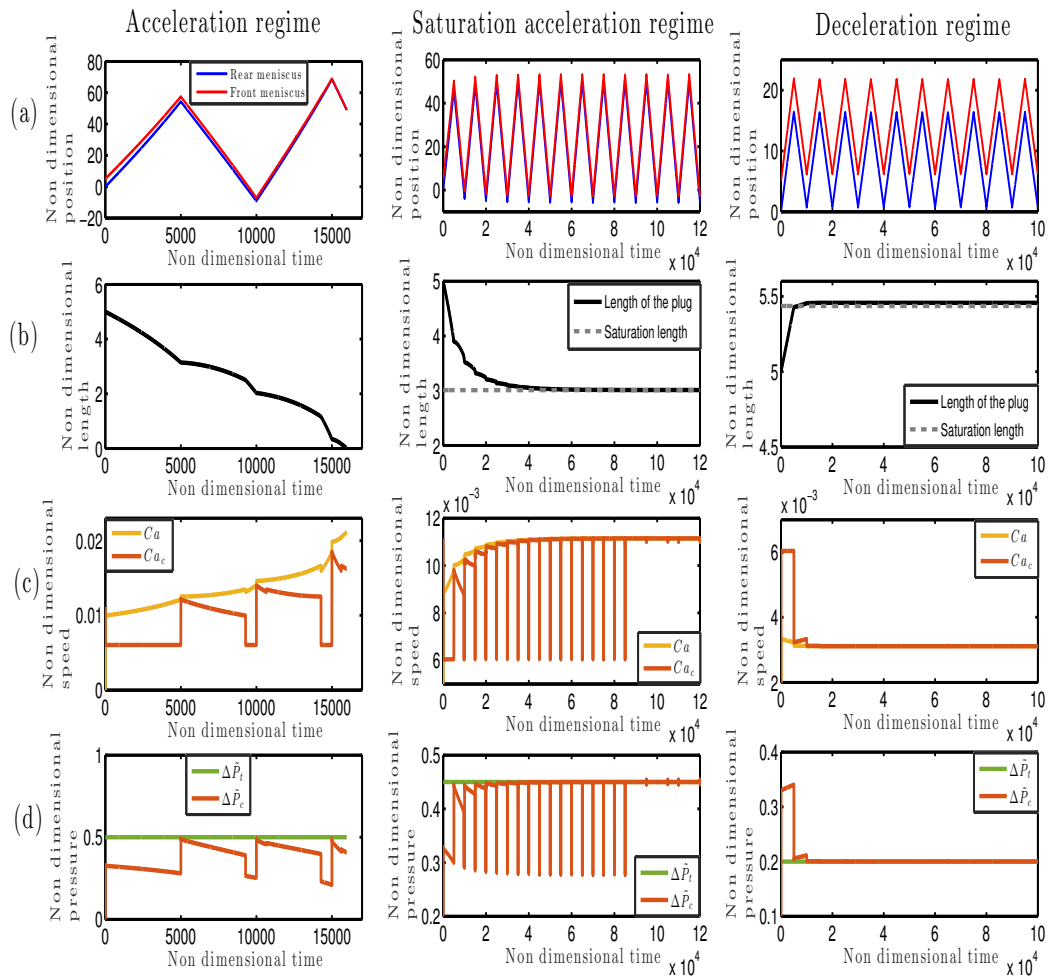

Figure 2.9 – Temporal evolution of a liquid plug of initial length $\tilde{L_0} = 5$ in a capillary tube prewetted by a liquid film of dimensionless thickness $\tilde{h_0} = 0.04$ under a driving pressure of the form presented in Fig. 2.8. Left: driving pressure magnitude $\Delta\tilde{P}_t = 0.5$, acceleration regime. Center: $\Delta\tilde{P}_t = 0.45$, saturation acceleration regime. Right: $\Delta\tilde{P}_t = 0.2$, deceleration regime.
(a) Positions of the menisci.
(b) Evolution of the plug length.
(c) Evolution of the absolute value of the dimensionless speed of the plug $|\,Ca\,|$.
(d) Evolution of the absolute value of the pressure $|\,\Delta\tilde{P}\,|$.
The critical capillary number and the critical pressure are represented in red on figures (c) and (d) respectively.

plug length and a constant velocity.

Finally, (iii) a *saturated deceleration regime* at low pressure magnitude in which the length of the plug increases but also stabilizes at a saturation value as in (ii). It is interesting to note that only the acceleration regime can be observed in *dry* capillary tubes (see chapter 1) even if the rupture time increases exponentially when the initial size of the plug is increased.

The occurrence of stationary regimes of stabilised plug oscillations is a consequence of the convergence of the critical pressure toward the driving pressure. The difference between the saturation acceleration and deceleration regimes resides in the initial increase or decrease of the critical pressure toward the driving pressure (see Fig. 2.9d). This leads to a saturation plug length smaller (larger) than its initial value for acceleration (deceleration) regimes respectively.

Now that we have identified and characterised the three possible regimes, we will in the two next subsections (i) determine the physical origin and characteristics of the stable states and (ii) study the transition between these regimes and establish a phase diagram.

2.4.2 Stable states

Physical analysis

The divergence of the plug dynamics or its convergence toward a stable periodic state can be understood from the evolution of the plug during the first 3 half periods.

If the magnitude of the pressure is higher than the initial critical pressure, the liquid plug size diminishes through the deposition of a liquid film thicker than the prewetting film. During the second half period, the plug comes back and retraces its steps. The critical pressure is affected by two adversarial effects: the diminution of the plug size and the increase in the prewetting film thickness. The first effect reduces the critical pressure while the second increases its value (see Fig. 2.11). In any case, the critical pressure remains below the driving pressure, and thus the regime remains accelerative. But the difference between the rupture and saturated accelerated regime resides in the subsequent cyclic increase or

decrease of the critical pressure that makes it diverge or converge toward the driving pressure. This tendency is determined through the comparison of the critical pressure at the beginning of the third and second cycles.

If the magnitude of the pressure is lower than the initial critical pressure, only the saturated deceleration regime can occur. Indeed, at each cycle, the plug grows and slows down. Thus, the plug travels on a diminishing portion of the tube and can at best collect the fluid that is lying on this portion of the tube. This bounds the growth of the plug size and explains the observed saturation. We can now work on the determination of the characteristics of the stable periodic states.

Analytical description of the stable periodic states

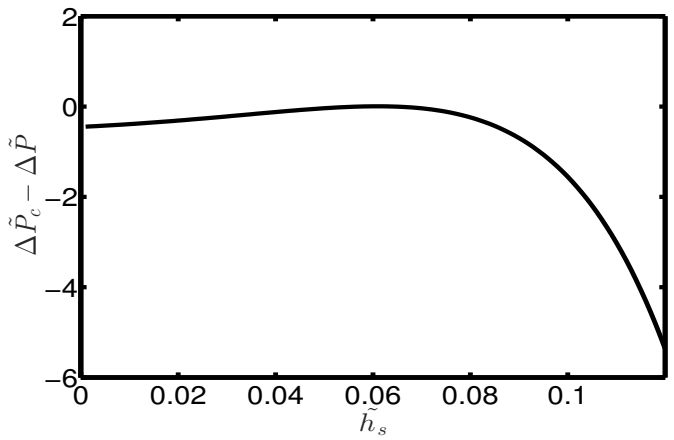

Figure 2.10 – Evolution of the pressure difference between the critical capillary number and the driving pressure in the saturation acceleration regime in which $\Delta\tilde{P}_t = 0.45$, $\tilde{L_0} = 5$, $\tilde{h_0} = 0.04$ and $\tilde{T} = 10^4$.

In the saturated acceleration and deceleration regimes, the plug dynamics evolves toward a stable state, wherein the capillary number Ca and the driving pressure $\Delta\tilde{P}_t$ are equal to their critical values Ca_c and $\Delta\tilde{P}_c$, the plug length to a saturation value $\tilde{L_s}$ and the thickness of the wetting film to a constant value $\tilde{h_s}$. Therefore, equations 2.1 to 2.4 become:

$$\Delta\tilde{P}_t = \Delta\tilde{P}_c \tag{2.6}$$

$$\Delta\tilde{P}_c = 4\tilde{L_s}Ca_c + \left(3.72 + \frac{F^2}{2}\right){Ca_c}^{2/3} \tag{2.7}$$

$$Ca_c = \left(\frac{\tilde{h_s}}{1.34(1-2.5\tilde{h_s})}\right)^{3/2} \tag{2.8}$$

with $F = 3^{1/3}\left(b_0 + b_1 log_{10}(A) + b_2\left[log_{10}(A)\right]^2 + b_3\left[log_{10}(A)\right]^3\right)$ and $A = (3Ca_c)^{-2/3}\tilde{h_s}$

The liquid mass balance between the initial state (wherein the plug size is equal to $\tilde{L_0}$ and the thickness of the liquid film on the walls $\tilde{h_0}$) and the final state (wherein the plug size is equal to $\tilde{L_s}$ and the thickness of the liquid film to $\tilde{h_s}$) gives:

$$\tilde{L_0} + (\tilde{L_d} - \tilde{L_0})(1 - (1-\tilde{h_0})^2) = \tilde{L_s} + (\tilde{L_d} - \tilde{L_s})(1 - (1-\tilde{h_s})^2) \tag{2.9}$$

Finally, there is a relation between the speed of the plug during the motion in a half period and the distance travelled $\tilde{L_d}$:

$$\tilde{L_d} = \int_0^{\tilde{T}/2} Ca_c d\tilde{t} + \tilde{L_s} = \frac{\tilde{T}}{2}Ca_c + \tilde{L_s} \tag{2.10}$$

Using these equations, the pressure difference $\Delta\tilde{P}_t - \Delta\tilde{P}_c$ is plotted against $\tilde{h_s}$ as shown on Fig. 2.10. This graph shows that the equation $\Delta\tilde{P}_t - \Delta\tilde{P}_c = 0$ admits multiple solutions. The stable state corresponding to a given initial state is obtained from a bisection method by looking for the closest solution to the initial state corresponding to an increase or a decrease of the plug length in the acceleration and deceleration regimes respectively. This model allows us to compute the stationary state in the saturation acceleration regime and in the deceleration regime as shown in Fig. 2.9. The saturation values are in good agreement with the values obtained through the computation of the whole plug dynamics.

2.4.3 Diagram of the flow regimes

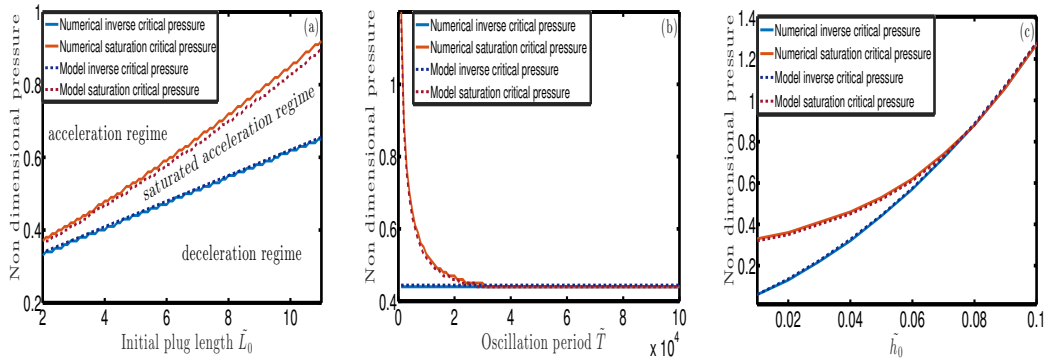

Figure 2.11 – Critical pressure for the transition between the deceleration and saturated acceleration regime (blue line, $\tilde{P} = \tilde{P_{co}}$) and the saturated acceleration regime and the rupture acceleration regime (red line, $\tilde{P} = \tilde{P_{c1}}$) as a function of:
(a) the initial plug lengths $\tilde{L_0}$ with $\tilde{h_0} = 0.05$, $\tilde{T} = 10^4$.
(b) the oscillation periods $\tilde{T}$ with $\tilde{h_0} = 0.05$, $\tilde{L_0} = 5$.
(c) the initial liquid films thickness $\tilde{h_0}$ with $\tilde{L_0} = 5$, $\tilde{T} = 10^4$.

We will now analyse the transition between these 3 regimes for different values of the key parameters governing the evolution of the liquid plug $\Delta\tilde{P_t}$, $\tilde{L_0}$, $\tilde{T}$ and $\tilde{h_0}$.

Following the physical analysis developed in the previous section, we can identify each regime by computing only the first 3 cycles of the plug evolution with the following criteria:

- If $|\tilde{L_p}(\tilde{t} = \tilde{T}) - \tilde{L_p}(\tilde{t} = 2\tilde{T})| < |\tilde{L_p}(\tilde{t} = 2\tilde{T}) - \tilde{L_p}(\tilde{t} = 3\tilde{T})|$, the liquid plug loses more and more liquid at each period. This corresponds to the *acceleration regime* leading to the plug rupture.

- If the previous criterion is not satisfied and $\tilde{L_p}(\tilde{t} = \tilde{T}) < \tilde{L_0}$, the size of the plug cyclically diminishes but this evolution slows down so that it evolves toward a saturation value. This corresponds to the *saturated acceleration regime*.

- Finally the regime wherein the previous criteria are not verified and $\tilde{L_p}(\tilde{t} = \tilde{T}) > \tilde{L_0}$ is the *deceleration regime*.

From numerous numerical simulations, we can then obtain the phase diagrams representing the transition between the three different regimes (see Fig. 2.11, solid lines) as a function of the three key parameters: the initial plug length $\tilde{L_0}$, the oscillation period $\tilde{T}$ and the prewetting film thickness $\tilde{h_0}$.

Another way to compute the transition between the regimes is to use the analytical expressions introduced earlier. Indeed, the occurrence of the acceleration or deceleration regime is only determined by the initial state (since no transition between the acceleration and deceleration regimes occurs). Thus if the value of the pressure magnitude $\Delta\tilde{P_t} > \Delta\tilde{P_{co}}$, the plug accelerates, while if $\Delta\tilde{P_t} < \Delta\tilde{P_{co}}$, it decelerates, with:

$$\Delta\tilde{P_{co}} = 4\tilde{L_0}Ca_{co} + \left(3.72 + \frac{F^2}{2}\right){Ca_{co}}^{2/3} \tag{2.11}$$

$$Ca_{co} = \left(\frac{\tilde{h_0}}{1.34(1 - 2.5\tilde{h_0})}\right)^{3/2} \tag{2.12}$$

with $F = 3^{1/3}\left(b_0 + b_1 log_{10}(A) + b_2\left[log_{10}(A)\right]^2 + b_3\left[log_{10}(A)\right]^3\right)$ and $A = (3Ca_{co})^{-2/3}\tilde{h_0}$.

Then, when $\Delta\tilde{P_t} > \Delta\tilde{P_{co}}$, the saturated acceleration regime occurs if a steady state exists (solution of Eq. 2.6 to 2.10) with $\tilde{L_s} < \tilde{L_0}$, otherwise, the plug breaks. This enables to compute the critical pressure $\Delta\tilde{P_{c1}}$ for the transition between the results obtained with this method are presented on Fig. 2.11 (dashed line, P_{co} in blue and P_{c1} in red) and are in good agreement with the ones obtained from numerical simulations of the plug evolution.

The transitions represented on Fig. 2.11 are rather intuitive since: (i) the critical pressures increase linearly with the plug initial length $\tilde{L_0}$ (see Fig.2.11a) and also increase with the prewetting liquid film thickness (see Fig. 2.11b), (ii) the transition between the acceleration and deceleration regimes does not depend on the period $\tilde{T}$ since it only depends on the initial state and (iii) $P_{co} \rightarrow P_{c1}$ when $\tilde{T}$ increases since, when the time period of the oscillation regime is increased, the forcing tends toward a constant unidirectional pressure driving with no

saturated acceleration regime.The most original result is the disappearance of the *saturated acceleration regime* at large prewetting film thickness as seen on Fig. 2.11c.

2.5 Physiologically relevant driving

We will now study the response of liquid plugs to realistic breathing cycles (see Fig. 2.4, [8]), which are both cyclic and variable in time and thus combine elements from the two previous sections. In particular, we will focus on the critical pressure levels required to trigger the transition between a regime leading to plugs breaking and hence airway reopening, and a regime leading to the persistence of liquid plugs, as a function of the generation inside the airway tree and the thickness of the liquid lining. Indeed, this last parameter strongly varies for patients suffering from pulmonary diseases like cystic fibrosis, chronic obstructive pulmonary disease and asthma and strongly affects the ability of quiet breathing to break liquid plugs as we shall see in the remaining part of this section.

2.5.1 Parameters value

The key parameters to run the simulations are: the shape of the pressure driving, the geometry of the lung (radius of the airways at each generation), the initial sizes of the plug $\tilde{L_0}$, the relative initial thickness of the mucus lining $\tilde{h_0}$ and the properties of mucus. For the lung geometry, we will only consider here the intermediate conducting airways (generation 10 to 16), where the Reynolds, Weber, Bond and Capillary numbers are small and use the data presented in Table 1 to estimate the airway radii. Since mucus plugs in the lung originate from Rayleigh-Plateau instability, we will consider that their length is dictated by the most unstable wavelength $\lambda = 2\pi\sqrt{2}R$. Thus the initial dimensionless length of the plug can be estimated as $\tilde{L_0} = 2\sqrt{2}(1-(1-\tilde{h_0})^2)$. For the thickness of the mucus lining, we will consider thicknesses of healthy patients ($2-3\%$ of the airways radii) up to thicknesses associated with pulmonary diseases (10% of the airways radii or more). Finally for the mucus properties, we will consider

the values provided in the introduction.

2.5.2 Flow regimes of liquid plugs under a realistic breathing cycle

For realistic pressure driving, only two flow regimes are observed : (i) a *acceleration regime* leading to the plug rupture (see Fig. 2.12a) and (ii) a *deceleration regime* leading to stable periodic oscillations of the liquid plug (see Fig. 2.12b). While we do not have quantitative explanation for the absence of the saturated acceleration regime, it can be explained qualitatively by the fact that this regime occurs for rectangular pressure driving when the pressure magnitude is just above the critical pressure P_{co}. Thus, for physiologically relevant pressure driving, if the pressure magnitude is just above the critical pressure P_{co}, the dynamics of the plug will be mostly decelerative due to the progressive increase in the pressure during the cycle and thus this will lead instead to a deceleration regime.

2.5.3 Critical pressure in the airway tree

Now, we can study the critical pressure magnitude required to open obstructed airways with realistic pressure driving as a function of the liquid lining thickness and the generation in the lung (see Fig. 2.13). These critical pressures are compared to the values obtained for constant pressure driving. As expected, the critical pressures are higher in the former case since for time dependent signal, the plug always grows during the first part of each half-cycle (since the driving pressure is low), which makes the rupture of the plug more difficult.

This figure shows that the thickness of the liquid lining is a key parameter, which dramatically increases the critical pressure necessary to break liquid plugs. If we compare the calculated critical pressure to the typical breathing pressure magnitude (between 133 and 266 Pa), we see that liquid plugs rupture naturally during quiet breathing cycles of healthy patients for all generations while they persist in airways of sick patients, especially in the last generation of the lung.

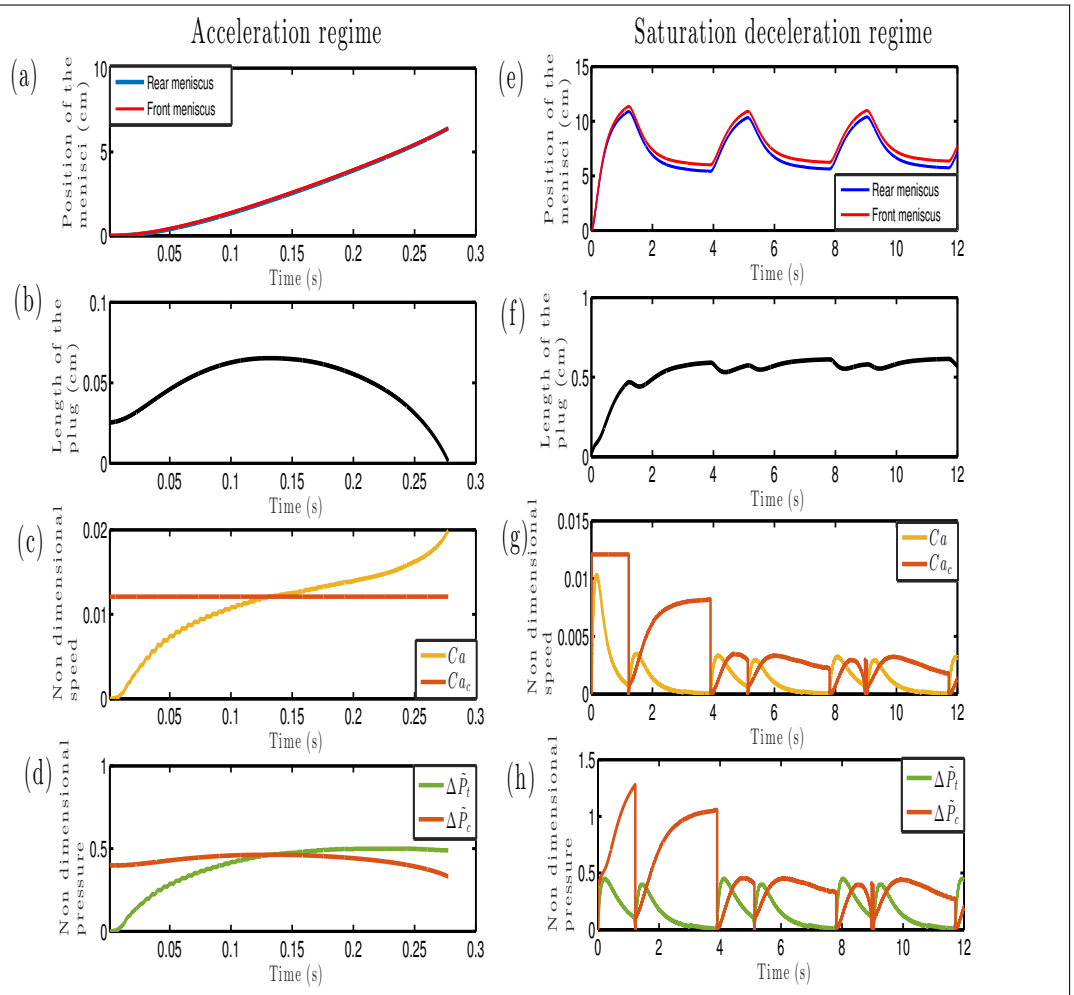

Figure 2.12 – Temporal evolution of the dynamics of a liquid plug of initial length $\tilde{L_0} = 2\sqrt{2}(1-(1-\tilde{h_0})^2)$ in a capillary tube prewetted by a liquid film of thickness $\tilde{h_0} = 0.06$ under the driving pressure $\Delta\tilde{P_t} = 0.5$ in the acceleration regime and $\Delta\tilde{P_t} = 0.45$ in the saturation deceleration regime:
(a-e) Position of the menisci.
(b-f) Evolution of the length of the plug.
(c-g) Evolution of the absolute value of the dimensionless speed of the plug $|\,Ca\,|$.
(d-h) Evolution of the absolute value of the pressure $|\,\tilde{\Delta P}\,|$.
The critical capillary number and the critical pressure are respectively in red and green.

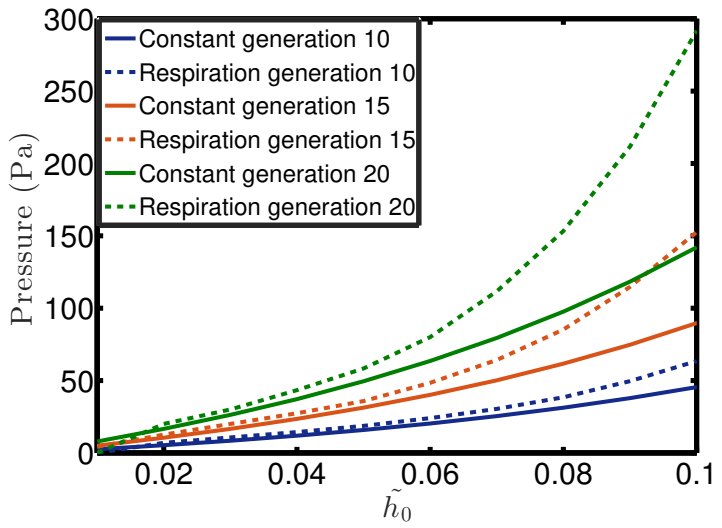

Figure 2.13 – Critical pressure for the transition between the acceleration and deceleration regime as a function of the liquid films thickness $\tilde{h_0}$ and for different generation of the lung tree. Solid line: constant pressure driving. Dashed line: realistic pressure driving of same magnitude.

2.6 Conclusion: critical assessment of the relevance of this study for pulmonary airway conditions

In this study, we did not consider some important factors that might play a fundamental role on obstructed lung airways reopening : (i) the complex rheological properties of the mucus evolving with the pathologies, (ii) the deformation of the airways walls and its effect on the plug displacement and rupture, (iii) the complex 3D branching geometry of the lung. Moreover, the alveolar pressure is also directly applied to the liquid plug, neglecting the interactions at the ends of the bronchi or the pressure changes in the presence of obstructed pathways. Nevertheless, this study is, to the best of our knowledge, the first to explore the dynamics and rupture of liquid plugs for realistic breathing cycles and prewetted airways and to determine the critical pressure necessary to reopen obstructed airways in these conditions. The results are consistent with observations in real lungs: occlusion mainly occurs in the smallest conducting airways and diseases

increasing the thickness of airways lining strongly increase the persistence of liquid plug in the bronchial tree. Finally, our model enables the gradual incorporation of the missing ingredients to provide more and more consistent models of plugs flow in the lung airway and achieve realistic predictions.

Chapter 3

Pressure-driven dynamics of liquid plugs in a rectangular microchannel: influence of the transition between static and dynamic film deposition regimes

Abstract

In this chapter, we study experimentally and theoretically the dynamics of liquid plugs in rectangular microchannels for both unidirectional and cyclic pressure forcing. In both cases, it is shown that the transition between static and dynamic film deposition behind the liquid plug leads to a dramatic acceleration of the plug, rapidly leading to its rupture. This behavior proper to polygonal channels with singularities in the tube corners is recovered from a reduced dimension model based on previous theoretical and numerical developments. In addition, it is shown for cyclic periodic forcing that the plug undergoes stables periodic oscillations if it remains in the static deposition regime during the first cycle, while otherwise it accelerates cyclically and ruptures. The transition between these two regimes occurs at a pressure-dependent critical initial length.

3.1 Introduction

The interest in segmented gas-liquid flows in polygonal, and in particular, rectangular microchannels [156, 157, 145, 139, 158, 159, 160, 161, 162, 163] has further grown with the development of soft lithography techniques in microfluidics [164, 165], which enable simple design of complex microchannels with rectangular cross-sections [166].

A finite volume of liquid (liquid plug or slug) that is displaced by an air finger at constant flow rate or pressure head (Taylor flow) leaves on the walls a trailing liquid film. Its thickness can be quantified by the so-called wet fraction, which is the proportion of the tube section occupied by the liquid film. *In cylindrical capillary tubes*, this parameter increases monotonically with the dimensionless velocity of the meniscus (the so-called capillary number Ca) with a $Ca^{2/3}$ law [111] at low capillary number. This law was further extended to larger capillary number [133]. In *polygonal microchannels* however, a transition occurs at a critical capillary number between two radically different regimes: Under this critical parameter, the fluid deposition process is mainly independent of the capillary number since it relies on the static shape of the meniscus [138, 139]. Indeed, the static meniscus shape cannot follow the singular shape of the rectangular channel, thus leading to fluid deposition in the corner of the tube. Above this critical number, the fluid deposition resulting from the deformation of the rear meniscus induced by the flow overcomes the static one. In this case, the wet fraction becomes again dependent on the capillary number, similarly to what is observed in cylindrical channels. Nevertheless, this process in polygonal channels also depends on the tube geometry [157, 138, 139, 160, 161]. It is possible to extend the laws introduced for cylindrical tubes to rectangular tubes, providing the introduction of an aspect-ratio-dependent capillary number [160, 161].

This liquid film deposition process induces a dramatic acceleration of a liquid plug when it is pushed at constant pressure head [96]. Indeed the diminution of the plug size leads to a reduction of the viscous resistance of the plug to motion, itself leading to an acceleration of the plug and thus more fluid deposition. More recently, it has been shown experimentally [97] that the inverse behavior

(progressive slow down and growth of the liquid plug) might also be observed in prewetted capillary tubes depending on the value of the driving pressure and the thickness of the prewetting film. The acceleration and rupture of a liquid plug has also been evidenced in complex tree geometries [96] and for cyclic pressure forcing [167]. In the latter case however, both the diminution of the viscous resistance and interfacial resistance (due to lubrication effects) at each cycle contribute to the plug acceleration and breaking.

Nevertheless, all the aforementioned studies were conducted in cylindrical tubes or at capillary number well above the critical capillary number. In this chapter, we study experimentally and theoretically the influence of the transition between static and dynamics fluid deposition process on the dynamics of liquid plugs in rectangular channels pushed either with a unidirectional or a cyclic pressure forcing. In both cases, it is shown that the transition between these two regimes leads to a dramatic acceleration of the plug eventually leading to its rupture. It is interesting to note that such rapid switching between two dramatically different behaviors has been reported for propagating bubbles by De Lózar & al. [168]. For cyclic forcing, it is shown that under a critical length the plug dynamics is unstable and leads to the plug rupture while above it is stable and periodic; the experimental results are recovered from a reduced dimension model, inspired from previous theoretical developments [96, 97, 167] adapted here to take into account (i) the modifications of the laws in the rectangular geometry, (ii) lubrication effects resulting from the back and forth motion of the liquid plug on a prewetted tube, and (iii) the transition between static and dynamic film deposition. The second and third sections provide the experimental and model details. The fourth and fifth sections explore respectively the response of liquid plugs to unidirectional and periodic cyclic pressure forcings and compare the observed dynamics to results in cylindrical tubes.

3.2 Experimental method

The experimental set-up is represented on Fig. 3.1. The experiments are conducted in rectangular polydimethylsiloxane (PDMS) microfluidic channels ob-

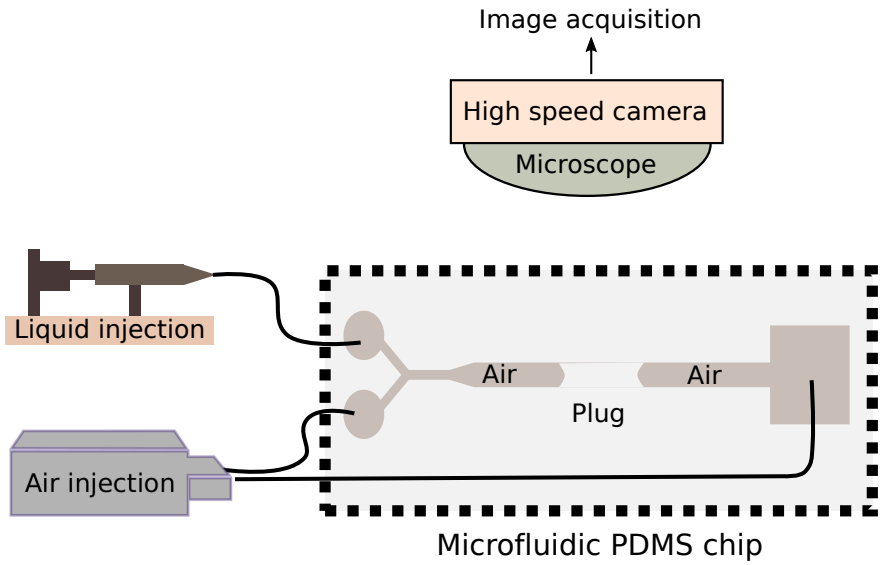

Figure 3.1 – Sketch of the experimental setup. A liquid plug is created inside a rectangular PDMS channel by pushing alternatively some liquid and some air at a Y-junction. The liquid is pushed by a syringe pump while the air is pushed by a MFCS pressure controller. Then the liquid plug is moved by the pressure controller either in one direction (unidirectional driving) or alternatively in both directions (cyclic periodic driving).

tained by standard photolithography techniques: A mold is etched by depositing a layer of photoresist resin (Microchem, SU8-2035) on a silicon wafer. This layer is spin-coated and patterned by standard photolithography. The spin-coating speed combined with the choice of the photoresist sets the height $h = 45 \pm 2\mu m$ of the microfluidic channels, while the width $w = 785 \pm 2\mu m$ is controlled by the design of the patterned masks which are used during the UV exposure. These values of the channel size and height were measured afterward (see Fig. 3.2). After exposure, the film is developed in an organic solvent solution (SU-8 developer) to yield the negative of the channel design. This SU8 mold was used to pour PDMS (Dow Corming, Sylgard 184) whose polymerization was obtained by curing it at 100°C. The microfluidic channel is then cut out and bonded on a glass microscope slide by passing the two surfaces in an oxygen plasma. The microscope slides are covered by a thin PDMS membrane in order to guarantee identical boundary condition to all four channel walls .

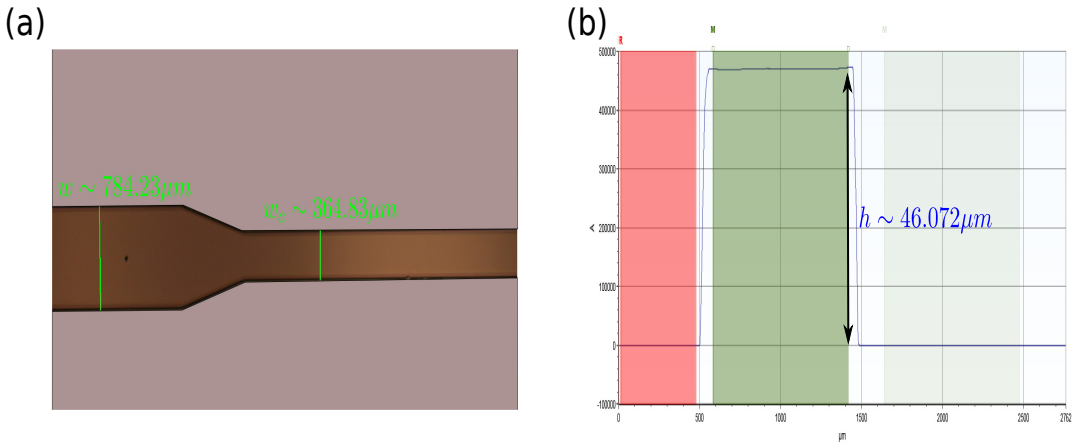

Figure 3.2 – Geometry dimensions of the rectangular microchannel:
(a) Widths of the controlled region w_c and the experiment region w measured with a microscope.
(b) Height of the microchannel measured with a profilometer (Dektak XTL).

Then, perfluorodecalin (PFD) liquid plugs are created in this channel by pushing alternatively some liquid and some air at a Y-junction with a syringe pump and a MFCS Fluigent pressure controller respectively, connected to both entrances of the microfluidic device. Perfluorodecalin was used for its good wetting properties (static contact angle $\theta_s = 23 \pm 1°$ see Fig. 3.3) with PDMS and since it does not swell PDMS [169]. Then, air is blown in the channel at low pressure to bring the liquid plug to the center of the microfluidic channel and stopped manually when the target position is reached. Finally, the plug motion is forced with either a *unidirectional* or *cyclic* periodic pressure forcing with the MFCS programmable pressure controller. For cyclic forcing one entrance and the exit of the channel are connected to two channels of the MFCS pressure controller. Then an overpressure (compared to atmospheric pressure) is applied alternatively to each end of the channel while the other is set to atmospheric pressure. The resulting shapes of the pressure forcing measured with an internal pressure sensors in these two cases are represented (as in chapter 1) on Fig. 3.4. For cyclic forcing the period was fixed to $2T = 4s$ or $2T = 6s$, with T the duration of a half cycle. The measured unidirectional pressure driving can be approximated by the following analytical expression based on Gompertz

functions:

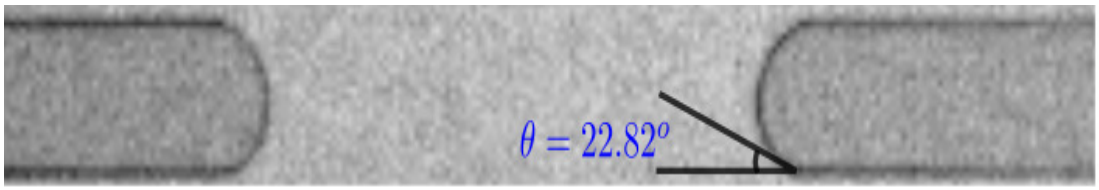

Figure 3.3 – Contact angle of a perfluorodecalin liquid plug in the PDMS microchannel

$$P_t = 900e^{-3e^{-10t}}, \tag{3.1}$$

while the cyclic forcing can be approximated by the expression :

$$\Delta P_t = 1200e^{-6e^{-3t}}\text{Pa} \quad \text{for } t \in [0;T] \tag{3.2}$$

$$\Delta P_t = (-1)^n(P_c - P_d) \text{ for } t \in [nT;(n+1)T] \tag{3.3}$$

$$\text{with } P_c = 1200e^{-2.5e^{-3(t-nT)}}Pa \tag{3.4}$$

$$\text{and } P_d = 1200e^{-1.2(t-nT)}e^{-0.02e^{-1.2(t-nT)}}Pa \tag{3.5}$$

Initially the tube is dry. Hence, the liquid plug moves on a dry capillary tube for unidirectional forcing. Nevertheless, the motion of the liquid plug leaves a trailing liquid film on the walls and in the corner of the channel. Thus, for cyclic forcing the liquid plug moves on a prewetted capillary tube after the first cycle as long as it is moves on a portion of the tube already visited by the liquid plug in the previous back and forth motions.

Experiments are recorded with a Photron SA3 high speed camera mounted on a Z16 Leica Microscope. The resolution of the camera used in the experiments is 1024×64 pixels, the acquisition frame rate 125 images/s and the trigger time 1/3000 s. The image analysis is then performed using ImageJ software and Matlab. The plug evolution is characterized by monitoring the positions of the rear interface X_r and front interface X_f (see Fig. 3.1), and deducing the evolution of the plug length $L_p(t) = X_f(t) - X_r(t)$ and the speed of the rear interface of the

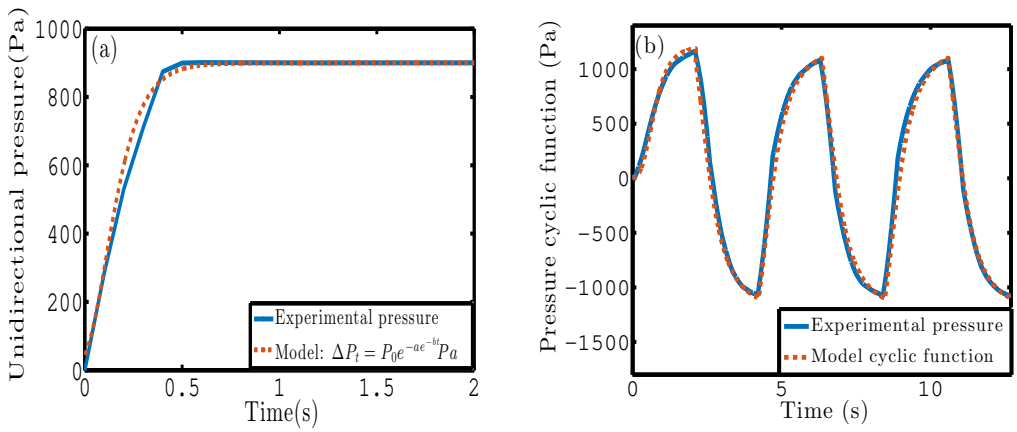

Figure 3.4 – Pressure forcings:
(a) Unidirectional pressure forcing measured experimentally (blue solid line) and approximated by the formula (red dotted line): $\Delta P_t = P_0 e^{-ae^{-bt}}$ with $P_0 = 900Pa$, $a = 3$ and the growth rate $b = 10$.
(b) Cyclic pressure forcing imposed by the MFCS pressure controller measured experimentally (blue solid line) and approximated by the analytical formula $\Delta P_t = 1200e^{-6e^{-3t}} Pa$ for $t \in [0;T]$, and $\Delta P_t = (-1)^n (P_c - P_d)$ for $t \in [nT;(n+1)T]$ with $P_c = 1200e^{-2.5e^{-3(t-nT)}} Pa$ and $P_d = 1200e^{-1.2(t-nT)} e^{-0.02e^{-1.2(t-nT)}} Pa$ (red dotted line) and $T = 2.12$ is the half period.

plug $U_r = dX_r/dt$.

3.3 Model of a plug flow in dry and prewetted rectangular microfluidic channels

The model derived in this section combines previous theoretical developments [96], [97] and [167], and integrates additional elements to include the transition between static and dynamic liquid film deposition.

3.3.1 Dimensional analysis and characterisation of the regime

In this problem, we consider a single liquid plugs of initial length L_0 set into motion in a rectangular microfluidic channel under the unidirectional or periodic

forcings represented on Fig. 3.4.

Dimensionless number	Formula	Estimation
τ_c/τ_{exp}	l_c/U	1.8×10^{-2}
τ_d/τ_{exp}	$\rho {l_c}^2/\mu$	1.3×10^{-2}
Re	τ_d/τ_c	0.7
We	$\rho U^2 l_c/\sigma$	1.9×10^{-3}
Ca	$\mu U/\sigma$	2.6×10^{-3}
Bo	$\rho g h^2/\sigma$	2×10^{-3}

Table 3.1 – Values of the key dimensionless parameters associated with the mean characteristic velocity $U = 1 cm/s$.

The characteristic parameters in this problem are the width of the microfluidic channel w, its height h, the viscosity of the liquid plug μ, the surface tension σ, the speed of the liquid plug U and the characteristic time associated with the plug evolution in the experiments τ_{exp}. For cyclic forcing, this time is simply the half period of the signal $\tau_{exp} = T$, while for unidirectional forcing, it is the time required for the plug to rupture. In the following, the geometry will be characterized by the aspect ratio $\alpha = w/h$ and the characteristic length scale $l_c = \sqrt{wh}$. From these parameters, we can construct the characteristic convection time $\tau_c = l_c/U$, and the characteristic viscous diffusion time $\tau_d = \rho {l_c}^2/\mu$. Then we can characterise the flow regime by introducing the following dimensionless numbers: the Reynolds number ($Re = \tau_d/\tau_c$) which compares convection to viscous diffusion, the Weber number ($We = \rho U^2 l_c/\sigma$) which compares inertia to surface tension, the capillary number ($Ca = \mu U/\sigma$) which compares viscous effects to surface tension effects, the Bond number which compare gravity to surface tension ($Bo = \rho g h^2/\sigma$), and finally the ratio of the experimental characteristic time τ_{exp} to the convective and diffusion times τ_{exp}/τ_c and τ_{exp}/τ_d. In the experiments the average velocity is typically $U_{mean} = 1$ cm/s and the maximal velocity $U_{max} = 4.5$ cm/s. The time required for the plug to rupture varies between 0.5 s and 5 s for unidirectional forcing and the half period of periodic forcing is $T = 2$ s or $T = 3$ s. These values enable the estimation of the dimensionless numbers introduced previously and summarised in 3.1 (for these estimations, we take $\tau_{exp} = 1$ s and $U = 1$ cm/s).

These values of the dimensionless numbers indicate that, globally, surface tension effects are dominant over viscous effects, themselves being dominant over inertial effects. This means that away from the walls, the shape of the meniscus is mainly dictated by the minimization of the interfacial capillary energy. This undeformed part of the meniscus is called the static meniscus. Nevertheless, as demonstrated first by Bretherton [111] in cylindrical tubes, viscous effects still play an important role close to the walls due to the incompatibility between the adherence condition (null velocity at the walls) and the homogeneous motion of an undeformed meniscus. This singularity leads to the existence of large shear stresses close to the walls and, hence, the deposition of a thin trailing film behind the rear meniscus and a change in the apparent contact angle for the front meniscus. Thus viscous effects still play an important role close to the walls despite the low value of the capillary number. Then, the relative importance of unsteady effects can be estimated from the ratios τ_c/τ_{exp} and τ_d/τ_{exp}. Since, these two ratios are small, the unsteady terms can be neglected in Navier-Stokes equations even if the plug evolves over time: the flow is quasi-static. Finally, the small value of the Bond number indicates that gravity effects can be neglected. Based on this analysis, we expect the liquid plugs dynamics in the present problem to be considered as a quasi-static visco-capillary flow governed by steady Stokes equation (as in chapter 1).

3.3.2 Model of the plug dynamics.

The model describing the pressure drop in the microfluidic channel is obtained by equalizing the driving pressure head ΔP_t (Fig. 3.4) to the sum of the pressure drop resulting from viscous dissipation in the bulk of the liquid plug ΔP_{visc}^{bulk}, the pressure drops at the front and rear meniscus of the plug ΔP_{front}^{men}, ΔP_{rear}^{men} and the pressure drop ΔP_{bubble} inside the air. Simple estimation of these pressure drops show that this latest contribution can of course be ignored compared to the other ones (see e.g. Kreutzer & al. [153]). Thus, the steady state balance of pressure across the liquid plug becomes:

$$\Delta P_t = \Delta P_{visc}^{bulk} + \Delta P_{front}^{men} + \Delta P_{rear}^{men} \tag{3.6}$$

Viscous pressure drop

The pressure drop resulting from a laminar flow of a fluid in a rectangular geometry is given by White [170]:

$$\Delta P_{visc}^{bulk} = \frac{a\mu QL}{wh^3} \tag{3.7}$$

with $a = 12\left[1 - \frac{192}{\pi^5\alpha}\tanh\left(\frac{\pi\alpha}{2}\right)^{-1}\right]$, L the portion of the tube considered and Q the flow rate. In the limit $\alpha \gg 1$ considered here ($\alpha = 17.5$ in the experiments) and for a liquid plug of length L_p, this expression becomes:

$$\Delta P_{visc}^{bulk} = \frac{12\mu QL_p}{wh^3} \tag{3.8}$$

where $Q = U_r S_r$ is the flow rate, S_r is the the cross sectional area open to air behind the liquid plug and U_r the speed of the rear meniscus. This expression relies on two assumptions: (i) it assumes that the pressure drop inside the plug follows a Hagen-Poiseuille law despite the finite size of the plug and the recirculation occurring close to the menisci and (ii) it assumes the same speed for the front and rear menisci. The validity of the first approximation has been tested numerically with the OpenFoam Volume of Fluid code [167] in 2D. These 2D simulations shows that equation (3.8) is an excellent approximation of the viscous pressure drop (error < 4.5%) as long as the length of the plug remains larger than the height of the channel. For smaller plugs the discrepancy increases progressively but, in this case, the pressure drops at the menisci strongly dominate over bulk viscous pressure drop leading to minor effects of the error on the overall plug dynamics. The second approximation amounts to neglect the evolution speed of the plug length dL_p/dt compared to the translational speed of rear interface dX_r/dt, since $dX_f/dt = dX_r/dt + dL_p/dt$. Experimental measurements of the speed of the front and rear interfaces show that this approximation holds within a few percent of accuracy. In the remaining part of the thesis, we will therefore neglect the difference between the front and rear interfaces in the estimation of the pressure drops, and the capillary number Ca will therefore be constructed

on the rear interface velocity: $Ca = \mu U_r/\sigma$.

Front meniscus pressure drop

When a liquid plug is at rest (no pressure head) in a rectangular tube, its front and rear interfaces adopt complex shapes minimizing the interfacial energy. This minimization problem can be solved with the method of Lagrange multipliers. The solution is a constant mean curvature (CMC) surface verifying the wetting conditions at the walls. In a rectangular geometry, this shape is rather complex Wong & al. [171] and there is no analytical expression of these surfaces geometry. Nevertheless, what matters when we consider the motion of a liquid plug is not the static shape of the meniscus but the departure from this static shape when the plug moves. Indeed the Laplace pressure jumps resulting from the curvatures of the front and rear interface at rest compensate one another leading to a zero contribution. Therefore we will only consider in the following the dynamic pressure jumps at the interface, that is to say the Young-Laplace pressure jumps when the plug is moving minus their value at rest.

The computation of the dynamic pressure jumps at the front interface can be greatly simplified in a rectangular geometry with high aspect ratio $\alpha \gg 1$. In this case, the principal curvature in one direction $\kappa_h \approx 2\cos(\theta_d^a)/h$ is strongly dominant over the curvature in the other direction $\kappa_w \approx 2\cos(\theta_d^a)/w$, where θ_d^a is the advancing dynamic apparent contact angle. Based on Young-Laplace equation, the dynamic pressure jump at the front meniscus can thus be estimated from the formula:

$$\Delta P_{front}^{men} \approx -\sigma(\kappa_h - \kappa_h^s), \text{ with } \kappa_h \approx 2\cos(\theta_d^a)/h \tag{3.9}$$

and $\kappa_h^s \approx 2/h$ the principal curvature in the vertical direction at rest. In the limit of low capillary numbers, asymptotic expansion leads to: $cos\theta_d^a \sim (1 - {\theta_d^a}^2/2)$, and the dynamic pressure drop becomes:

$$\Delta P_{front}^{men} = \frac{2\sigma}{h}\left(\frac{{\theta_d^a}^2}{2}\right) \tag{3.10}$$

Of course, this expression is an approximation since (i) it neglects the horizontal curvature compared to the vertical one and (ii) it neglects the thickness of the prewetting film (if the plug is moving on a prewetted capillary tube). This expression is therefore only valid for high aspects ratios h/w, low capillary numbers and thin prewetting films.

The next step is to determine the value of the dynamic apparent contact angle θ_d^a as a function of the capillary number. *On a dry substrate*, the dynamic contact angle can be estimated from Hoffman-Tanner's law:

$$\theta_d^a = ECa^{1/3} \tag{3.11}$$

The measurements of the coefficient E for wetting silicon oil liquid plugs by Bico and Quéré [155] and perfluorodecalin liquid plugs by Signe & al. [167] in cylindrical glass capillary tubes obtained consistent values of this parameter: $E = 4.3$ and $E = 4.4$ respectively. Ody & al. [172] and Baudoin & al. [96] measured a value of $E = 4.9$ for perfluorodecalin liquid plug moving in PDMS rectangular capillary tubes with high aspect ratio. This value is in good agreement with the experiments performed in our rectangular microchannels.

The expression of the dynamic contact angle in the rectangular microchannel *on a prewetted surface* that integrates lubrication effects is the theoretical expression proposed by Chebbi [137] and used in chapter1:

$$tan\theta_d^a = (3Ca)^{1/3} f((3Ca)^{-2/3} cos\theta_d^a \, h_f/R) \tag{3.12}$$

with h_f/R the thickness of the liquid film ahead of the liquid plug, $f(y) = \sum_{j=0}^{3} b_n [log_{10} y]^n$ and the coefficients b_n are tabulated in Chebbi [137]. To the best of our knowledge, no rigorous derivation of an analytical formula exists for rectangular geometries. Nevertheless, a similar expression as equation (3.12) is expected in rectangular geometries with high aspect ratios $\alpha \gg 1$. Indeed, Chebbi (similarly to Bretherton) derive the above theoretical expression in the approximation of thin prewetting liquid film h_f compared to the radius of the tube ($h_f/R \ll 1$). In this approximation, the radial curvature of the tube is locally neglected and the problem solved is identical to a 2D planar problem.

In the rectangular configuration, an estimation of the thickness of the prewetting film in the vertical direction is nevertheless missing. To adapt this formula to rectangular geometries, Baudoin & al. [96] proposed to estimate the relative thickness of the prewetting film by the formula $\sqrt{1-\tilde{S}_f}$ with $\tilde{S}_f = S_f/(hw)$ the dimensionless cross sectional area open to air in front of the plug. For rectangular channel with large aspect ratios, it is expected that this expression slightly overestimates lubrication effects since the prewetting film is always thicker on the lateral walls than in the central ones.

Finally, as demonstrated by Signe & al. [167], a good approximation of the implicit formula (3.12) in the limit of low capillary numbers is:

$$\theta_d^a = FCa^{-1/3} \tag{3.13}$$

with:
$F = 3^{1/3}\left(b_0+b_1 log_{10}(A)+b_2\left[log_{10}(A)\right]^2+b_3\left[log_{10}(A)\right]^3\right)$ and $A = (3Ca)^{-2/3}\sqrt{1-\tilde{S}_f}$.
This expression shares some similarities with Hoffman-Tanner's law but this time the coefficient F depends on the capillary number, underlining the lubrication effect.

Rear meniscus pressure drop

The dynamical pressure drop at the rear interface was calculated theoretically by Bretherton [111] in cylindrical geometries, Wong & al. [138, 139] for polygonal channels, and later on numerically by Hazel & Heil [140] for rectangular microfluidic channels of different aspect ratios at finite capillary numbers. Based on the results of Hazel & Heil [140], it is possible to infer the following formula for the dynamic pressure jump at the rear interface [96]:

$$\Delta P_{rear}^{men} = \frac{2\sigma}{h} D f(\alpha) Ca^{2/3} \tag{3.14}$$

with $f(\alpha) = (0.52 + 0.48/\alpha)$ and $D = 4.1$ a constant obtained from best fitting of Hazel & Heil [140] data.

Total pressure drop

If we combine equations (3.8), (3.10), (3.11), (3.13) and (3.14), the total pressure drop across the liquid plug becomes:

$$\begin{aligned} \text{Dry tube: } \Delta P_t &= \frac{12\sigma S_r L_p}{wh^3} Ca + \frac{\sigma}{h}\left[E^2 + 2Df(\alpha)\right] Ca^{2/3} \\ \text{Wet tube: } \Delta P_t &= \frac{12\sigma S_r L_p}{wh^3} Ca + \frac{\sigma}{h}\left[F^2 + 2Df(\alpha)\right] Ca^{2/3} \end{aligned} \tag{3.15}$$

with $E = 4.9$, $F = 3^{1/3}\left(b_0 + b_1 log_{10}(A) + b_2\left[log_{10}(A)\right]^2 + b_3\left[log_{10}(A)\right]^3\right)$ and $A = (3Ca)^{-2/3}\sqrt{1-\tilde{S}_f}$. These equations can be written under dimensionless form by introducing the characteristic length $l_c = \sqrt{wh}$ and the characteristic pressure variation σ/h:

$$\begin{aligned} \text{Dry tube: } \Delta\tilde{P}_t &= 12\sqrt{\alpha}\tilde{S}_r\tilde{L}_p Ca + \left[E^2 + 2Df(\alpha)\right] Ca^{2/3} \\ \text{Wet tube: } \Delta\tilde{P}_t &= 12\sqrt{\alpha}\tilde{S}_r\tilde{L}_p Ca + \left[F^2 + 2Df(\alpha)\right] Ca^{2/3} \end{aligned} \tag{3.16}$$

where the tildes indicate dimensionless functions. To achieve a close set of equations, two equations are missing: one determining the evolution of the plug length $\tilde{L}_p$ and one determining the fluid deposition process on the walls and consequently $\tilde{S}_r$ and $\tilde{S}_f$.

Evolution of the plug length

The first equation is simply obtained from a mass balance between the amount of liquid that the plug collects and loses. Let $S_0 = wh$ be the cross section of channel, and S_r and S_f the sections of the tube open to air behind and in front of the plug respectively. The mass balance becomes:

$$S_0 dL_p = (S_0 - S_f)dx_f - (S_0 - S_r)dx_r \tag{3.17}$$

with $dx_f = dL_p + dx_r$. Therefore, the equation giving the evolution of the length of the liquid plug takes the form:

$$\frac{dL_p}{dt} = \left[\frac{S_r}{S_f} - 1\right] U = \frac{\sigma}{\mu}\left[\frac{S_r}{S_f} - 1\right] Ca \tag{3.18}$$

where S_r depends only on the dimensionless speed of the rear interface $S_r = S_r(Ca)$ and S_f depends on the history of the liquid deposition on the walls and the position of the front interface $S_f = S_f(x_f, t)$. If we introduce the characteristic length l_c and the viscocapillary time scale $\tau = \mu l_c/\sigma$, we obtain the dimensionless equation:

$$\frac{d\tilde{L}_p}{d\tilde{t}} = \left[\frac{\tilde{S}_r(Ca)}{\tilde{S}_f(\tilde{x}_r, \tilde{t})} - 1\right] Ca \tag{3.19}$$

When the plug moves on a dry surface, then $\tilde{S}_f = 1$. Otherwise the value of $\tilde{S}_f$ is either inferred from the initial condition if the plug moves on a prewetted tube or from a memory of the liquid deposition by the liquid plug when the plug undergoes cyclic motion (see Signe & al. [167] for cylindrical tubes). In many publications, the wet fraction m is introduced instead of the air fraction S_r. The wet fraction is the relative portion of the tube section occupied by the liquid. These two parameters are linked by the formula: $m = 1 - \tilde{S}_r$.

Static and dynamic wet fraction

Figure 3.5 – Sketch of the cross-section behind the liquid plug:
(a) When $Ca \to 0$ (static film deposition regime).
(b) $Ca \gtrsim Ca_c$ (dynamic film deposition regime). Black: liquid, white: air.

An air finger pushing a liquid plug in a cylindrical tube adopts a cylindrical shape closely fitting the shape of the cylindrical tube. Such close fitting is not

possible in rectangular tubes due to the presence of the singularities in the corners. In the low Bond number ($Bo \ll 1$) and low capillary number limit ($Ca \ll 1$), the section of the bubble far behind the rear meniscus can adopt two configurations [161] schematically represented on Fig. 3.5 depending on the value of the capillary number:

- (i) When $Ca \to 0$, in the static limit, the liquid only covers the corners of the tube and the limit between the liquid and the air are four quarter circles. In this case the wet fraction tends to an asymptotic value called the static wet fraction m_s, which depends only on the aspect ratio of the channel α: $m_s = m_s(\alpha)$. Indeed, the liquid deposition in the corners of the tube in this regime relies on the static shape of the rear meniscus.

- (ii) when $Ca \gtrsim Ca_c$, the limit between the liquid and the air becomes two half circle on the side and a liquid film covers the walls in the center of the channel De Lozàr & al. [161]. In this case, the wet fraction depends on the dynamics of the plug and hence on the capillary number. We will call it the dynamic wet fraction $m_d = m_d(Ca, \alpha)$.

The transition between these two configurations is progressive (see De Lozàr & al. [160]) and occurs at a critical capillary number Ca_c whose value was found in our experiments to lie around $Ca_c = (2 \pm 0.1) \times 10^{-3}$, a value coherent with the measurement of De Lozàr & al. [161] at similar aspect ratios α.

The *static wet fraction* m_s in the absence of gravity ($Bo = 0$) was theoretically predicted in Wong & al. [138]:

$$m_s = (4 - \pi)\tilde{r_s}^2 \tag{3.20}$$

with $\tilde{r_s} = r_s/l_c$ the dimensionless radius of curvature of the four quarter circles delimiting the liquid and the air in the corners of the tube and

$$\tilde{r_s} = \frac{\sqrt{\alpha}}{\alpha + 1 + ((\alpha - 1)^2 + \pi\alpha)^{1/2}} \tag{3.21}$$

For an aspect ratio $\alpha = 17$ such as in our experiments, this formula gives the value $m_s = 0.012$. The wet fraction can be estimated experimentally by moni-

toring the evolution of the plug size as a function of the rear interface velocity when $Ca \ll Ca_c$. We found the average estimate of this parameter (over all the experiments performed and described in the next section) to be: $m_s = 0.03$. This value is larger than the theoretical value predicted by Wong & al. [138]. Nevertheless the theoretical value derived by this author was obtained with zero influence of gravity ($Bo = 0$). For finite values of the Bond number, it was shown experimentally by De Lozàr & al. [161] (see their figure 4) that gravity tends to significantly increase the static wet fraction (these authors found $m_s \approx 0.065$ for $Bo \sim 1$ and $\alpha = 15$). In our case, though small the Bond number (table 3.1) is not null, which might explain the larger value of the static wet fraction measure experimentally than expected theoretically. For the simulations, we will therefore adopt the constant value:

$$m_s = 1 - \tilde{S_r} = 0.03 \text{ for } Ca < Ca_c \tag{3.22}$$

under the critical capillary number.

The evolution of the *dynamic wet fraction* in square and rectangular microfluidic channels was investigated experimentally by [158, 159, 160, 146, 162, 163] and numerically by [140, 161, 173]. In particular, [160, 161] found that the measured and simulated evolution of the dynamic wet fraction m_d as a function of the capillary number collapse for all aspect ratio α providing the introduction of an effective capillary number $\hat{Ca} = \left[1 + \alpha^2/\alpha_t^2\right] Ca$ with $\alpha_t = 6.4$. Thus the behavior in a rectangular channel with any aspect ratio can be inferred from the behavior in a square tube. This scaling subsist even for finite Bond numbers as demonstrated both theoretically and numerically by [160, 161]. Of course this scaling is only valid for $Ca > Ca_c$ since otherwise, the fluid deposition does not depend on Ca but strongly depends on α. Thus, combining (i) the scaling law proposed by De Lozàr & al. [161] for the effective capillary number, (ii) Aussilous & Quéré law [133] for the evolution of the wet fraction as a function of the capillary number and (iii) the matching condition at the critical capillary number between the static and dynamic behavior gives:

$$m_d = 1 - \tilde{S}_r = \frac{m_s + G\left[(\hat{Ca}/\hat{Ca}_c)^{2/3} - 1\right]}{\left[1 + H((\hat{Ca}/\hat{Ca}_c)^{2/3} - 1)\right]} \text{ for } Ca > Ca_c \tag{3.23}$$

where the coefficients $G = 1.05$ and $H = 1.75$ are obtained from best fit with De Lozàr & al. [160] experimental data.

Finally, $\tilde{S}_r$ is taken as $\tilde{S}_r = m_s - 1$ when the plug moves at a capillary number lower than Ca_c and $\tilde{S}_r = m_d - 1$ above. This is of course an approximation since the experimentally observed transition between the dynamic and static regime at $Ca \sim Ca_c$ is more progressive [160].

3.3.3 Numerical resolution of the equations

The closed set of equations (3.16), (3.19), (3.22) and (3.23) are also solved using a first order Euler explicit scheme to predict the speed and the evolution of the length of the liquid plug. To cope with the strong acceleration of the liquid plug, an adaptive time step refinement is used: the spatial displacement $\Delta\tilde{x} = x_r^{n+1} - x_r^n$ is kept constant and thus the time step $\Delta\tilde{t}^n$ at iteration n is calculated from the formula: $\Delta\tilde{t}^n = \Delta\tilde{x}Ca^{n-1}$. Convergence on $\Delta\tilde{x}$ has been verified for all the simulations provided in this chapter.

3.4 Effect of the transition between static and dynamic film deposition on the dynamics of a liquid plug driven by a unidirectional forcing

3.4.1 Direct experimental evidence of the transition

The transition between the static and dynamic liquid film deposition and the associated changes in the plug dynamics are evidenced on Fig. 3.6 a-d. These figures illustrate the evolution of a liquid plug of initial size $L_o = 3.5$ mm driven by a unidirectional pressure head $\Delta P_t = 1000e^{-3e^{-10t}}\,Pa$.

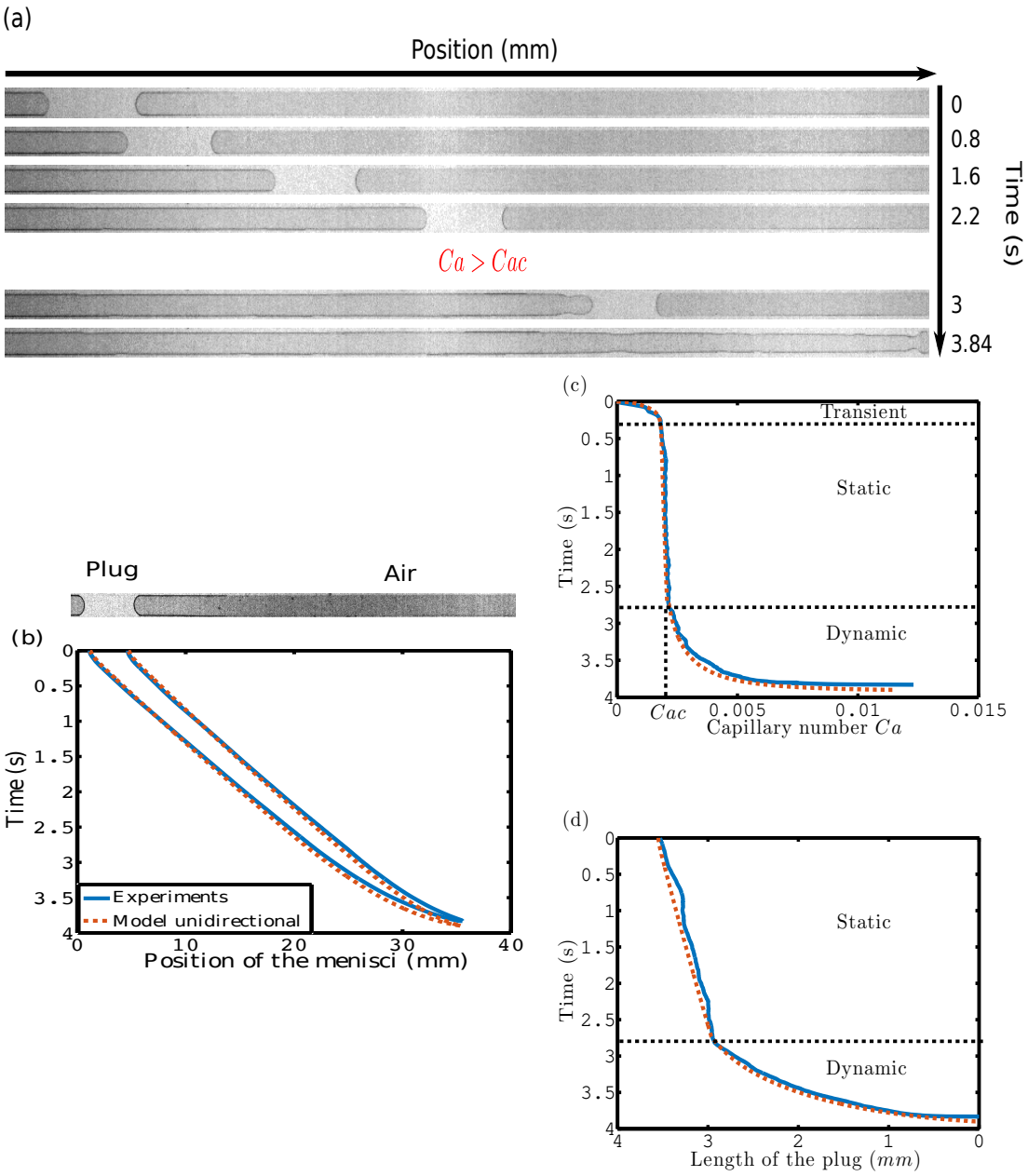

Figure 3.6 – Dynamics of a liquid plug of initial length $L_0 = 3.55mm$ pushed in a dry rectangular microfluidic channel with a unidirectional pressure head $\Delta P_t = 1000e^{-3e^{-10t}}Pa$:
(a) Stack showing the evolution of the plug below and above the critical capillary number Ca_c. Liquid (air) appears light (dark) grey.
(b) Position of the rear and front interfaces (menisci) as a function of time.
(c) Evolution of the capillary number as a function of time.
(d) Evolution of the plug length as a function of time. Blue solid curves correspond to experimental measurements and red dashed curves to simulations.

Blue curves correspond to experimental measurements while red curves correspond to simulations with the model developed in the previous section. Fig. 3.6a is obtained by stacking snapshots of the plug evolution every 8 ms when the capillary number lies below its critical value Ca_c and then later on when Ca exceeds Ca_c. When $Ca < Ca_c$ no liquid film is visible on the channel sides since liquid deposition only occurs in the corner of the tube, while this film is clearly visible when Ca exceeds Ca_c.

Figure 3.6b shows the position of the front and rear interfaces as a function of time. Figure 3.6c shows the evolution of the capillary number. The black dashed line (also reported on Fig. 3.6d) marks the transition (at time $t_c \approx 2.8$s) between the static and dynamic film deposition regimes. It corresponds to the time when Ca reaches the critical value $Ca_c = 2 \pm 0.1 \times 10^{-3}$. Before t_c and after the end of the transient regime ($t > t_t = 0.3$ s) (corresponding to the time required for the pressure controller to achieve a constant value), the increase in the capillary number is very slow. This leads to a quasi-linear variation of the plug size as a function of time as can be seen on Fig. 3.6d since the wet fraction m is constant in the static regime. Then, when the value of the capillary number overcomes the critical value Ca_c, the plug undergoes a strong acceleration leading to more and more fluid deposition and eventually to the plug rupture.

Excellent agreement between the simulations (red) and experiments (blue) is achieved for the evolutions of (i) the position of the interface (Fig. 3.6 b), (ii) the plug dimensionless speed (Fig. 3.6 c) and (iii) the plug length (Fig. 3.6 d). Our reduced dimension model thus properly captures the main physical ingredients. This model can be used to rationalize the observed tendencies: In the *static film deposition regime*, the value of the pressure head prescribes an initial value of the capillary number and the size of the plug diminishes quasi-linearly due to film deposition in the corners of the tube. This regular diminution of the plug size leads to a reduction of the viscous resistance of the plug to motion since the viscous pressure drop depends linearly on L_p. This induces a slow increase in the liquid plug speed (since the viscous resistance is weak compared to interfacial resistances). Nevertheless, since m does not depends on Ca, there is no retroaction of the evolution of the plug speed on the liquid film deposition and thus the evolution remains relatively stable. In the *dynamic film deposition*

regime however, the increase in the plug speed leads to more film deposition according to equation (3.23), itself leading to an acceleration of the plug speed.

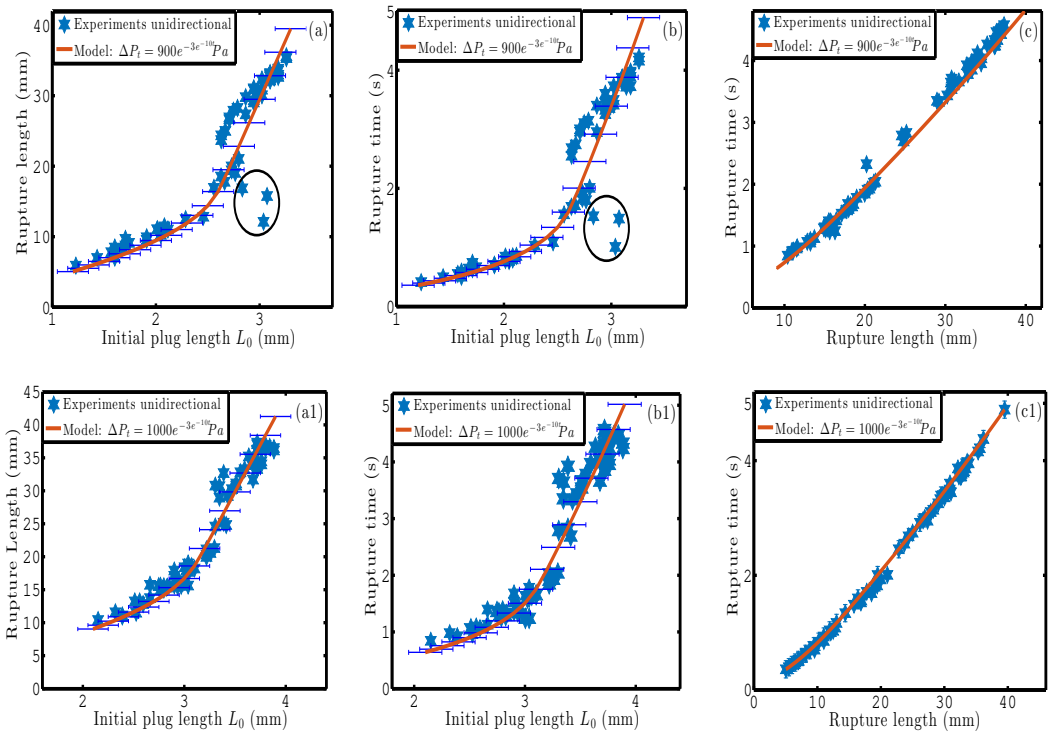

Figure 3.7 – Rupture lengths (a-a1) and rupture times (b-b1) of a set of liquid plugs as a function their initial lengths when they move on a dry rectangular microfluidic channel under two driving pressure $\Delta P_t = 900e^{-3e^{-10t}}Pa$ (a-b-c) and $\Delta P_t = 1000e^{-3e^{-10t}}Pa$ (a1-b1-c1). The rupture lengths as a function of the rupture times are given in figures (c-c1). The blue stars correspond to experiments and the red lines to simulations with the model developed in section 3.3. A circle surrounds three datas which are out of the global tendency. The most likely reason of this dispersion is that the microfluidic channel was not dried properly and there were some liquid remaining at the front interface that lubricated the channel and thus accelerated the plug motion leading to reduced rupture time and length.

This retroaction is at the origin of the massive acceleration of the plug and rapid evolution of its size when Ca exceeds Ca_c. This behavior is reminiscent of what is observed in cylindrical tubes [97, 167] while the static film deposition regime only occurs in polygonal channels.

3.4.2 Influence of this transition on the plugs rupture time and rupture length

We performed numerous experiments (represented on Fig. 3.7) for different initial plug lengths L_o and two different driving pressure ($\Delta P_t = 900e^{-3e^{-10t}}Pa$ and $\Delta P_t = 1000e^{-3e^{-10t}}Pa$) to analyse the evolution of the plug rupture time and rupture length in rectangular microchannels. The rupture time is the time required for the plug to rupture ($L_p = 0$) while the rupture length is the distance traveled by the liquid plug ($D_l = max(X_f) - min(X_r)$) before its rupture. These two parameters quantify the stability of a liquid plug to breaking. The quantitative agreement between experiments (blue stars) and simulations (red lines) enables to validate our model on an an extensive set of experimental data.

Again a transition between two distinct regimes is clearly evidenced on Fig. 3.7 (for both the rupture time and the rupture length) at a driving pressure-dependent critical initial plug length L_o^c ($L_o^c \approx 2.6$ mm for $\Delta P_t = 900$ Pa and $L_o^c \approx 3.1$ mm for $\Delta P_t = 1000$) Pa. Under this critical value of the initial plug length $L_o < L_o^c$, the initial dimensionless plug speed lies above the critical capillary number and thus the dynamics of the liquid plug is only in the dynamic film deposition regime. Thus the plug accelerates rapidly leading to rapid rupture of the plug on a short propagation length scale. Above, this critical initial length $L_o > L_o^c$, the initial capillary number lies under the critical number Ca_c and thus the plug dynamics is initially in the static film deposition regime. This regime leads to larger plug rupture time and thus propagation distance. Moreover, since in this regime the acceleration is weak, the rupture time and rupture length remain relatively linear function of the plug initial length (see Fig. 3.7). From this analysis, we can infer a theoretical evaluation of the critical initial length L_o^c, which delimits the transition between these two regimes. Indeed, L_o^c corresponds to the plug initial length when the initial capillary number is equal to the critical capillary number Ca_c. From equation (3.15) and by approximating S_r by wh at first order, we obtain:

$$L_o^c = \frac{h}{12Ca_c}\left[\frac{\Delta P_t h}{\sigma} - (E^2 + 2Df(\alpha))Ca_c^{2/3}\right]$$

This formula gives $L_o^c = 3.1 \pm 0.2$ mm and $L_o^c = 3.5 \pm 0.2$ mm for $\Delta P_t = 900$ Pa and $\Delta P_t = 1000$ Pa respectively. It slightly overestimates the critical length but nevertheless remains in good agreement with the experimentally measured values. This formula is also consistent with the increase in L_o^c as a function of ΔP_t observed experimentally. This theoretical prediction of the critical initial length L_o^c is of the upmost practical interest since it enables to predict in which regime will mainly evolve a liquid plug depending on its initial length. An interesting point is also that despite the regime change, the rupture length and rupture time remain relatively proportional to each other (Fig. 3.7 c and c1).

3.4.3 Comparison with the dynamics in cylindrical tubes

Figure 3.8 compares the rupture time and length obtained in rectangular and cylindrical tubes in the same range of capillary number ($5.5 \times 10^{-5} \lesssim Ca \lesssim 1.2 \times 10^{-2}$). As mentioned before, there is no static regime in cylindrical tubes and thus only the dynamic regime is observed on Fig. 3.8 (a2-b2).

3.5 Response of liquid plugs to periodic pressure forcings in rectangular microfluidic channels

3.5.1 Detailed analysis of single plug ruptures.

We further investigated the response of liquid plugs to cyclic forcing. For this purpose, liquid plugs are inserted at the center of a rectangular microfluidic channel and a cyclic pressure forcing (represented on Fig. 3.4b) is applied. Fig. 3.9 illustrates the positions of the rear and front interfaces (a-c-e) and the evolution of the plug length (b-d-f) for three different initial plug lengths: $L_1 = 3.8$ mm (a,b), $L_2 = 4.1$ mm (c,d) and $L_3 = 4.5$ mm (e,f). The blue curves correspond to experiments and the red curves to simulations. For these 3 initial lengths, the plugs undergo oscillations eventually leading to their rupture. The experimental results show that the evolution of the plug length is not monotonous: the plug size first increases and then decreases during each back and forth motion. This is a consequence of the progressive increase in the driving pressure (Fig. 3.4b): at

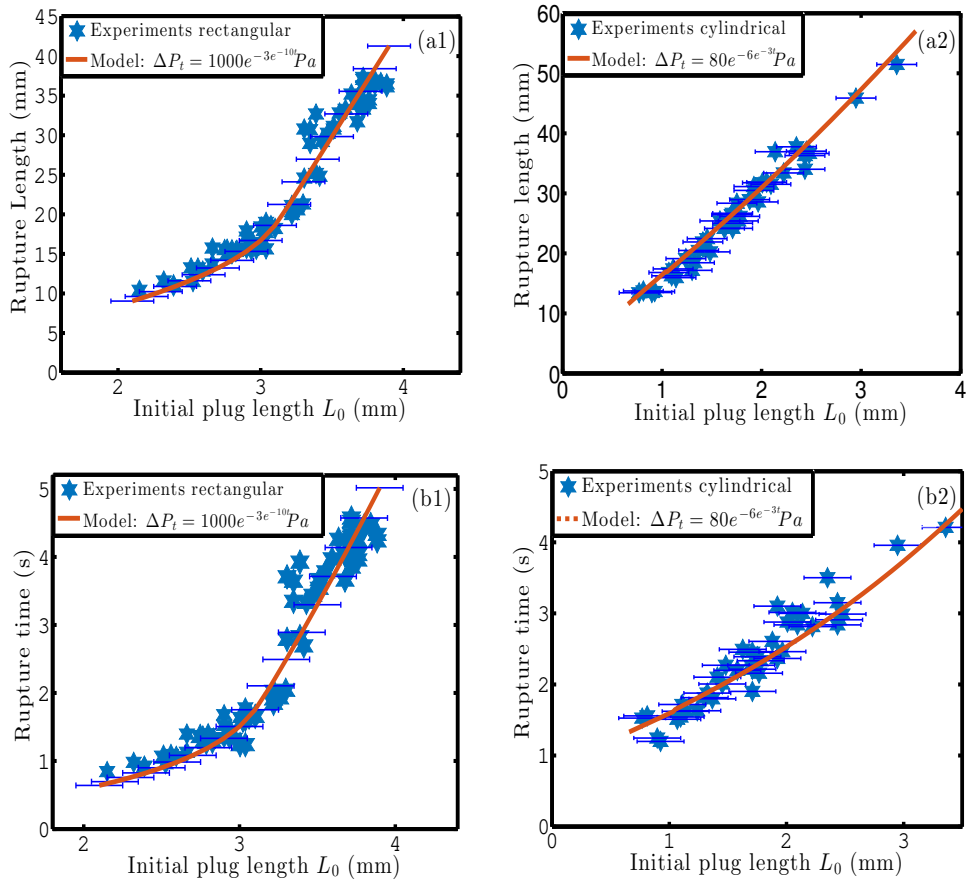

Figure 3.8 – Rupture lengths (a1) and rupture times (b1) of a liquid plug moving in a rectangular microfluidic channel under the pressure driving $\Delta P_t = 1000e^{-3e^{-10t}}$ Pa compared to the rupture lengths (a2) and rupture times (b2) of a liquid plug moving a cylindrical capillary tube of radius $R = 0.235$ mm under the pressure driving $\Delta P_t = 80e^{-6e^{-3t}}$ Pa (a2-b2) . The blue stars correspond to experiments and red curves to simulations.

the beginning the driving pressure is low, the plug moves slowly and leaves less liquid behind it that it recovers from the liquid film lying in front of it. Then, when the driving pressure reaches a critical pressure (derived in Magniez & al. [97] in the case of cylindrical tubes), the tendency is inverted.

The number of oscillations before the plug rupture increases with the initial length of the plug. For the longest plug ($L_3 = 4.5$ mm), a clear transition can be seen between a first phase where the plug undergoes relatively stable oscillations

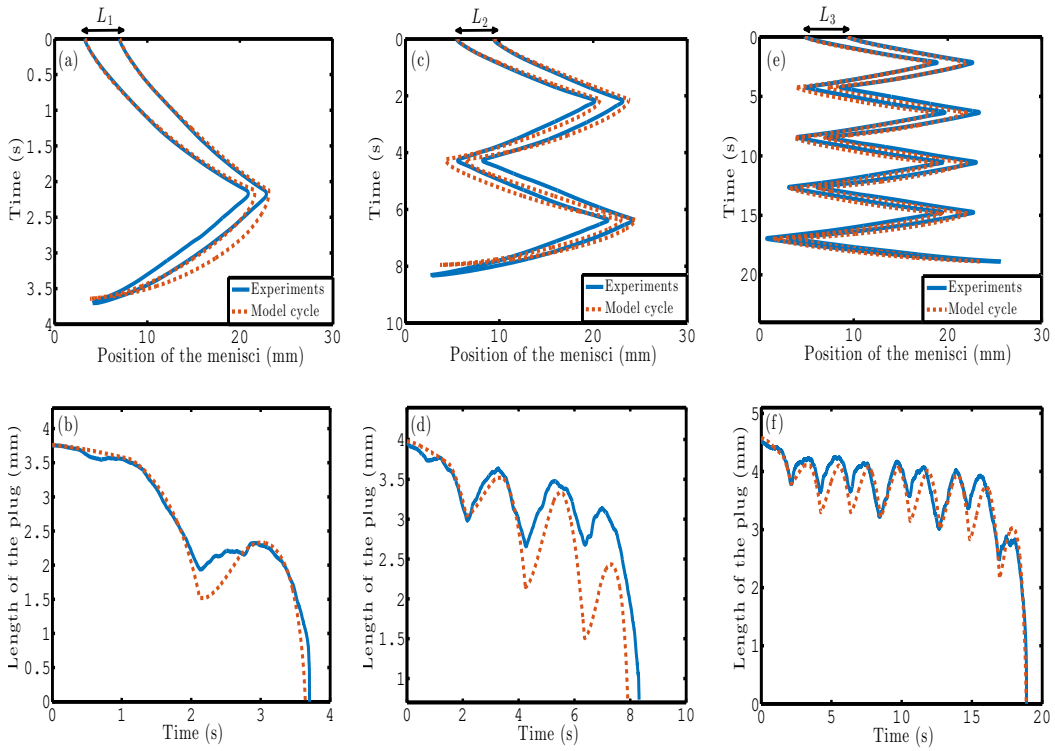

Figure 3.9 – Spatiotemporal evolution of three plugs of initial lengths (a-b) $L_1 = 3.85$ mm, (c-d) $L_2 = 4.1$ mm and (e-f) $L_3 = 4.5$ mm driven by the cyclic pressure forcing represented on Fig. 3.4(b). (a-c-e) Positions of the left and right menisci as a function of time. (b-d-f) Evolution of the length of the plug as a function of time.

with weak net evolution of its length from one cycle to another (see Fig. 3.9 before time $t = 15$ s) and a second phase with a brutal acceleration of the plug rapidly leading to its rupture ($t \geq 15$s)

3.5.2 Specificity of the cyclic dynamics of liquid plugs in rectangular channels compared to cylindrical channels.

Such transition is not observed in cylindrical tubes wherein the net variation of the plug size is more regular (see Fig. 3.10f). Signe & al. [167] demonstrated that in cylindrical channels, the two sources of the plug instability leading to its rupture are (i) the cyclic diminution of the plug viscous resistance to

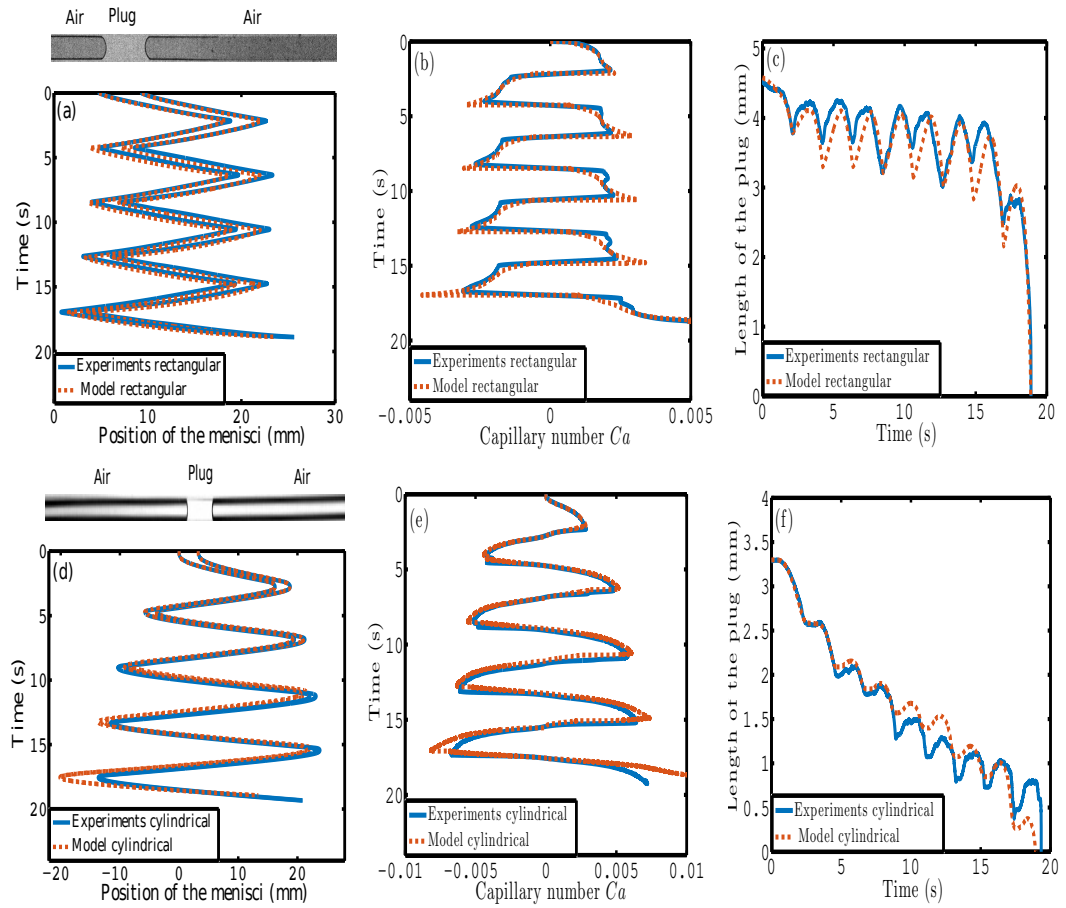

Figure 3.10 – (a-b-c) Spatiotemporal evolution of a liquid plug of initial length $L_1 = 4.5mm$ moving in a *rectangular microchannel* under the driving pressure represented on Fig. 3.4(b). (a) Position of the left and right menisci. (b) Evolution of the capillary number. (c) Evolution of the plug length. (d-e-f) Spatiotemporal evolution of a liquid plug of initial length $L_2 = 3.35mm$ moving in a *cylindrical capillary tube* of radius $R = 0.235mm$ driven by a cyclic forcing: $\Delta P_t = 78e^{-6e^{-3t}}Pa$ for $t \in [0, T]$, $\Delta P_t = (-1)^n(P_c - P_d)$ for $t \in [nT, (n+1)T]$ with $P_c = 78e^{-3e^{-3(t-nT)}}Pa$ and $P_d = 78e^{-1.4(t-nT)}e^{-0.02e^{-1.4*(t-nT)}}Pa$, $T = 2.15s$ with $2T = 4s$. (d) Position of the left and right menisci. (e) Evolution of the Capillary number. (f) Evolution of the plug length. For all experiments, the blue curves correspond to experiments and the red curves to simulations with the model presented in this chapter for experiments (a-b-c) in rectangular tube and the model presented in Signe & al. [167] for the experiments (d-e-f) in cylindrical tubes.

motion due to the diminution of its length and (ii) a cyclic reduction of the plug interfacial resistance due to the deposition of a liquid film of increasing thickness at each cycle and lubrication effects. A very interesting point is that these two instability sources rely on the amount of liquid deposited on the walls. If the amount of liquid left on the walls behind the liquid plug would remain constant, there would be no cyclic evolution of the plug size and no instability related to lubrication effects. Thus the plug would undergo stable periodic motion with no evolution of its size and no rupture.

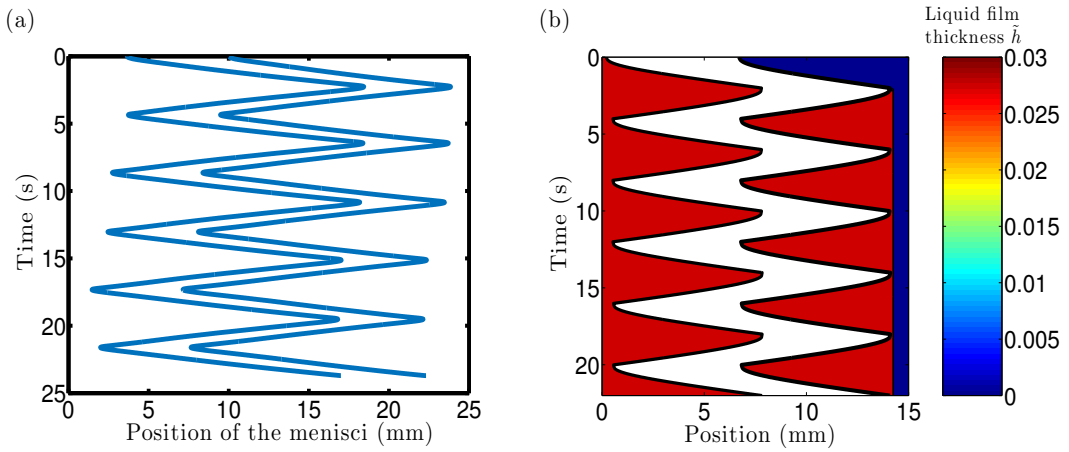

Figure 3.11 – (a) Evolution the positions of the left and right menisci of a plug of initial length $L_4 = 6.5$mm driven by the cyclic forcing represented on Fig. 3.4(b). We stopped the acquisition after 6 cycles since no significant of the plug length and speed from one cycle to the next was observed. (b) Simulations showing the predicted spatiotemporal evolution of the amount of liquid lying on the walls (wet fraction).

This behavior is indeed observed for plugs of initial length larger than $L_o^c = 4.7$mm (see Fig. 3.11a). In this case the plug always moves at a dimensionless speed smaller than the critical capillary number Ca_c. Since simulations and experiments are in good quantitative agreement, the simulations are used to monitor the evolution of the amount of liquid covering the walls (wet fraction) as a function of time. On Fig. 3.11b, we indeed see that the plug leaves a film of constant thickness (constant wet fraction m_s), thus leading to a zero cyclic mass balance.

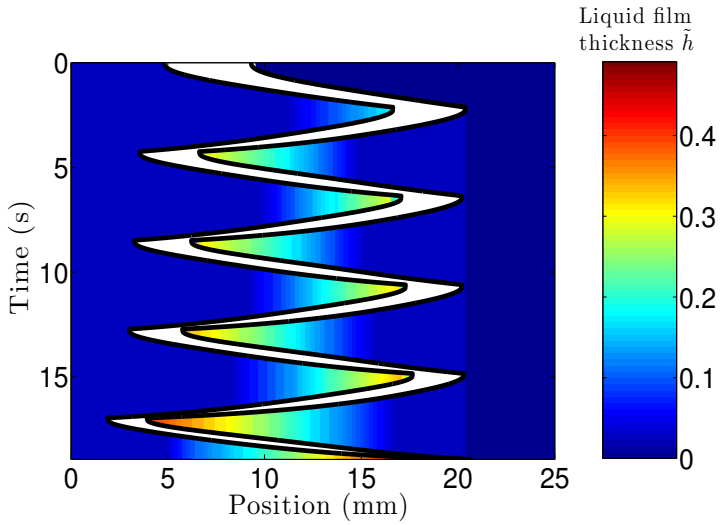

Figure 3.12 – Spatiotemporal evolution of the amount of liquid lying on the walls (wet fraction) for a plug of initial length $L_3 = 4.5mm$ driven by the cyclic pressure forcing Fig. 3.4(b). This figure correspond to the same experiment as Fig. 3.9 (e-f) and Fig. 3.10 (a-b-c)

To understand the transition occurring for plugs smaller than L_o^c we also plotted the evolution of the wet fraction as a function of time for the initial size $L_3 = 4.5$mm (see Fig. 3.12). In this case, the plug moves initially at a capillary number lying under the critical capillary number Ca_c thus leading to the deposition of a liquid film of constant thickness behind the plug. The plug speed increases progressively (see Fig. 3.10b) due to the increase in the driving pressure (see Fig. 3.4). At time $t \approx 1.5$s (see Fig. 3.12) the plug dimensionless speed overcomes Ca_c and the wet fractions starts increasing until the direction of motion changes (see Fig. 3.12). During the next cycles, the same behavior is observed with, at first, the deposition of a film of constant thickness and then the deposition of a film of increasing thickness (see Fig. 3.12). Nevertheless, at each cycle, (i) the plug travels further away, (ii) the plug size decreases, (iii) more and more liquid is left on the walls and (iv) the proportion of the motion above Ca_c increases. For time $t > 15$s the plug dimensionless speed exceeds Ca_c for the most part of the motion and this leads to a rapid evolution of the plug size and speed and eventually its rupture. This second phase is similar to the evolution

of liquid plugs in cylindrical tubes.

This analysis enables to set a criterion on the stability of a liquid plug driven by a pressure periodic cyclic forcing in a dry rectangular microchannel: If the plug dimensionless speed remains below Ca_c during the first cycle, then the plug dynamics will remain stable during the next cycles, while if the plug reaches Ca_c during this first cycle, it will accelerate cyclically and eventually rupture.

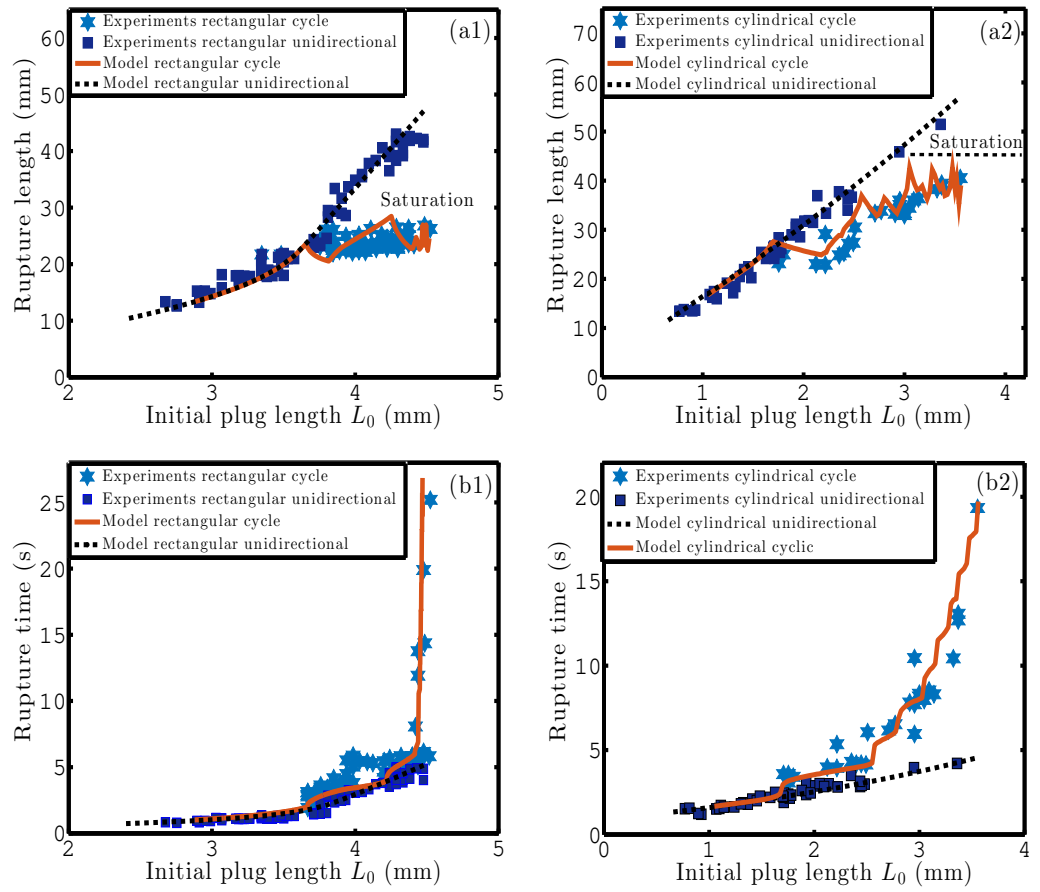

Figure 3.13 – (a1-a2) Rupture lengths and (b1-b2) rupture times for a cyclic or unidirectional pressure forcing in a rectangular (a1-b1) or cylindrical (a2-b2) channel. For rectangular channels, the pressure driving corresponds to the one represented on Fig. 3.4b and for cyclic pressure driving, it correspond to the one described in Fig. 3.10. Blue stars correspond to experiments with cyclic forcing, black squares to experiments with unidirectional pressure forcing, red solid lines to simulations for cyclic pressure forcing and black dashed lines to simulations with unidirectional pressure driving.

3.5.3 Evolution of the rupture time and rupture length and comparison between cyclic and unidirectional forcing.

To get a parametric overview of plugs dynamics in rectangular microchannels, we performed hundreds experiments with different plug initial lengths and either unidirectional or cyclic pressure drivings (of same maximal amplitude). The measured values of the rupture time and rupture length are represented on Fig. 3.13a1, b1) and compared to the evolutions in cylindrical tubes Fig. 3.13a2, b2). As previously reported in cylindrical channels, we observe a saturation of the rupture length when the plug starts undergoing cycles. Nevertheless a major difference with cylindrical tubes is that the rupture time increases to infinity for a finite value of the critical initial length $L_0^c \approx 4.7$mm while the increase in the rupture time was shown to follow a more "gradual" exponential trend in Signe & al. [167]. This is again a consequence of the existence of the static deposition regime in rectangular channels which does not exist in cylindrical tubes. Of course, in any case, the rupture time is never really infinite owing to evaporation of the plug occurring in the channel.

3.6 Conclusion

In this chapter, we studied the dynamics of single liquid plugs in rectangular microfluidic channels under unidirectional and cyclic pressure forcing. First, we showed that the transition between static and dynamic film deposition regimes leads to a dramatic acceleration of the plug rapidly leading to its rupture. A pressure-dependent critical size for the transition between these two regimes is derived analytically. For cyclic periodic pressure forcing, we showed that two regimes can occur depending on the initial size of the plug: the plug can either undergo stable periodic oscillations or cyclically accelerate and eventually rupture. The stable regime is observed when the plug dimensionless speed remains below a critical capillary number during the first cycle, while the second is observed as soon as the plug overcomes this value during the first cycle. We were able to quantitatively reproduce the evolution with a reduced dimension model obtained from the combination of previous elements introduced in chap-

ter 1 with additional elements to consider the transition between the static and dynamic film deposition regimes.

These results are of primary interest since microfluidic channels with polygonal cross sections are widely used in the field of microfluidics owing to their easy fabrication. In particular, for the study of liquid plugs dynamics in complex geometries, such as airway tree, it is extremely difficult to design trees with cylindrical sections. Thus, this work also enable to analyse and transpose results obtained in rectangular channels to cylindrical channels and understand the pertinence and limit of such comparison.

Chapter 4

Ongoing work: Cyclic dynamics of liquid plugs in synthetic tree networks

Abstract

In this chapter, we present preliminary experimental results on the dynamics of single liquid plugs inserted inside a five generations PDMS synthetic network and driven by a cyclic forcing. Three main regimes are identified as the driving pressure level is decreased: A first regime wherein all daughter plugs break during the first half cycle and hence do not enter cyclic evolution. A second regime wherein at least one path is reopened during the first half cycle, but some daughter plug survive and oscillate until their rupture. And a third regime wherein no plug breaks during the first cycle and all daughter plugs enter cyclic motion. Each of these transitions leads to a dramatic increase in the total time required to reopen the entire network. The physics learnt from the previous chapters helps us understanding qualitatively the tendencies, yet, much work is still needed to extract the physics behind all these experimental data.

4.1 Introduction

Two-phase gas-liquid flow in complex networks is a hydrodynamic problem with practical applications in a variety of engineered systems including flow in porous media [114, 116, 117], enhanced oil recovery [112], the stability of flow in microfluidic device [174, 175, 172, 176] and in natural systems as the network in a tree leaf [177] or the human pulmonary airway tree. This last case motivated many numerical [178, 179, 68, 180, 181, 152], experimental [71, 114, 182, 183, 149] and theoretical studies [184, 172, 96], which attempt to analyse and model the dynamics of liquid plugs in bifurcating microchannels and understand the physical interactions that occur between the flowing fluids and the network. Nevertheless, to the best of our knowledge, no experiments have been performed for cyclic dynamics of plugs in networks and there are few comparisons in the literature of the models with carefully controlled experiments.

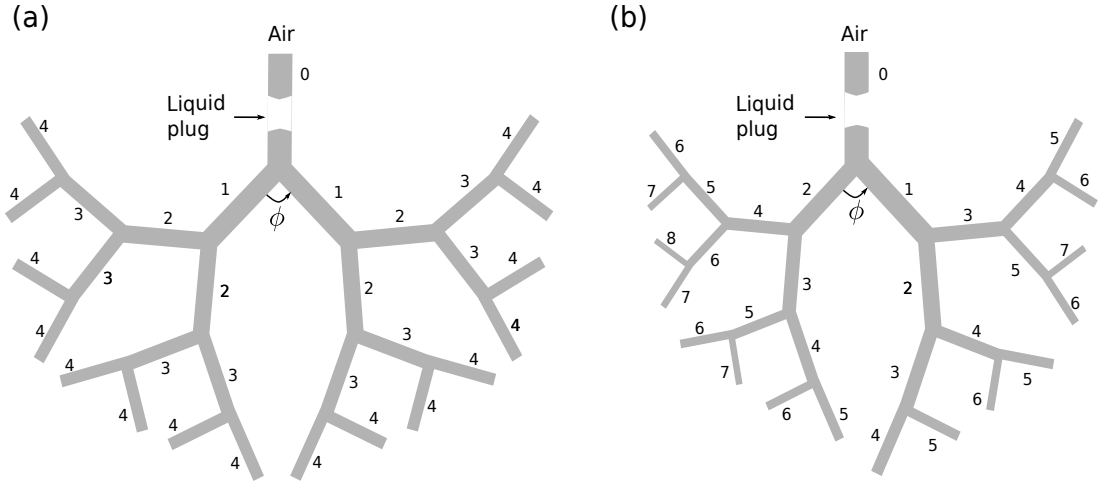

Figure 4.1 – Models of 5 generations tree-like networks of the lung obstructed by a liquid plug used for the experimental design of the PDMS networks. The first branch numbered 0 divides in successive generations:
(a) Symmetric model: each branch in a generation of the network divides dichotomously in successive daughter branches.
(b) Asymmetric model: each branch of the network gives rise to the following two next daughter branches.
The branching angle $\phi = 90^o$ is kept constant in all the branches of the networks.

In the previous chapters, we have shown that the dynamics of a liquid plug in a straight channel depends on the type of forcings (flow rate or pressure head), the liquid film history during the flow, the magnitude and the frequency of the cyclic forcing, and the geometry of the channel (cylindrical or polygonal). The connections between different branches in a network of microchannels makes the analysis of the dynamics of the liquid plugs more complex due to local and global interactions that occur through the connected network which allow the flow in a given generation to influence the flow in the other regions of the branching network [96]. The number of levels in the network also play an important role because during a cyclic motion, the liquid plugs can oscillate in between successive generations of the branching tree. Therefore, the physical interactions between the flowing fluids and the connected network depend on all those parameters which are, for most of them not accounted for in all the aforementioned studies.

In this chapter, we present an experimental study on the flow and rupture of liquid plugs in two polydimethylsiloxane (PDMS) microfluidic tree-like networks: one symmetric and one asymmetric (see Fig. 4.1). The liquid plugs experience a pressure cyclic forcing of oscillation period close to a real breathing cycle ($2T = 4$ s) and pressure levels comparable to the alveolar pressure. Our first analysis of the experiments shows that depending on the pressure magnitude, several regimes exist with either the breaking of all the liquid plugs during the first half-cycle or the persistence of liquid plugs in the airways, which undergo cyclic motion until their rupture. The transition between the straight and cyclic behavior leads to a dramatic increase in the total reopening time of the network. An interesting point, is that the second regime (persistence of liquid plugs and oscillations in a single generation) is reminiscent of the configurations studied in the previous chapters. Nevertheless the slow motion of the liquid plugs in this regime leads to static film deposition, and hence high rupture time of the liquid plug... This means that while the preliminary distribution and division of the plugs in the network is probably relatively similar to what happens in cylindrical channels, their persistence time is dramatically increased by the existence of the static deposition regime in our rectangular channels.

4.2 Method

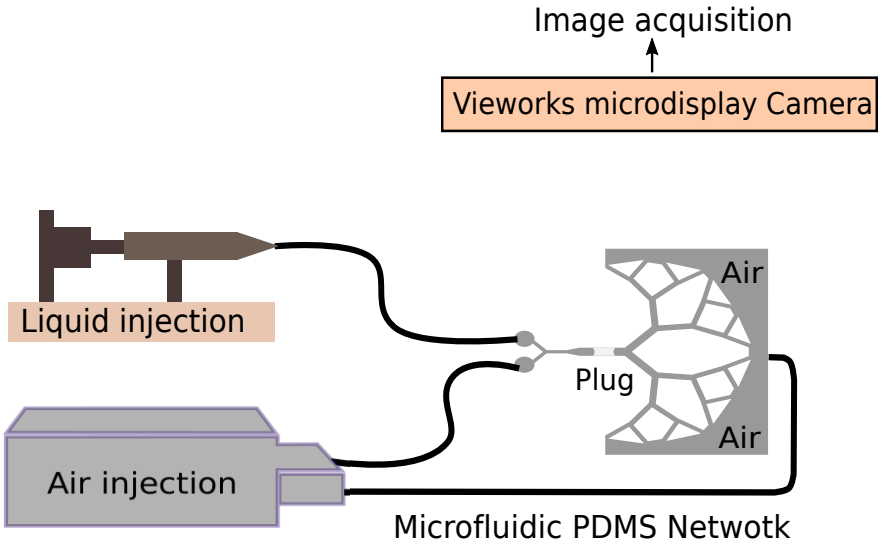

Figure 4.2 – Sketch of the experimental setup. A liquid plug is created inside a rectangular PDMS tree-like network by pushing alternatively some liquid and some air at a Y-junction. The liquid is pushed by a syringe pump while the air is pushed by a MFCS pressure controller. Then the liquid plug is moved alternatively in both directions in a cyclic periodic driving.

The experimental setup is represented on Fig. 4.2. The experiments are conducted in rectangular polydimethylsiloxane (PDMS) microfluidic tree-like networks obtained by standard photolithography techniques already explained in chapter 3. The height $h = 45 \pm 2\mu m$ of the microfluidic network is fixed by the choice of the photoresist and the speed of the spin-coating, while the cross sectional ratio r between the branch number n and the branch number $n+1$ is kept constant $r = S_{n+1}/S_n = 0.83$, thus fixing the width w_n at each generation n as in Song & al. [185]. The channel lengths also decrease linearly with almost the same ratio and the branching angle is kept constant in the network $\phi = 90^o$. This value is consistent with the measured branching angles in airway generations of less than $1mm$ in diameter by Horsfield [17].

A perfluorodecalin liquid plug is then injected in the first generation 0 and is moved alternatively by periodic pressure cyclic drivings of different level varying from (200 to 900) Pa. The shape of the pressure forcing is complex owing to the

response time of the system but we succeeded to have almost the same pressure evolution for all experiments. Therefore we will only characterise the pressure driving by the maximum pressure level ΔP_t^{max} that is reached. The experiments are recorded with a Vieworks microdisplay camera allowing to take long time experiments with a suitable acquisition rate up to 350 images/s compared to the high speed camera that allowed to take up to (10000) images/s but in a very short time. The acquisition rate in the experiments are fixed according to the driving conditions. The resolution of the camera used is 1024×726 pixels and the trigger time 1/3000 s.

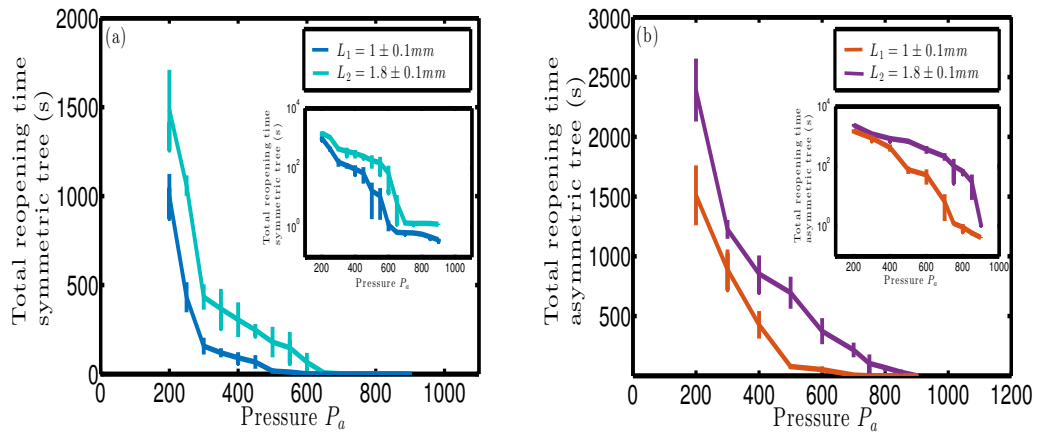

Figure 4.3 – Total reopening times of (a) the symmetric network and (b) the asymmetric network obstructed by a liquid plug of initial length $L_1 = 1 \pm 0.1$ mm and $L_2 = 1.8 \pm 0.1$ mm set in motion under different cyclic pressure driving of level ΔP_t^{max} varying from (200 to 900) Pa. Each experiment is repeated four times in the symmetric network and three times in the asymmetric network. The solid lines represent the mean value for the experiments.

4.3 Total reopening time and flow regimes in the tree-like networks

A single liquid plug of controlled size L is initially created in generation 0 of the network represented on Fig. 4.1 and driven by a cyclic pressure driving

of pressure level ΔP_t^{max}. The first parameter that we investigated is the time required for the network to be entirely reopen (all paths free), called total reopening time. We can see on Fig. 4.3 some sharp transition between different regimes. At high driving pressure the plug leaves a large amount of fluid behind it and its size evolves rapidly as it invades the network. Depending on the pressure level, it will divide one or several times into daughter plugs but all plugs will rupture during the first half cycle. This regime is observed on Fig. 4.3 (a) for pressure levels larger than 650 Pa for $L_1 = 1$mm and 700 Pa for $L2 = 1.8$ mm. We must underline that the channels are not prewetted, which leads to a rapid decrease of the plug length. Then, if all the daughter plugs do not break during the first cycle, they start undergoing cyclic motions in the network.

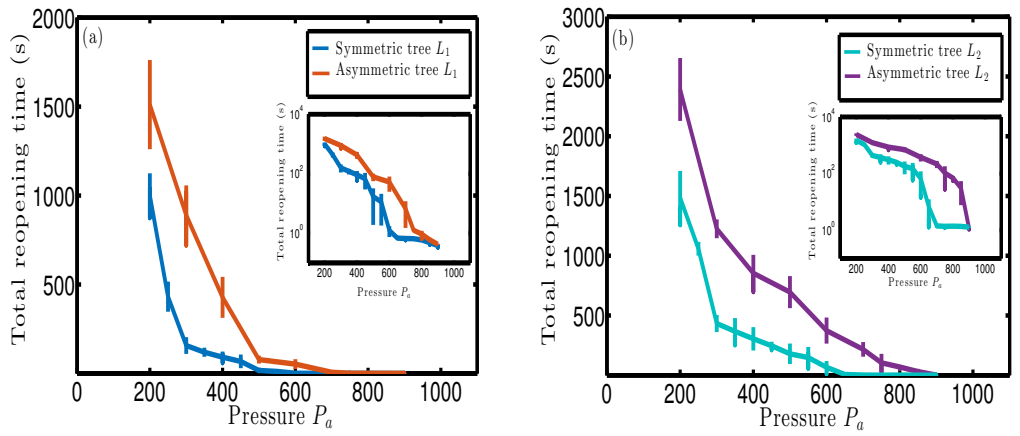

Figure 4.4 – Total reopening time in (a) the symmetric network compared to the asymmetric network (b) for two plug sizes $L_1 = 1 \pm 0.1$ mm and $L_2 = 1.8 \pm 0.1$ mm set in motion under different cyclic pressure driving of level ΔP_t^{max} varying from (200 to 900) Pa. The solid lines represent the mean values.

In practice, in most experiments, the daughter plugs only oscillate in one generation since a plug ruptured during the first half period, leading to large pressure decrease and they are not able to cross the bifurcations. When plug enter cyclic motions, their evolution is much slower since (i) the plug moves on a prewetted channel when it moves back, which slows down the evolution of its size as seen in chapter 1 (exponential increase in the rupture time when the

plug starts undergoing cycles) and (ii) at each plug rupture, the driving pressure in the network decreases dramatically and thus the plug enters the static film deposition regime which is extremely stable. We need now to analyse more closely what happens in the transition and find relevant quantities to quantify the evolutions in these two regimes.

4.4 Influence of the network geometry

If we compare the evolution in the asymmetric and symmetric networks Fig. 4.4, we see that the regimes are pretty similar except that the reopening time is significantly larger for the asymmetric network. We believe that it is mainly due to the fact that since the reduction in the network cross sections from one generation to the next is faster for the asymmetric network. This leads to a more rapid evolution of the network resistance in the asymmetric case and thus slower plug displacement for the same pressure driving. Again, this intuition needs to be quantified by measuring the average speed of the plugs per generation in each networks. Another interesting point is that the two curved converge for both high and low pressure. This is expected for the largest pressures since in this case, the plug break in the first generation of the network and thus the dynamics does not depend on the network geometry.

4.5 First pathway reopening time

As long as all pathways are closed by a liquid plug (there is a liquid plug in between all paths entrance and exit), each plug is driven by the same applied driving pressure ΔP_t^{max} since the pressure loss is mainly due to the presence of the plug (resistance of air can be neglected). Once a path is reopened, the air flows freely inside it, which leads to a drastic reduction of the driving pressure for all the remaining plugs since in a branching tree, all paths are connected. Thus it is essential to track down the first plug rupture to understand the tendencies. Fig. 4.5 shows the evolutions of the first pathway reopening time for each network and initial plug size L. If we look at the transition between

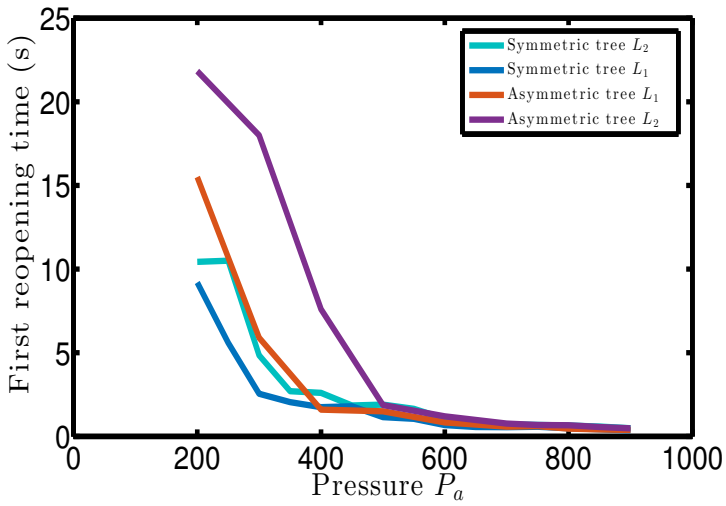

Figure 4.5 – Rupture time of the first liquid plug (thus reopening a path of the network) for the symmetric and asymmetric networks and the two plug sizes $L_1 = 1 \pm 0.1$ mm and $L_2 = 1.8 \pm 0.1$ mm as a function of the cyclic pressure driving level ΔP_t^{max} varying from (200 to 900) Pa. The solid lines represent the mean value of four experiments in the symmetric network and three experiments in the fractal network.

the rupture of the plug during the first half-cycle and its rupture during the next cycles, we see that the transition occurs at about 500 Pa for the asymmetric tree with plug initial length L_2, 400 Pa for the asymmetric tree with plug initial length L_1, 350 Pa for the symmetric tree with plug initial length L_2, and 300 Pa for the symmetric tree with plug initial length L_1. Each time, these transition leads to an obvious evolution of the trends for the total reopening time and in particular an increase in the slope of the total reopening time evolution.

4.6 Volume of reopened airway

The knowledge of the volume of reopened airway is of fundamental importance for pulmonary obstruction diseases because it gives informations on the evolution of the airway congestion during the breathing cycle. As we write this lines, we just obtained the evolution of the reopened volume as a function of time (see Fig. 4.6 and Fig. 4.7) for the different pressure levels but has not time to analyse

the tendencies yet...

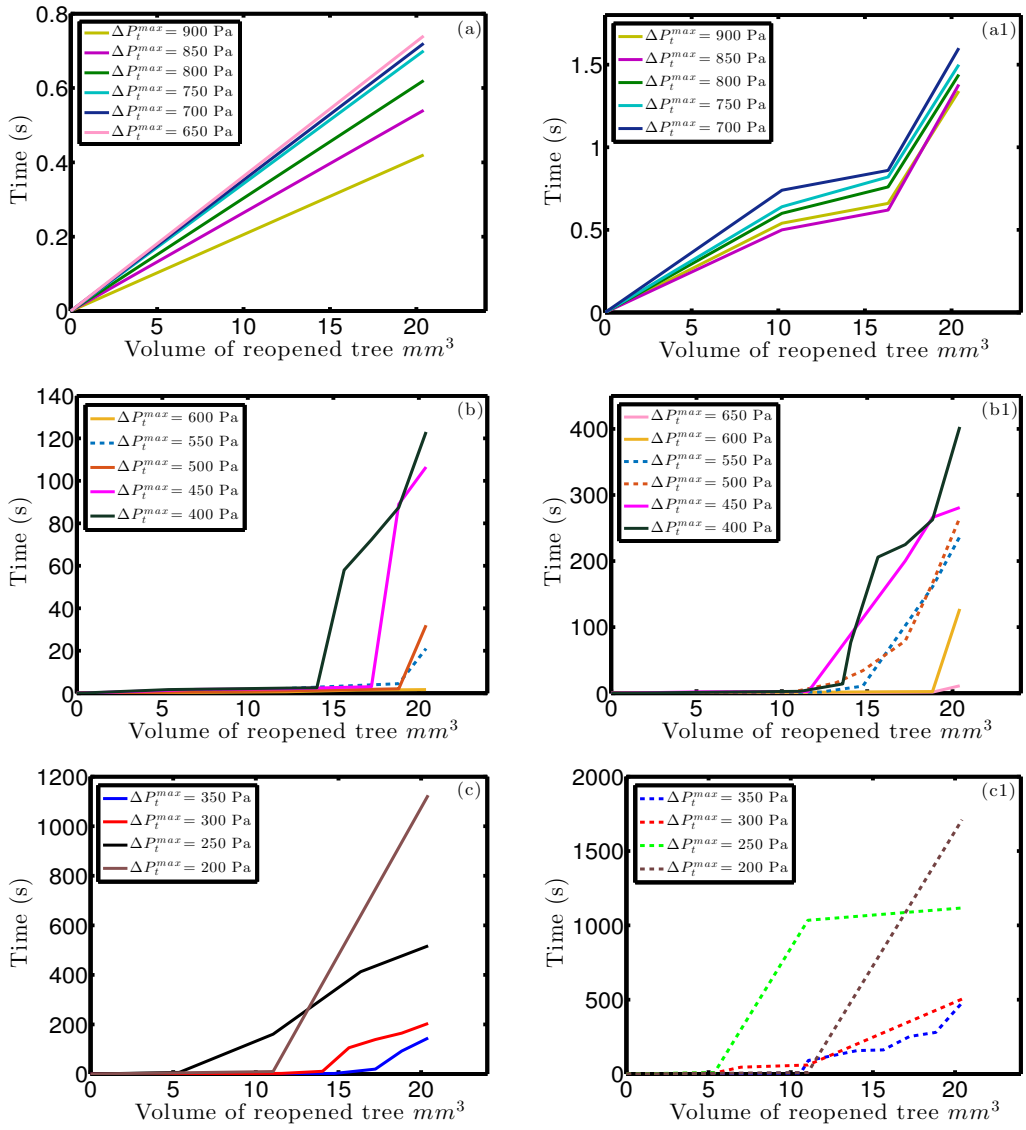

Figure 4.6 – Reopened volume of the symmetric network for a liquid plug of initial length $L_1 = 1 \pm 0.1$ mm (a-b-c) and $L_2 = 1.8 \pm 0.1$ mm (a1-b1-c1) under different cyclic pressure driving of level ΔP_t^{max} varying from (200 to 900) Pa. Solid lines show the situation in which the oscillations of the liquid plugs occur in a given generation of the network while dashed lines present the situation in which the oscillations occur between one or two generations of the network.

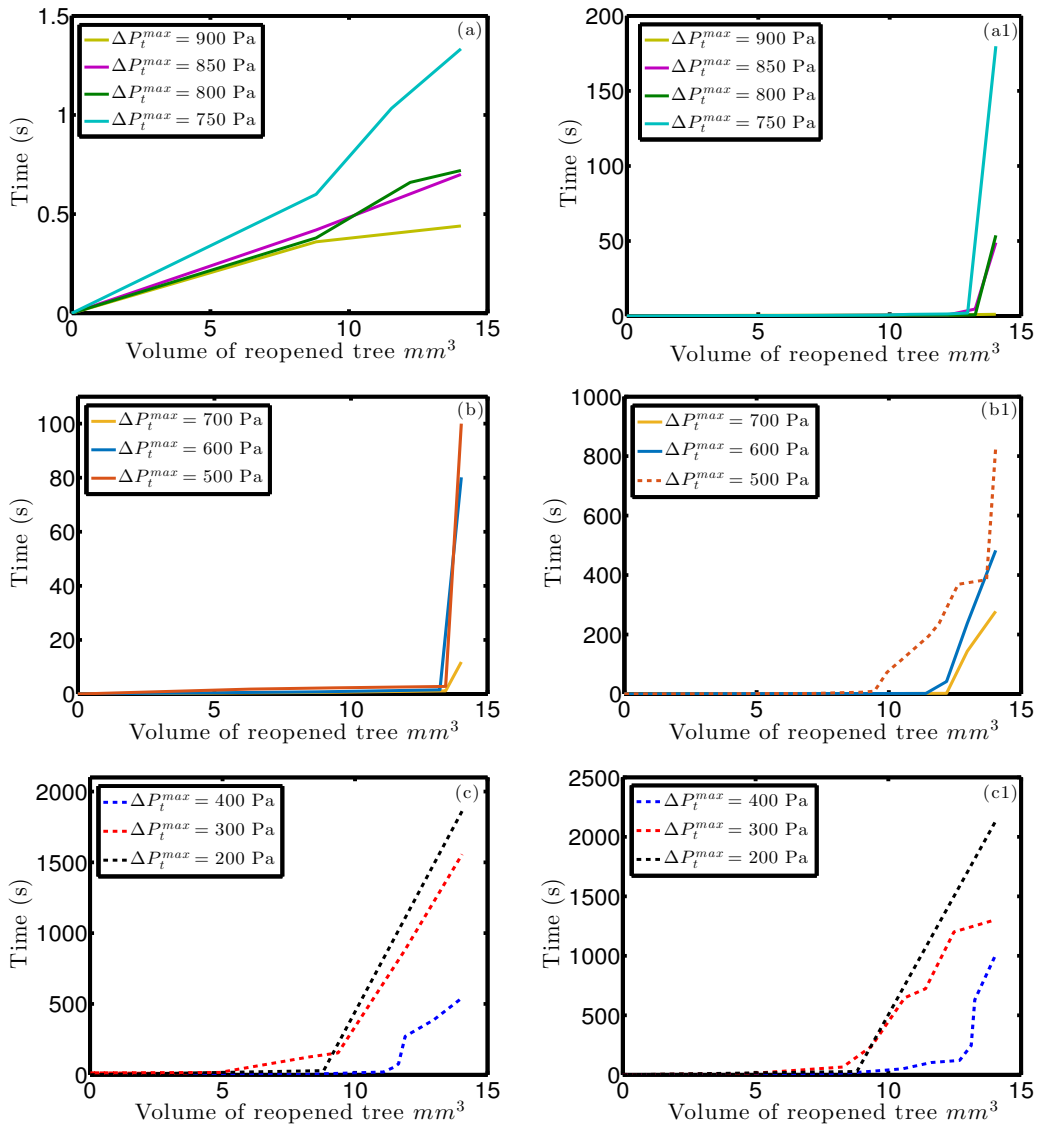

Figure 4.7 – Reopened volume of the asymmetric network for a liquid plug of initial length $L_1 = 1 \pm 0.1$ mm (a-b-c) and $L_2 = 1.8 \pm 0.1$ mm (a1-b1-c1) under different cyclic pressure driving of level ΔP_t^{max} varying from (200 to 900) Pa. Solid lines show the situation in which the oscillations of the liquid plugs occur in a given generation of the network while dashed lines present the situation in which the oscillations occur between one or two generations of the network.

4.7 Conclusion

In this chapter, we presented experimental preliminary results of the cyclic dynamics of liquid plugs in synthetic (PDMS) tree-like networks. These first results show some interesting tendencies, with the existence of different flow regimes. A substantial amount of time is nevertheless necessary to analyse them properly... Work in progress...

Conclusion and prospects

During this thesis, we studied experimentally and theoretically the response of liquid plugs to cyclic forcing in three different configurations: cylindrical rigid capillary tubes, rectangular (PDMS) channels and tree-like (PDMS) synthetic networks. Our starting motivation was to understand how mucus plugs behave in the lung tree during breathing cycles: do they break or do they persist depending on the intensity of the forcing and the thickness of the mucus lining.

Indeed, while there is an abundant literature on the dynamics of liquid plugs in tubes, almost all of these studies have been performed with constant flow rate or pressure driving, forcing conditions far from the ones occurring in the lungs during the breathing cycle. The study of the response of liquid plugs to cycles unveiled many interesting physical phenomena: the history role played by the film deposition, the existence of stable states with periodic oscillations of liquid plugs in prewetted tubes for pressure forcing or the fundamental role played by the transition between static and dynamic film deposition on the plug dynamics in rectangular channels. The models developed and validated in this thesis were then used to identify the critical pressures required to reopen airways obstructed by liquid plugs for a physiologically relevant forcing. This study underlines the key role played by the thickness of the liquid lining on the stability of the plugs and the higher driving pressure required to reopen more distal airways.

Since our initial motivation was the physiology of lungs in pathological conditions, one may wonder: why performing experiments in rectangular channels? First, it is extremely difficult to conceive cylindrical complex microfluidic networks, while it is much easier to conceive rectangular networks with soft photolithography. As a consequence, many studies on the dynamics of liquid plugs have been performed in rectangular tubes. It is therefore fundamental

to understand the physics in this geometry and to determine in which cases the results can be extrapolated to cylindrical geometries and in which cases the plug dynamics is fundamentally different. We are currently working a lot on the analysis of the results obtained in networks and how the tendencies apply or not to cylindrical networks. Second, rectangular channels obtained with soft lithography have become a standard in microfluidics setup and segmented gas-liquid flow appear in many research and industrial systems. Thus, it is equally important to understand the dynamics of liquid plugs in these geometries. Our study extends results in the literature to account for the variation of the channel geometry and the transition at a critical capillary number Ca_c, between the static m_s and the dynamic m_d wet fraction of liquid deposited during the cyclic motion.

This work raises many questions (What happens if the mucus is not Newtonian? Can we derive a model in a complex network? How to account for plugs division? What are the real forcing conditions in intermediate airways? What role is played by the walls elasticity?...) and provides only a few answers. Nevertheless, we hope that this thesis will add another small piece to the complex puzzle of the pulmonary airway flows and pave the way toward new studies.

Bibliography

[1] Gillian Pocock, Christopher D. Richards, and David Richards. *Human Physiology*. London: Methuen, 2013.

[2] John Burnard West. *Respiratory physiology: the essentials*. Lippincott Williams & Wilkins, 2012.

[3] Risa J Robinson, Jackie Russo, and Richard L Doolittle. "3D airway reconstruction using visible human data set and human casts with comparison to morphometric data". In: *The Anatomical Record* 292.7 (2009), pp. 1028–1044.

[4] Andrew S Weyrich and Guy A Zimmerman. "Platelets in lung biology". In: *Annual review of physiology* 75 (2013), pp. 569–591.

[5] Emma Lefrançais et al. "The lung is a site of platelet biogenesis and a reservoir for haematopoietic progenitors". In: *Nature* 544.7648 (2017), pp. 105–109.

[6] William F Ganong and William Ganong. *Review of medical physiology*. Appleton & Lange Norwalk, CT, 1995.

[7] Ireneusz Jabłoński and Janusz Mroczka. "A forward model of the respiratory system during airflow interruption". In: *Metrol. Meas. Syst* 16.2 (2009), pp. 219–232.

[8] Biogear. *Respiratory Methodology.* 2016.

[9] TJ Pedley. "Pulmonary fluid dynamics". In: *Annual Review of Fluid Mechanics* 9.1 (1977), pp. 229–274.

[10] Ewald R Weibel. *The pathway for oxygen: structure and function in the mammalian respiratory system*. Harvard University Press, 1984.

[11] Geoffrey B West, James H Brown, and Brian J Enquist. "A general model for the origin of allometric scaling laws in biology". In: *Science* 276.5309 (1997), pp. 122–126.

[12] James B Grotberg. "Respiratory fluid mechanics". In: *Physics of Fluids* 23.2 (2011), p. 021301.

[13] Keith Horsfield and Gordon Cumming. "Morphology of the bronchial tree in man." In: *Journal of Applied Physiology* 24.3 (1968), pp. 373–383.

[14] Keith Horsfield et al. "Models of the human bronchial tree." In: *Journal of applied physiology* 31.2 (1971), pp. 207–217.

[15] Ewald R Weibel. "Geometric and dimensional airway models of conductive, transitory and respiratory zones of the human lung". In: *Morphometry of the human lung*. Springer, 1963, pp. 136–142.

[16] Matthias Heil and Joseph P White. "Airway closure: surface-tension-driven non-axisymmetric instabilities of liquid-lined elastic rings". In: *Journal of Fluid Mechanics* 462 (2002), pp. 79–109.

[17] K Horsfield and G Cumming. "Angles of branching and diameters of branches in the human bronchial tree". In: *Bulletin of Mathematical Biology* 29.2 (1967), pp. 245–259.

[18] James B Grotberg. "Pulmonary flow and transport phenomena". In: *Annual Review of Fluid Mechanics* 26.1 (1994), pp. 529–571.

[19] BJ West, V Bhargava, and AL Goldberger. "Beyond the principle of similitude: renormalization in the bronchial tree". In: *Journal of Applied Physiology* 60.2 (2005), pp. 2166–2166.

[20] Benjamin Mauroy et al. "An optimal bronchial tree may be dangerous". In: *Nature* 427.6975 (2004), pp. 633–636.

[21] Thais Mauad et al. "Abnormal alveolar attachments with decreased elastic fiber content in distal lung in fatal asthma". In: *American journal of respiratory and critical care medicine* 170.8 (2004), pp. 857–862.

[22] Heinz Fehrenbach, Christina Wagner, and Michael Wegmann. "Airway remodeling in asthma: what really matters". In: *Cell and Tissue Research* (2017), pp. 1–19.

[23] Olatunji W Williams et al. "Airway mucus: from production to secretion". In: *American journal of respiratory cell and molecular biology* 34.5 (2006), pp. 527–536.

[24] John V Fahy and Burton F Dickey. "Airway mucus function and dysfunction". In: *New England Journal of Medicine* 363.23 (2010), pp. 2233–2247.

[25] W Holländer and W Stöber. "Aerosols of smoke, respiratory physiology and deposition". In: *Toxic Interfaces of Neurones, Smoke and Genes*. Springer, 1986, pp. 74–87.

[26] Duncan F Rogers. "Physiology of airway mucus secretion and pathophysiology of hypersecretion". In: *Respiratory care* 52.9 (2007), pp. 1134–1149.

[27] Richard A Cone. "Barrier properties of mucus". In: *Advanced drug delivery reviews* 61.2 (2009), pp. 75–85.

[28] Samuel K Lai et al. "Micro-and macrorheology of mucus". In: *Advanced drug delivery reviews* 61.2 (2009), pp. 86–100.

[29] Christopher Brennen and Howard Winet. "Fluid mechanics of propulsion by cilia and flagella". In: *Annual Review of Fluid Mechanics* 9.1 (1977), pp. 339–398.

[30] Konrad Morgenroth and Johannes Bolz. "Morphological features of the interaction between mucus and surfactant on the bronchial mucosa". In: *Respiration* 47.3 (1985), pp. 225–231.

[31] Yingying Hu et al. "A microfluidic model to study fluid dynamics of mucus plug rupture in small lung airways". In: *Biomicrofluidics* 9.4 (2015), p. 044119.

[32] M King and BK Rubin. "Mucus physiology and pathophysiology: therapeutic aspects". In: *LUNG BIOLOGY IN HEALTH AND DISEASE* 92 (1996), pp. 391–412.

[33] JA Moriarty and JB Grotberg. "Flow-induced instabilities of a mucus–serous bilayer". In: *Journal of Fluid Mechanics* 397 (1999), pp. 1–22.

[34] E Puchelle et al. "Elasto-thixotropic properties of bronchial mucus and polymer analogs". In: *Biorheology* 22.5 (1985), pp. 415–423.

[35] JH Widdicombe. "Regulation of the depth and composition of airway surface liquid". In: *Journal of anatomy* 201.4 (2002), pp. 313–318.

[36] SL Codd et al. "Tensile stiffness of ovine tracheal wall". In: *Journal of Applied Physiology* 76.6 (1994), pp. 2627–2635.

[37] D Yager et al. "Airway surface liquid thickness as a function of lung volume in small airways of the guinea pig". In: *Journal of Applied Physiology* 77.5 (1994), pp. 2333–2340.

[38] RD Kamm and RC Schroter. "Is airway closure caused by a liquid film instability?" In: *Respiration physiology* 75.2 (1989), pp. 141–156.

[39] Walter E Finkbeiner. "Physiology and pathology of tracheobronchial glands". In: *Respiration physiology* 118.2 (1999), pp. 77–83.

[40] Duncan F Rogers. "Airway goblet cell hyperplasia in asthma: hypersecretory and anti-inflammatory?" In: *Clinical & Experimental Allergy* 32.8 (2002), pp. 1124–1127.

[41] Nils Gunnar Toremalm. "The Daily Amount of Tracheo-Bronchial Secretions in Man: A Method for Continuous Tracheal Aspiration in Laryngectomized and Tracheotomized Patients". In: *Acta Oto-Laryngologica* 52.sup158 (1960), pp. 43–53.

[42] Mathieu Bottier et al. "A new index for characterizing micro-bead motion in a flow induced by ciliary beating: Part II, modeling". In: *PLoS computational biology* 13.7 (2017), e1005552.

[43] J Rodrigo Vélez-Cordero and Eric Lauga. "Waving transport and propulsion in a generalized Newtonian fluid". In: *Journal of Non-Newtonian Fluid Mechanics* 199 (2013), pp. 37–50.

[44] AJ Mautone and MB Cataletto. "Mechanical defense, mechanisms of the lung". In: *Pulmonary Physiology (Scarpelli EM, ed). Philadelphia: Lea and Febiger* (1990), pp. 192–214.

[45] David B Hill et al. "Force generation and dynamics of individual cilia under external loading". In: *Biophysical journal* 98.1 (2010), pp. 57–66.

[46] DJ Smith, EA Gaffney, and JR Blake. "Modelling mucociliary clearance". In: *Respiratory physiology & neurobiology* 163.1 (2008), pp. 178–188.

[47] Adam Wanner, Matthias Salathé, and Thomas G O'Riordan. "Mucociliary clearance in the airways." In: *American journal of respiratory and critical care medicine* 154.6 (1996), pp. 1868–1902.

[48] Larisa Gheber and Zvi Priel. "On metachronism in ciliary systems: a model describing the dependence of the metachronal wave properties on the intrinsic ciliary parameters". In: *Cytoskeleton* 16.3 (1990), pp. 167–181.

[49] Jens Elgeti, Roland G Winkler, and Gerhard Gompper. "Physics of microswimmers—single particle motion and collective behavior: a review". In: *Reports on progress in physics* 78.5 (2015), p. 056601.

[50] Babak Nasouri and Gwynn J Elfring. "Hydrodynamic interactions of cilia on a spherical body". In: *Physical Review E* 93.3 (2016), p. 033111.

[51] J Sade et al. "The role of mucus in transport by cilia". In: *American Review of Respiratory Disease* 102.1 (1970), pp. 48–52.

[52] John D Smart. "The basics and underlying mechanisms of mucoadhesion". In: *Advanced drug delivery reviews* 57.11 (2005), pp. 1556–1568.

[53] Michael R Knowles and Richard C Boucher. "Mucus clearance as a primary innate defense mechanism for mammalian airways". In: *The Journal of clinical investigation* 109.5 (2002), p. 571.

[54] Annie Viallat et al. "Circular flow patterns induced by ciliary activity in reconstituted human bronchial epithelium". In: *APS Meeting Abstracts*. 2016.

[55] BB Ross, R Gramiak, and H Rahn. "Physical dynamics of the cough mechanism". In: *J Appl Physiol* 8.3 (1955), pp. 264–268.

[56] David E Leith et al. "Cough". In: *Comprehensive Physiology* (1986).

[57] Virginie Duclaux, Christophe Clanet, and David Quéré. "The effects of gravity on the capillary instability in tubes." In: *Journal of Fluid Mechanics* 556 (2006), pp. 217–226.

[58] John K Sheehan et al. "Analysis of respiratory mucus glycoproteins in asthma: a detailed study from a patient who died in status asthmaticus." In: *American journal of respiratory cell and molecular biology* 13.6 (1995), pp. 748–756.

[59] Steven R Hays and John V Fahy. "The role of mucus in fatal asthma". In: *The American journal of medicine* 115.1 (2003), pp. 68–69.

[60] James C Hogg et al. "The nature of small-airway obstruction in chronic obstructive pulmonary disease". In: *New England Journal of Medicine* 350.26 (2004), pp. 2645–2653.

[61] Robert Tarran, Brian Button, and Richard C Boucher. "Regulation of normal and cystic fibrosis airway surface liquid volume by phasic shear stress". In: *Annu. Rev. Physiol.* 68 (2006), pp. 543–561.

[62] Richard C Boucher. "Cystic fibrosis: a disease of vulnerability to airway surface dehydration". In: *Trends in molecular medicine* 13.6 (2007), pp. 231–240.

[63] Anh L Innes et al. "Epithelial mucin stores are increased in the large airways of smokers with airflow obstruction". In: *CHEST Journal* 130.4 (2006), pp. 1102–1108.

[64] Virginie Duclaux. "Occlusions pulmonaires, Entropion oculaire et Anévrismes: une approche physique en physiologie". PhD thesis. Université de Provence-Aix-Marseille I, 2006.

[65] Walker Long et al. "Effects of two rescue doses of a synthetic surfactant on mortality rate and survival without bronchopulmonary dysplasia in 700-to 1350-gram infants with respiratory distress syndrome". In: *The Journal of pediatrics* 118.4 (1991), pp. 595–605.

[66] Hacer Yapıcıoğlu et al. "The use of surfactant in children with acute respiratory distress syndrome: efficacy in terms of oxygenation, ventilation and mortality". In: *Pulmonary pharmacology & therapeutics* 16.6 (2003), pp. 327–333.

[67] William A et al. Engle. "Surfactant-replacement therapy for respiratory distress in the preterm and term neonate." In: *Pediatrics* 121.2 (2008), pp. 419–432.

[68] Marcel Filoche, Cheng-Feng Tai, and James B Grotberg. "Three-dimensional model of surfactant replacement therapy." In: *Proceedings of the National Academy of Sciences* 112.30 (2015), pp. 9287–9292.

[69] Alan J Nimmo et al. "Intratracheal administration of glucocorticoids using surfactant as a vehicle". In: *Clinical and experimental pharmacology and physiology* 29.8 (2002), pp. 661–665.

[70] David Halpern et al. "Liquid and surfactant delivery into pulmonary airways". In: *Respiratory physiology & neurobiology* 163.1 (2008), pp. 222–231.

[71] Daner Abdula. "Bubbling and foaming assisted clearing of mucin plugs in microfluidic Y-junctions". In: *Journal of biomechanics* (2016).

[72] Bruce K Rubin, Oscar Ramirez, and Malcolm King. "Mucus rheology and transport in neonatal respiratory distress syndrome and the effect of surfactant therapy". In: *Chest* 101.4 (1992), pp. 1080–1085.

[73] GT De Sanctis et al. "Exogenous surfactant enhances mucociliary clearance in the anaesthetized dog". In: *European Respiratory Journal* 7.9 (1994), pp. 1616–1621.

[74] RV Craster and OK Matar. "Surfactant transport on mucus films". In: *Journal of Fluid Mechanics* 425 (2000), pp. 235–258.

[75] Matthias Heil, Andrew L Hazel, and Jaclyn A Smith. "The mechanics of airway closure." In: *Respiratory physiology & neurobiology* 163.1 (2008), pp. 214–221.

[76] Matthias Heil and Andrew L Hazel. "Fluid-structure interaction in internal physiological flows". In: *Annual review of fluid mechanics* 43 (2011), pp. 141–162.

[77] M Hell. "Airway closure: occluding liquid bridges in strongly buckled elastic tubes". In: *TRANSACTIONS-AMERICAN SOCIETY OF MECHANICAL ENGINEERS JOURNAL OF BIOMECHANICAL ENGINEERING* 121 (1999), pp. 487–493.

[78] FF Espinosa and RD Kamm. "Meniscus formation during tracheal instillation of surfactant". In: *Journal of Applied Physiology* 85.1 (1998), pp. 266–272.

[79] Ioana Laura Omocea et al. "Breakup of Liquid Jets". In: *Energy Procedia* 85 (2016), pp. 383–389.

[80] Joseph Plateau. "Experimental and theoretical statics of liquids subject to molecular forces only". In: (1873).

[81] Lord Rayleigh. "XVI. On the instability of a cylinder of viscous liquid under capillary force". In: *The London, Edinburgh, and Dublin Philosophical Magazine and Journal of Science* 34.207 (1892), pp. 145–154.

[82] Lord Rayleigh. "XIX. On the instability of cylindrical fluid surfaces". In: *The London, Edinburgh, and Dublin Philosophical Magazine and Journal of Science* 34.207 (1892), pp. 177–180.

[83] Subrahmanyan Chandrasekhar. *Hydrodynamic and hydromagnetic stability*. Courier Corporation, 1961.

[84] Jens Eggers. "Nonlinear dynamics and breakup of free-surface flows". In: *Reviews of modern physics* 69.3 (1997), p. 865.

[85] Peter T Macklem, Donald F Proctor, and James C Hogg. "The stability of peripheral airways". In: *Respiration physiology* 8.2 (1970), pp. 191–203.

[86] Adriano M Alencar et al. "Physiology: Dynamic instabilities in the inflating lung". In: *Nature* 417.6891 (2002), pp. 809–811.

[87] D Halpern and JB Grotberg. "Fluid-elastic instabilities of liquid-lined flexible tubes". In: *Journal of Fluid Mechanics* 244 (1992), pp. 615–632.

[88] James B Grotberg and Oliver E Jensen. "Biofluid mechanics in flexible tubes". In: *Annual Review of Fluid Mechanics* 36 (2004).

[89] Andrew L Hazel and Matthias Heil. "Steady finite-Reynolds-number flows in three-dimensional collapsible tubes". In: *Journal of fluid Mechanics* 486 (2003), pp. 79–103.

[90] David Halpern, Hideki Fujioka, and James B Grotberg. "The effect of viscoelasticity on the stability of a pulmonary airway liquid layer". In: *Physics of Fluids* 22.1 (2010), p. 011901.

[91] D Campana, J Di Paolo, and FA Saita. "A 2-D model of Rayleigh instability in capillary tubes—-surfactant effects". In: *International journal of multiphase flow* 30.5 (2004), pp. 431–454.

[92] Vinod Suresh and JB Grotberg. "The effect of gravity on liquid plug propagation in a two-dimensional channel". In: *Physics of Fluids* 17.3 (2005), p. 031507.

[93] Y. Zheng, H. Fujioka, and J.B. Grotberg. "Effect of gravity, inertia and surfactant on steady plug propagation in a two-dimensional channel". In: *Phys. Fluids* (2007), p. 082107.

[94] OE Jensen. "The thin liquid lining of a weakly curved cylindrical tube". In: *Journal of Fluid Mechanics* 331 (1997), pp. 373–403.

[95] Georg F Dietze and Christian Ruyer-Quil. "Films in narrow tubes". In: *Journal of Fluid Mechanics* 762 (2015), pp. 68–109.

[96] Michael Baudoin et al. "Airway reopening through catastrophic events in a hierarchical network." In: *Proceedings of the National Academy of Sciences* 110.3 (2013), pp. 859–864.

[97] JC Magniez et al. "Dynamics of liquid plugs in prewetted capillary tubes: from acceleration and rupture to deceleration and airway obstruction." In: *Soft Matter* 12.42 (2016), pp. 8710–8717.

[98] Sebastián Ubal et al. "Stability of the steady-state displacement of a liquid plug driven by a constant pressure difference along a prewetted capillary tube". In: *Industrial & Engineering Chemistry Research* 47.16 (2008), pp. 6307–6315.

[99] Hideki Fujioka et al. "Reduced-dimension model of liquid plug propagation in tubes". In: *Physical Review Fluids* 1.5 (2016), p. 053201.

[100] Parsa Zamankhan et al. "Steady motion of Bingham liquid plugs in two-dimensional channels". In: *Journal of Fluid Mechanics* 705 (2012), pp. 258–279.

[101] Hideki Fujioka and James B Grotberg. "The steady propagation of a surfactant-laden liquid plug in a two-dimensional channel". In: *Physics of Fluids (1994-present)* 17.8 (2005), p. 082102.

[102] Y Zheng et al. "Liquid plug propagation in flexible microchannels: a small airway model". In: *Physics of Fluids* 21.7 (2009), p. 071903.

[103] PD Howell, SL Waters, and JB Grotberg. "The propagation of a liquid bolus along a liquid-lined flexible tube". In: *Journal of fluid mechanics* 406 (2000), pp. 309–335.

[104] Andrew L Hazel and Matthias Heil. "Three-dimensional airway reopening: the steady propagation of a semi-infinite bubble into a buckled elastic tube". In: *Journal of Fluid Mechanics* 478 (2003), pp. 47–70.

[105] Anne Juel and Alexandra Heap. "The reopening of a collapsed fluid-filled elastic tube". In: *Journal of Fluid Mechanics* 572 (2007), pp. 287–310.

[106] Lucie Ducloué et al. "Reopening modes of a collapsed elasto-rigid channel". In: *Journal of Fluid Mechanics* 819 (2017), pp. 121–146.

[107] Donald P Gaver et al. "The steady motion of a semi-infinite bubble through a flexible-walled channel". In: *Journal of Fluid Mechanics* 319 (1996), pp. 25–65.

[108] HT Low, YT Chew, and CW Zhou. "Pulmonary airway reopening: effects of non-Newtonian fluid viscosity". In: *Journal of biomechanical engineering* 119.3 (1997), pp. 298–308.

[109] Fred Fairbrother and Alfred E Stubbs. "Studies in Electro-endosmosis.Part IV. The "Bubble-tube" Method of Measurement." In: *Journal of the Chemical Society (Resumed)* (1935), pp. 527–529.

[110] Taylor. "Deposition of a viscous fluid on the wall of a tube." In: *Journal of Fluid Mechanics* 10.02 (1961), pp. 161–165.

[111] Bretherton. "The motion of long bubbles in tubes." In: *Journal of Fluid Mechanics* 10.02 (1961), pp. 166–188.

[112] J. Havre, K.O. Stornes, and H. Stray. "Taming slug flow in pipelines". In: *ABB Review* 4 (2000), pp. 55–63.

[113] F. Di Meglio. "Dynamics and control of slugging in oil production". PhD thesis. Ecole Nationale supérieure des mines de Paris, 2011.

[114] Roland Lenormand, Cesar Zarcone, and A Sarr. "Mechanisms of the displacement of one fluid by another in a network of capillary ducts." In: *Journal of Fluid Mechanics* 135 (1983), pp. 337–353.

[115] G.J. Hisaraki and J.B. Lawson. "Mechanisms of foam flow in porous media: apparent viscosity in smooth capillaries". In: *Soc. Petr. Eng. J.* 25.2 (1985), pp. 176–190.

[116] Madalena M Dias and Alkiviades C Payatakes. "Network models for two-phase flow in porous media Part 1. Immiscible microdisplacement of non-wetting fluids." In: *Journal of Fluid Mechanics* 164 (1986), pp. 305–336.

[117] Jan Stark and Michael Manga. "The motion of long bubbles in a network of tubes." In: *Transport in Porous Media* 40.2 (2000), pp. 201–218.

[118] Axel Gunther et al. "Transport and reaction in microscale segmented gas-liquid flow." In: *Lab on a Chip* 4.4 (2004), pp. 278–286.

[119] Nora Assmann and Philipp Rudolf von Rohr. "Extraction in microreactors: intensification by adding an inert gas phase." In: *Chemical Engineering and Processing: Process Intensification* 50.8 (2011), pp. 822–827.

[120] Agnieszka Ladosz, Eugen Rigger, and Philipp Rudolf von Rohr. "Pressure drop of three-phase liquid-liquid-gas slug flow in round microchannels." In: *Microfluidics and Nanofluidics* 20.3 (2016), pp. 1–14.

[121] EJ Burger and P Macklem. "Airway closure: demonstration by breathing 100 percent O2 at low lung volumes and by N2 washout." In: *Journal of applied physiology* 25.2 (1968), pp. 139–148.

[122] JM Hughes, DY Rosenzweig, and P Bo Kivitz. "Site of airway closure in excised dog lungs: histologic demonstration." In: *Journal of Applied Physiology* 29.3 (1970), pp. 340–344.

[123] Earle B Weiss et al. "Acute respiratory failure in chronic obstructive pulmonary disease: Part I: Pathology". In: *Disease-a-Month* 15.11 (1969), pp. 1–58.

[124] M Griese, P Birrer, and A Demirsoy. "Pulmonary surfactant in cystic fibrosis". In: *European Respiratory Journal* 10.9 (1997), pp. 1983–1988.

[125] Sarah M Wright et al. "Altered airway surfactant phospholipid composition and reduced lung function in asthma." In: *Journal of Applied Physiology* 89.4 (2000), pp. 1283–1292.

[126] Jens M Hohlfeld. "The role of surfactant in asthma". In: *Respiratory research* 3.1 (2001), p. 4.

[127] J.P. White and M. Heil. "Three dimensional instabilities of liquid-lined elastic tubes: a thin film fluid-structure interaction model". In: *J. Fluid Mech.* (2005), p. 031506.

[128] A Van't Veen et al. "Lung distribution of intratracheally instilled Tc-99m-tobramycin-surfactant mixture in rats with a Klebsiella pneumoniae lung infection". In: *ACP-Applied Cardiopulmonary Pathophysiology* 7.2 (1998), pp. 87–94.

[129] Melissa Barber and Carol J Blaisdell. "Respiratory causes of infant mortality: progress and challenges." In: *American journal of perinatology* 27.07 (2010), pp. 549–558.

[130] C.-W. Park and G.M. Homsy. "Two-phase displacement in hele shaw cells: theory". In: *J. Fluid Mech.* 139 (1984), pp. 291–308.

[131] Richard L Hoffman. "A study of the advancing interface. I. Interface shape in liquid-gas systems." In: *Journal of colloid and interface science* 50.2 (1975), pp. 228–241.

[132] LH Tanner. "The spreading of silicone oil drops on horizontal surfaces." In: *Journal of Physics D: Applied Physics* 12.9 (1979), p. 1473.

[133] Pascale Aussillous and David Quéré. "Quick deposition of a fluid on the wall of a tube." In: *Physics of Fluids (1994-present)* 12.10 (2000), pp. 2367–2371.

[134] E. Klaseboer, R. Gupta, and R. Macina. "An extended Bretherton model for long Taylor bubbles at moderate capillary numbers". In: *Phys. Fluids* 26.3 (2014), p. 032107.

[135] S.L. Waters and J.B. Grotberg. "The propagation of a surfactant laden liquid plug in a capillary tube". In: *Phys. Fluids* 471 (2002).

[136] O.E. Jensen. "Draining collars and lenses in liquid-lines vertical tubes". In: *J. Coll. Interf. Sci.* 221 (2000), pp. 38–49.

[137] Rachid Chebbi. "Deformation of advancing gas-liquid interfaces in capillary tubes." In: *Journal of colloid and interface science* 265.1 (2003), pp. 166–173.

[138] H. Wong, C.J. Radke, and S. Morris. "The motion of long bubbles in polygonal capillaries. Part 1. Thin films". In: *J. Fluid Mech.* 292 (1995), pp. 71–94.

[139] H. Wong, C.J. Radke, and S. Morris. "The motion of long bubbles in polygonal capillaries. Part 2. Drag, fluid pressure and fluid flow". In: *J. Fluid Mech.* 292 (1995), pp. 95–110.

[140] A.L. Hazel and M. Heil. "The steady propagation of a semi-infinite bubble into a tube of elliptical or rectangular cross section". In: *J. Fluid Mech.* 470 (2002), pp. 91–114.

[141] Chaim Gutfinger and John A Tallmadge. "Films of non-Newtonian fluids adhering to flat plates". In: *AIChE Journal* 11.3 (1965), pp. 403–413.

[142] RW Hewson, N Kapur, and PH Gaskell. "A model for film-forming with Newtonian and shear-thinning fluids". In: *Journal of Non-Newtonian Fluid Mechanics* 162.1 (2009), pp. 21–28.

[143] M Jalaal and NJ Balmforth. "Long bubbles in tubes filled with viscoplastic fluid". In: *Journal of Non-Newtonian Fluid Mechanics* 238 (2016), pp. 100–106.

[144] Benoît Laborie et al. "Yield-stress fluid deposition in circular channels". In: *Journal of Fluid Mechanics* 818 (2017), pp. 838–851.

[145] John Ratulowski and Hsueh-Chia Chang. "Transport of gas bubbles in capillaries". In: *Physics of Fluids A: Fluid Dynamics (1989-1993)* 1.10 (1989), pp. 1642–1655.

[146] Donata M Fries, Franz Trachsel, and Philipp Rudolf von Rohr. "Segmented gas-liquid flow characterization in rectangular microchannels". In: *International Journal of Multiphase Flow* 34.12 (2008), pp. 1108–1118.

[147] MJF Warnier et al. "Pressure drop of gas-liquid Taylor flow in round micro-capillaries for low to intermediate Reynolds numbers." In: *Microfluidics and Nanofluidics* 8.1 (2010), pp. 33–45.

[148] Dongeun Huh et al. "Acoustically detectable cellular-level lung injury induced by fluid mechanical stresses in microfluidic airway systems". In: *Proceedings of the National Academy of Sciences* 104.48 (2007), pp. 18886–18891.

[149] Yu Song et al. "The air-liquid flow in a microfluidic airway tree." In: *Medical engineering & physics* 33.7 (2011), pp. 849–856.

[150] Hideki Fujioka and James B Grotberg. "Steady propagation of a liquid plug in a two-dimensional channel". In: *J. Biomech. Eng* 126.5 (2004), pp. 567–577.

[151] Hideki Fujioka, Shuichi Takayama, and James B Grotberg. "Unsteady propagation of a liquid plug in a liquid-lined straight tube." In: *Physics of Fluids (1994-present)* 20.6 (2008), p. 062104.

[152] B.L. Vaughan Jr and J.B. Grotberg. "Splitting of a two dimensional liquid plug at an airway bifurcation". In: *J. Fluid Mech.* 793 (2016), pp. 1–20.

[153] Michiel T Kreutzer et al. "Inertial and interfacial effects on pressure drop of Taylor flow in capillaries." In: *AIChE Journal* 51.9 (2005), pp. 2428–2440.

[154] Duong A Hoang et al. "Benchmark numerical simulations of segmented two-phase flows in microchannels using the Volume of Fluid method". In: *Computers & Fluids* 86 (2013), pp. 28–36.

[155] José Bico and David Quéré. "Falling slugs". In: *Journal of colloid and interface science* 243.1 (2001), pp. 262–264.

[156] P.G. Saffman and G. Taylor. "The penetration of a fluid into a porous medium or Hele-Shaw cell containing a more viscous liquid". In: *Proceedings of the Royal Society of London A: Mathematical, Physical and Engineering Sciences*. Vol. 245. 1242. P. R. Soc. Lond. A-Conta. 1958, pp. 312–329.

[157] M.H. Jensen et al. "Effect of gravity on the Saffman-Taylor meniscus: Theory and experiment". In: *Phys. Rev. A* 35.5 (1987), p. 2221.

[158] W.B. Kolb and R.L. Cerro. "Coating the inside of a capillary of square cross section". In: *Chem. Eng. Sci.* 46.9 (1991), pp. 2181–2195.

[159] T.C. Thulasidas, M.A. Abraham, and R.L. Cerro. "Bubble-train flow in capillaries of circular and square cross section". In: *Chem. Eng. Sci.* 50.2 (1995), pp. 183–199.

[160] A. De Lozàr, A.L. Hazel, and A. Juel. "Scaling properties of coating flows in rectangular channels". In: *Phys. Rev. Lett.* 99.23 (2007), p. 234501.

[161] A. De Lozàr, A. Juel, and A.L. Hazel. "The steady propagation of an air finger into a rectangular tube". In: *J. Fluid Mech.* 614 (2008), pp. 173–195.

[162] Youngbae Han and Naoki Shikazono. "Measurement of liquid film thickness in micro square channel". In: *International Journal of Multiphase Flow* 35.10 (2009), pp. 896–903.

[163] Youngbae Han, Naoki Shikazono, and Nobuhide Kasagi. "Measurement of liquid film thickness in a micro parallel channel with interferometer and laser focus displacement meter". In: *International Journal of Multiphase Flow* 37.1 (2011), pp. 36–45.

[164] David C Duffy et al. "Rapid prototyping of microfluidic systems in poly (dimethylsiloxane)". In: *Anal. Chem.* 70.23 (1998), pp. 4974–4984.

[165] Stephen R Quake and Axel Scherer. "From micro-to nanofabrication with soft materials". In: *Science* 290.5496 (2000), pp. 1536–1540.

[166] Janelle R Anderson et al. "Fabrication of microfluidic systems in poly (dimethylsiloxane)". In: *Electrophoresis* 21.1 (2000), pp. 27–40.

[167] S. SigneMamba et al. "Dynamics of a liquid plug in a capillary tube under cyclic forcing: memory effect and airway reopening". In: *J. Fluid Mech. (submitted)* (2017).

[168] Alberto de Lózar et al. "Tube geometry can force switchlike transitions in the behavior of propagating bubbles". In: *Physics of Fluids* 21.10 (2009), p. 101702.

[169] J.N. Lee, C. Park, and G.M. Whitesides. "Solvent compatibility of poly (dimethylsiloxane)-based microfluidic devices". In: *Anal. Chem.* 75.23 (2003), pp. 6544–6554.

[170] F White. *Fluid Mechanics. 5th edt*. 2003.

[171] Harris Wong, CJ Radke, and S Morris. "The motion of long bubbles in polygonal capillaries. Part 1. Thin films." In: *Journal of Fluid Mechanics* 292 (1995), pp. 71–94.

[172] Cédric P Ody, Charles N Baroud, and Emmanuel De Langre. "Transport of wetting liquid plugs in bifurcating microfluidic channels." In: *Journal of colloid and interface science* 308.1 (2007), pp. 231–238.

[173] M.T. Kreutzer et al. "Multiphase monolith reactors: chemical reaction engineering of segmented flow in microchannels". In: *Chem. Eng. Sci.* 60.22 (2005), pp. 5895–5916.

[174] Nadia Vertti-Quintero et al. "Behavior of liquid plugs at bifurcations in a microfluidic tree network". In: *Biomicrofluidics* 6.3 (2012), p. 034105.

[175] Wilfried Engl et al. "Droplet traffic at a simple junction at low capillary numbers". In: *Physical review letters* 95.20 (2005), p. 208304.

[176] Nicolas Champagne et al. "Traffic jams and intermittent flows in microfluidic networks". In: *Physical review letters* 105.4 (2010), p. 044502.

[177] S Bohn et al. "Constitutive property of the local organization of leaf venation networks". In: *Physical Review E* 65.6 (2002), p. 061914.

[178] FF Espinosa and RD Kamm. "Bolus dispersal through the lungs in surfactant replacement therapy". In: *Journal of Applied Physiology* 86.1 (1999), pp. 391–410.

[179] Andres J Calderon et al. "A boundary element model of the transport of a semi-infinite bubble through a microvessel bifurcation". In: *Physics of Fluids* 22.6 (2010), p. 061902.

[180] Jinho Kim et al. "Targeted delivery of liquid microvolumes into the lung". In: *Proceedings of the National Academy of Sciences* 112.37 (2015), pp. 11530–11535.

[181] Peter S Stewart and Oliver E Jensen. "Patterns of recruitment and injury in a heterogeneous airway network model". In: *Journal of The Royal Society Interface* 12.111 (2015), p. 20150523.

[182] KJ Cassidy, N Gavriely, and JB Grotberg. "Liquid plug flow in straight and bifurcating tubes." In: *Journal of biomechanical engineering* 123.6 (2001), pp. 580–589.

[183] Charles N Baroud, Sedina Tsikata, and Matthias Heil. "The propagation of low-viscosity fingers into fluid-filled branching networks". In: *Journal of Fluid Mechanics* 546 (2006), pp. 285–294.

[184] Arnab Majumdar et al. "Fluid transport in branched structures with temporary closures: A model for quasistatic lung inflation". In: *Physical Review E* 67.3 (2003), p. 031912.

[185] Helen Song, Joshua D Tice, and Rustem F Ismagilov. "A microfluidic system for controlling reaction networks in time." In: *Angewandte Chemie* 115.7 (2003), pp. 792–796.

Communications

Dynamics of a liquid plug in a capillary tube under cyclic forcing: memory effects and airway reopening.

S. Signé Mamba, J.C. Magniez, F. Zoueshtiagh, M. Baudoin

Accepted for publication in J. Fluid. Mech (November 2017)

Pressure-driven dynamics of liquid plugs in rectangular micro-channels: influence of the transition between static and dynamic film deposition regimes.

S. Signé Mamba, F. Zoueshtiagh, M. Baudoin

Submitted to Int. J. Multiph. Flow (January 2018)

The dynamics of liquid plugs in synthetic networks under cyclic forcings: towards understanding and treatment of respiratory diseases

Abstract

Breathing is one of the most vital mechanism for humans. Indeed, one can live a few days without eating or drinking, but only few minutes without breathing. Owing to the complexity of the respiratory system, the mechanism of breathing is not well understood, especially in pathological conditions when airways are obstructed by mucus. The presence of liquid plugs resulting from the accumulation of mucus in the bronchial tree is a characteristic of genetic diseases like cystic fibrosis or chronic diseases like asthma or chronic bronchitis. Thus, understanding the dynamics of these plugs during the breathing cycle is essential to improve our understanding of those diseases. In this thesis, we study experimentally and theoretically, the dynamics and rupture of liquid plugs under unidirectional and cyclic forcing in a rigid capillary tube. We develop a reduced dimension model, which quantitatively reproduces the observed dynamics, unveil the underlying physics and in particular the sources of the plug instability leading to its rupture. From this model, we are able to derive the critical pressure magnitude required to reopen obstructed pathways. In addition to the study of cylindrical tubes, we investigated the cyclic dynamics of liquid plugs in rectangular channels, a geometry of the utmost interest for microfluidic systems. In this case, we show that under cyclic pressure forcing, two regimes can be observed depending on the values of the capillary number: one leading to the rupture of the plug and one to stable cyclic oscillations. Finally, in the last part of this work, we study experimentally the cyclic forcing of liquid plugs in tree structures mimicking the geometry of intermediate generation of the lung. These preliminary results show that plugs not ruptured during the first half cycle persist in the airways for a long time and oscillate until their rupture. To conclude, we must underline that the initial objective of this thesis was not to achieve a realistic description of pathological flows in the lungs, but only to develop some fundamental solid building blocks that might contribute to this goal in the future.

Keywords: two phase flow, cyclic forcings, taylor flow, slug, bolus, capillary tube, synthetic networks, airways reopening

---

IEMN
Laboratoire central – Cité scientifique - Avenue Poincaré – CS 60069 – 59652 Villeneuve d Asca Cedex – France

De la dynamique de bouchons liquides dans les réseaux synthétiques soumis à des forçages cycliques au diagnostic et traitement de maladies respiratoires

Résumé

La respiration est un mécanisme essentiel de survie chez les humains. En effet, si nous pouvons survivre quelques jours sans manger et boire, nous ne pouvons survivre que quelques minutes sans respirer. Le système respiratoire est extrêmement complexe de par sa structure fractale qui induit des physiques très différentes entre les voies proximales et distales. Il n'existe à l'heure actuelle aucune modélisation réaliste du système pulmonaire en particulier dans des conditions pathologiques où les voies sont obstruées par des bouchons de mucus. Ces bouchons liquides caractéristiques de certaines maladies comme la mucoviscidose, les bronchites chroniques ou l'asthme résultent de l'accumulation de mucus dans les voies pulmonaires. Comprendre les mécanismes à l'œuvre lors de l'écoulement de ces bouchons lors d'un cycle respiratoire est donc primordial pour améliorer notre compréhension et le traitement de ces pathologies. Nous présentons dans cette thèse une première étude théorique et expérimentale de la dynamique de ces bouchons liquides dans des tubes capillaires rigides soumis à des forçages unidirectionnels et cycliques. Nous avons développé au cours de ce travail un modèle simplifié permettant de reproduire quantitativement les dynamiques observées, de comprendre la physique sous-jacente et en particulier d'identifier les sources d'instabilités qui entraînent la rupture d'un pont liquide. Ce modèle nous a permis de déterminer les pressions critiques nécessaires à la réouverture des voies pulmonaires. Ensuite, nous nous sommes intéressés à la dynamique des ponts liquides dans des tubes rectangulaires, la géométrie la plus communément rencontrée en microfluidique. Dans cette géométrie, nous avons identifié de nouveaux régimes qui n'apparaissent pas dans les géométries cylindriques, et en particulier un régime d'oscillation stable sous forçage en pression périodique. Enfin nous nous sommes intéressés à la dynamique cyclique de ponts liquides dans des réseaux synthétiques en arbres. Nos premiers résultats montrent que les ponts qui ne sont pas détruits lors du premier demi-cycle persistent très longtemps dans les voies et oscillent de manière cyclique dans une génération jusqu'à leur rupture. Pour conclure il est important de souligner que l'objectif initial de cette thèse n'était pas d'aboutir à une modélisation réaliste des écoulements pulmonaires dans des conditions pathologiques, mais simplement d'apporter des briques fondamentales solides qui pourraient y contribuer dans le futur.

Mots clés : écoulement diphasiques, forçages périodiques, bouchons liquides, bolus, tubes capillaires, réseaux synthétiques, réouverture des voies respiratoires

Résumé de la thèse en français

Ce travail de thèse s'inscrit dans un projet qui vise une modélisation réaliste des écoulements pulmonaires en particulier dans des conditions pathologiques où les voies respiratoires sont obstruées par des bouchons (ponts) de mucus. Pour comprendre ces écoulements et construire des modèles qui se rapprochent des conditions physiologiques, il est nécessaire de tenir compte des interactions complexes entre l'air qui s'écoule dans les voies respiratoires pendant la respiration, le fluide (mucus) qui recouvre les parois du poumon et les parois pulmonaires pendant le cycle respiratoire.

L'objectif du travail présenté dans cette thèse est l'étude des mécanismes physiques à l'œuvre lors de l'écoulement de ces bouchons de mucus pendant les cycles respiratoires afin d'améliorer notre compréhension des phénomènes et les traitements liés à ces pathologies.

Introduction générale

Le système respiratoire humain est un système biologique formé de 3 grandes parties : (i) les poumons (droit et gauche) que l'on retrouve dans la cavité thoracique, (ii) les voies respiratoires, comprenant le nez, la bouche, le larynx, le pharynx, les bronches et les bronchioles et (iii) les muscles respiratoires dont le rôle principal est tenu par le diaphragme [1]. Ce système complexe formé d'organes, de muscles et de tissus est essentiellement utilisé pour les échanges gazeux mais joue également un rôle fondamental dans la métabolisation de composés physiologiques, le filtrage de l'air et agit comme un réservoir pour le sang [4, 5]. Les échanges gazeux au cours desquels le dioxygène O_2 est absorbé et le dioxyde de carbone CO_2 est rejeté par les poumons ne sont possibles que par la respiration qui consiste en des cycles répétés d'inspirations et d'expirations de l'air par le nez jusqu'à environ 500 millions de petits sacs alvéolaires à une fréquence de 12 à 18 respirations par minute [2] : il constitue donc un processus cyclique qui se produit dans les voies respiratoires.

L'inspiration est un phénomène actif qui commence par la contraction du diaphragme d'environ $1-1.5cm$, ce qui augmente le volume de la cage thoracique

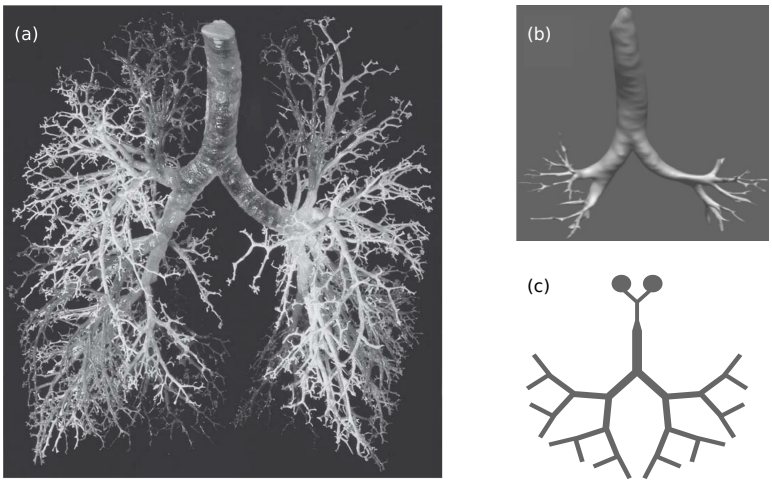

Figure 4.8 – Géométrie d'un poumon humain:
a) Moule d'un poumon humain. Les alvéoles ont été retirées pour pouvoir observer les voies respiratoires [2].
b) Reconstruction 3D de 5 générations du poumon d'une femme utilisée pour des simulations [3].
c) Modèle symétrique fractal 2D fait en PDMS de 5 générations d'un poumon utilisé pour des expériences.

$250 - 350cm^3$. Cette augmentation de volume entraîne une diminution de la pression d'écoulement d'air entre le nez et les alvéoles pulmonaires (pression alvéolaire) en dessous de la pression de référence dans le poumon qui est la pression atmosphérique à cause de la loi de Boyle ($PV = cst$) : ce qui engendre un écoulement d'air vers les poumons jusqu'à ce que les pressions s'égalisent à la fin de l'inspiration. L'expiration est au contraire un phénomène passif au cours duquel les muscles de respiration se relaxent et l'air maintenant chargé en dioxyde de carbone est expulsé du poumon [2].

Les voies respiratoires du poumon qui sont le lieu de passage de l'air et d'échanges gazeux, consistent en un réseau de tubes de différentes tailles et propriétés mécaniques, interconnectés et qui adoptent une structure en arbre (Fig. 4.8). Ces voies pulmonaires sont recouvertes d'une double couche de liquide (mucus non Newtonien au-dessus d'une couche Newtonienne) ayant un rôle de protection contre les particules extérieures qui sont inhalées lors de la respiration et qui peuvent s'avérer dangereuses si elles sont en contact avec les parois du poumon [25]. Ce mucus est ensuite transporté par le mouvement coordonné de cils pulmonaires à une vitesse $\sim 3mm.min^{-1}$ jusqu'à l'estomac où il sera détruit.

Cette fine couche de mucus qui, dans un poumon sain est repartie de façon

uniforme le long des parois pulmonaires adopte un comportement différent dans des conditions pathologiques telles que : (i) l'asthme [58, 35, 59, 60], la mucoviscidose [61, 62, 28], (iii) les bronchites chroniques [32, 58, 63] ou encore (iv) le cancer du poumon. Ce comportement anormal du mucus peut se traduire par une hypersécrétion de mucus ou encore un mucus aux propriétés rhéologiques altérées qui offre un environnement de choix pour la prolifération des bactéries (Fig. 4.9). Ce mucus pathologique qui obstrue les voies respiratoires entrave la circulation de l'air dans l'arbre pulmonaire et peut mener à la mort des sujets malades à cause d'une insuffisance respiratoire.

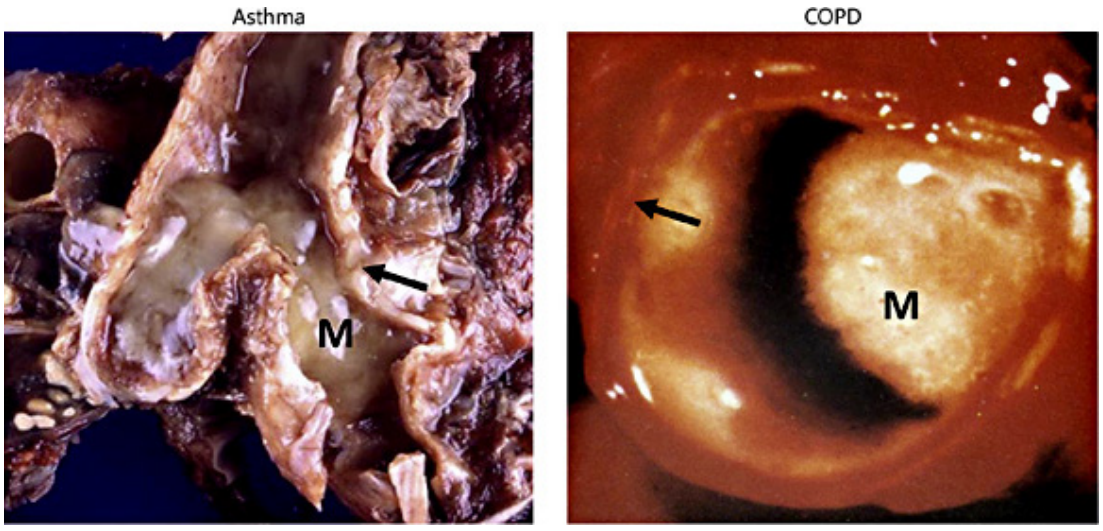

Figure 4.9 – Production de mucus dans le cas de l'asthme et d'une bronchite chronique. L'excès de mucus M bloque partiellement la voie respiratoire [26].

La problématique de la réouverture des voies aériennes est critique pour les patients souffrant d'obstruction des voies respiratoires. Dans la littérature, plusieurs modèles ont été développés pour étudier la réouverture des voies respiratoires dans des tubes rigides secs [96] et prémouillés [97]. En prenant en compte l'élasticité des parois pulmonaires [103, 104, 102, 105, 106], les effets de la gravité de l'inertie [93], ou encore les propriétés non Newtoniennes du mucus [108, 100] mais toujours en utilisant des conditions de forçages (débit ou pression) constantes.

Ce travail de thèse est motivé par l'absence dans la littérature d'études sur la dynamique de ponts liquides soumis à des conditions de forçages complexes. Ainsi nous visons au travers des études menées dans ce manuscrit une meilleure compréhension théorique et expérimentale de la dynamique de l'écoulement et de la rupture des ponts liquides soumis à un forçage cyclique à une fréquence proche d'un cycle respiratoire réel.

IEMN
Laboratoire central – Cité scientifique - Avenue Poincaré – CS 60069 – 59652 Villeneuve d Asca Cedex – France

Dans le chapitre 1, nous proposons une étude théorique et expérimentale de la dynamique des ponts liquides soumis à des forçages cycliques (débit et pression) dans des tubes capillaires cylindriques en verre. Cette étude nous a permis d'identifier les sources d'instabilités qui entraînent la rupture d'un pont liquide.

Le chapitre 2 complète l'étude précédente par une étude numérique qui nous a permis de déterminer les pressions critiques nécessaires à la réouverture des voies pulmonaires obstruées.

Avec le chapitre 3, nous explorons la dynamique cyclique des ponts liquides dans des canaux rectangulaires qui est la géométrie la plus communément rencontrée en microfluidique. Nous montrons que la transition entre 2 régimes de dépôts de films liquides due à la forme polygonale des canaux modifie dramatiquement la dynamique des ponts liquides.

Enfin nous présentons dans le chapitre 4 une étude préliminaire sur la dynamique des ponts liquides dans des réseaux en arbres soumis à des forçages cycliques de différentes amplitudes. Plusieurs régimes d'écoulement sont observés en fonction de l'amplitude de forçage et de la géométrie du réseau. Ces résultats montrent que les ponts liquides qui ne sont pas détruits lors du premier cycle ont tendance à persister dans l'arbre pulmonaire et osciller jusqu'à leurs ruptures.

Chapitre 1 : Dynamique d'un pont liquide dans un tube capillaire soumis à un forçage cyclique

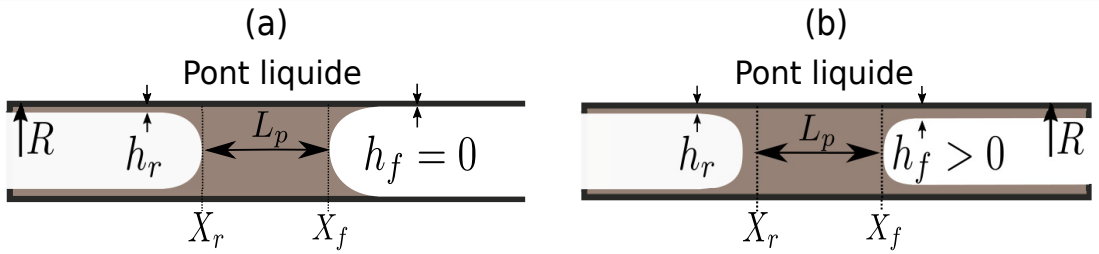

Figure 4.10 – Un pont liquide de longueur L_p est créé à l'intérieur d'un tube capillaire de rayon R. X_r et X_f sont respectivement les positions des ménisques arrière et avant. La couche de liquide déposée lors du mouvement du pont liquide est h_r :
(a) Le tube capillaire est sec $h_f = 0$.
(b) Le tube capillaire est prémouillé $h_f > 0$.

Un pont liquide initialement créé à l'intérieur d'un tube capillaire et qui se déplace sous l'action d'un forçage unidirectionnel déforme ses interfaces (ménisques) avant et arrière. Cette déformation qui se produit au niveau des parois du capillaire conduit à des sauts de pressions à l'avant et à l'arrière du pont liquide ce qui entraîne un dépôt de film liquide sur les parois du tube pendant le mouvement (Fig. 4.10).

Dans cette partie, nous étudions théoriquement et expérimentalement la réponse d'un pont de liquide à un forçage cyclique en pression et en débit de période ($2T = 4$ s). Les expériences sont menées dans des tubes capillaires rigides en verre et comparées à un modèle théorique étendu basé sur les développements précédents [96, 97]. Il est montré qu'en fonction du type de forçage, la dynamique du pont liquide peut être soit périodique avec la reproduction du même mouvement cyclique dans le temps (en débit), soit accélératrice conduisant éventuellement à la rupture du bouchon (en pression) . En particulier, cette étude révèle le rôle hystérétique central joué par le dépôt de film liquide sur la dynamique du pont liquide.

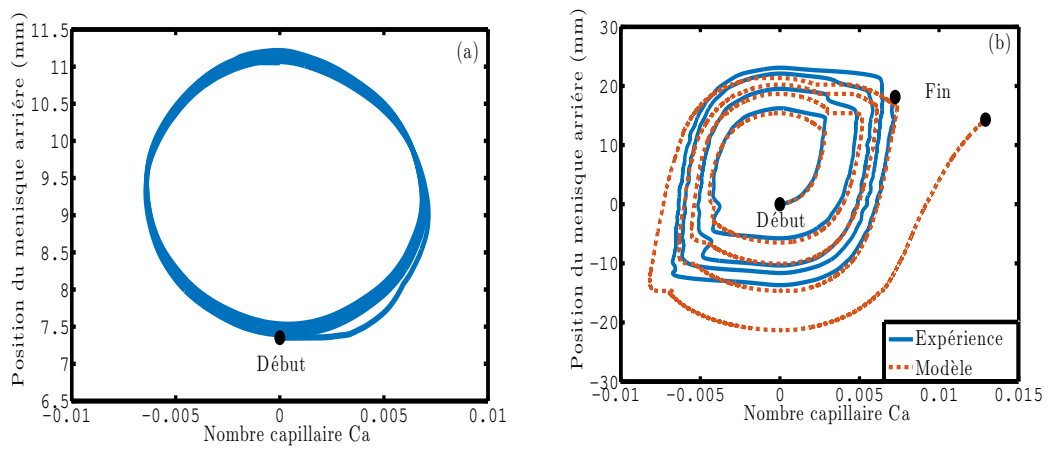

Figure 4.11 – Portait de phase montrant l'évolution de la position du ménisque arrière du pont liquide en fonction de la vitesse adimensionnée (le nombre capillaire Ca) :
(a) Forçage cyclique en débit.
(b) Forçage cyclique en pression.
Les courbes en bleu représentent les expériences tandis que les courbes en rouge représentent les simulations.

La différence observée dans la dynamique du pont liquide soumis à un forçage en débit et en pression s'explique par la nature même de la contrainte appliquée. En effet pour un forçage cyclique en débit, (i) la vitesse du pont

IEMN
Laboratoire central – Cité scientifique - Avenue Poincaré – CS 60069 – 59652 Villeneuve d Asca Cedex – France

liquide et sa position sont directement imposées par le mouvement du pousse seringue et ne dépendent pas de la résistance du pont liquide et (ii) le film de liquide déposé sur les parois du tube est constant parce qu'il ne dépend que de la vitesse. Ce qui conduit à un bilan massique nul et donc une évolution périodique du pont liquide à chaque cycle (Fig. 4.11a).

Dans le cas d'un forçage cyclique en pression, la dynamique du pont liquide diffère fondamentalement (Fig. 4.11b). L'explication de cette modification se situe dans l'existence de deux effets mémoires qui modifient l'évolution des résistances à chaque cycle : (i) Un effet mémoire lié à une réduction cyclique de la longueur du pont liquide qui à son tour diminue la résistance visqueuse et (ii) un deuxième effet lié à la lubrification du tube après chaque passage du pont liquide ($h_f > 0$) qui réduit la résistance de l'interface avant. Ces effets mémoires dépendent fortement de la mémoire du film liquide déposé lors de chaque déplacement dans le cycle (Fig. 4.12).

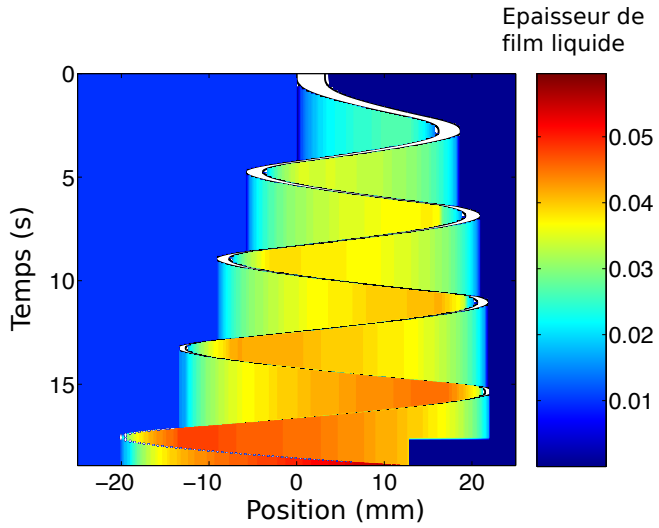

Figure 4.12 – Diagramme spatiotemporel montrant l'évolution de l'épaisseur de film liquide déposé sur les parois obtenu à partir du modèle réduit.

Enfin, la comparaison des données expérimentales avec notre modèle théorique, de la rupture de ponts liquides de tailles différentes soumis à un forçage en pression cyclique démontre l'existence d'une distance de saturation pour la rupture des ponts liquides quelque soit la taille initiale : c'est donc un phénomène limité dans l'espace contrairement à ce qui observé en utilisant un forçage unidirectionnel.

Chapitre 2 : Pressions critiques nécessaires à la réouverture des voies respiratoires

Nous montrons à travers une étude théorique et numérique des pressions critiques nécessaires à la réouverture des voies respiratoires obstruées par des ponts liquides soumis à dans des conditions réalistes de forçage (voir Fig. 4.13), que la dynamique des ponts liquides peut être soit : (i) accélérée associée à une diminution progressive de la taille du pont liquide à chaque cycle menant à la rupture du pont liquide ou (ii) décélérée associée à une croissance de la taille du pont liquide à chaque cycle et une aggravation de la congestion. La transition entre ces deux régimes dépend essentiellement de l'amplitude de la pression de forçage ainsi que de l'épaisseur de film liquide tapissant les voies pulmonaires.

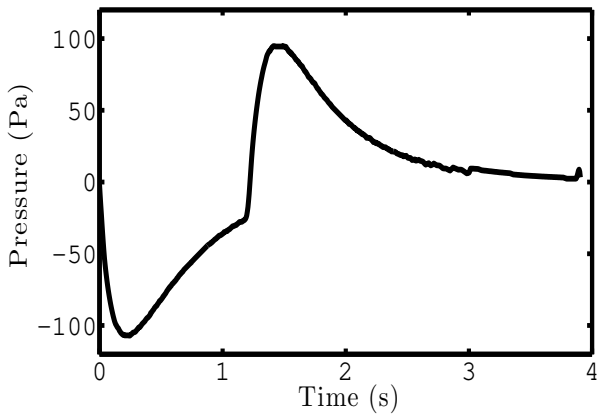

Figure 4.13 – Simulation numérique de la pression alvéolaire obtenue pendant un cycle de respiration normal [8] .

Pour ce faire, nous avons initié une première étude sur la réponse du pont liquide à un forçage en pression variable dans le temps $\Delta\tilde{P}_t = \tilde{P}_0(1 - exp(-\tilde{t}/\tilde{\tau}))$ avec $\tilde{t}$ et $\tilde{\tau}$ respectivement les valeurs du temps et du temps instationnaire. Cette étude nous a permis d'observer trois régimes d'évolution de la dynamique du pont liquide : (i) un régime d'accélération qui apparait pour des amplitudes de pression très supérieures à la pression critique, (ii) un régime de décélération induit pour des amplitudes de pression légèrement supérieures à la pression critique initiale mais qui restent insuffisantes pour parvenir à une accélération du pont liquide et enfin (iii) un régime de décélération pour des amplitudes de pression bien inférieures à la pression critique initiale. Bien que l'existence d'une zone d'évolution instationnaire de la pression rende la prédiction de la

IEMN
Laboratoire central – Cité scientifique - Avenue Poincaré – CS 60069 – 59652 Villeneuve d Asca Cedex – France

transition entre les différents régimes plus complexes, les paramètres clés de transition restent l'amplitude de forçage et l'épaisseur initiale de film liquide.

Le second cas étudié est la réponse du pont liquide soumis à un signal en pression cyclique rectangulaire pour évaluer l'influence du mouvement cyclique. Dans ce cas de figure comme dans le précédant trois régimes sont observés mais toujours avec l'apparition du régime d'accélération pour des amplitudes de pression très supérieures à la pression critique. Par contre, on observe deux autres régimes d'oscillations stables des ponts liquides : (i) un régime d'accélération saturante pour des amplitudes de pression légèrement supérieures à la pression critique et caractérisée dans un premier temps par une diminution de la taille du pont liquide mais qui va tendre une valeur de constance et (ii) un régime de décélération saturante pour des pressions faibles caractérisé par une augmentation de la taille du pont liquide qui va finir par se stabiliser et osciller autour d'une valeur constante comme dans le cas précédent. La différence entre ces deux derniers régimes se situe dans une croissance ou décroissance initiale de la pression critique qui va conduire dans un cas à une taille du pont liquide plus petite que la taille initiale (accélération saturante) ou une taille de pont liquide plus grande que sa taille initiale (décélération saturante).

En combinant les résultats des études précédentes et en utilisant: (i) les données physiologiques du diamètre et la taille des bronches, (ii) la dépendance de la longueur du pont liquide avec l'épaisseur du film liquide et (iii) la variation de l'épaisseur initiale de film liquide pour différents degrés de congestion des voies respiratoires, nous avons étudié la réponse du pont liquide soumis à un forçage réaliste (variable dans le temps et cyclique) présenté à la figure 4.13. Le résultat le plus surprenant est la disparition des régimes de décélération induite et d'accélération saturante qui peut s'expliquer par la forme particulière du signal utilisé. Nous retrouvons toujours les deux régimes : (i) d'accélération conduisant à la rupture du pont liquide et (ii) de décélération associée à une augmentation progressive de la taille du pont liquide à chaque cycle.

Nous montrons également au travers de cette étude le rôle clé joué par l'épaisseur de film liquide qui augmente de façon dramatique les pressions critiques nécessaires à la réouverture des voies respiratoires en particulier dans les dernières générations du poumon.

Dans cette étude nous nous limitons à un cas idéal qui ne prend pas en compte : (i) les propriétés rhéologiques du mucus, (ii) la déformation des parois et leurs effets sur la propagation et la rupture du pont liquide ainsi que (iii) les interactions complexes dues à la géométrie en arbre du poumon. Cependant cette étude est à notre connaissance la première à explorer la réponse des ponts liquides soumis un forçage se rapprochant d'un cycle respiratoire réaliste pour différentes épaisseurs de films liquide et qui permet de déterminer les pressions

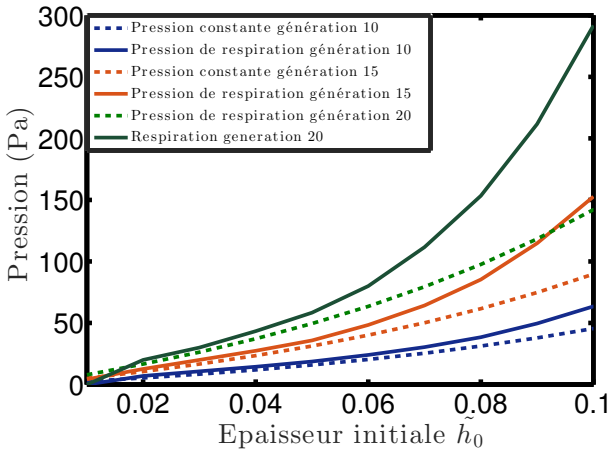

Figure 4.14 – Pression critique de transition entre le régime d'accélération et de décélération en fonction de l'épaisseur de film liquide $\tilde{h_0}$ dans différentes générations de l'arbre pulmonaire. Pointillé: pression alvéolaire et trait solide : pression constante de même amplitude.

critiques nécessaires à la réouverture des voies respiratoires obstruées.

Chapitre 3 : Dynamique d'un pont liquide dans un microcanal rectangulaire soumis à des forçages en pression : Influence de la transition entre le régime de dépôt de film liquide statique et dynamique

La transition entre le régime de dépôt de film liquide statique et dynamique (voir Fig. 4.15) conduit à une accélération dramatique du pont liquide qui mène rapidement à sa rupture. Cette transition de régime est propre aux canaux polygonaux qui présentent des singularités au niveau de leurs bords. Dans cette partie nous étudions l'influence de la transition entre ces deux régimes de dépôt de film liquide sur la dynamique du pont liquide dans un microcanal rectangulaire fait en PDMS à partir des techniques de photolithographie. Le pont liquide est soumis à différents types de forçages en pression (unidirectionnel et cyclique). Les observations expérimentales sont quantitativement recouvrées par un modèle théorique que nous avons développé et qui s'appuie sur des études précédentes.

La première étape de cette étude consiste à déterminer l'influence de la

IEMN
Laboratoire central – Cité scientifique - Avenue Poincaré – CS 60069 – 59652 Villeneuve d Asca Cedex – France

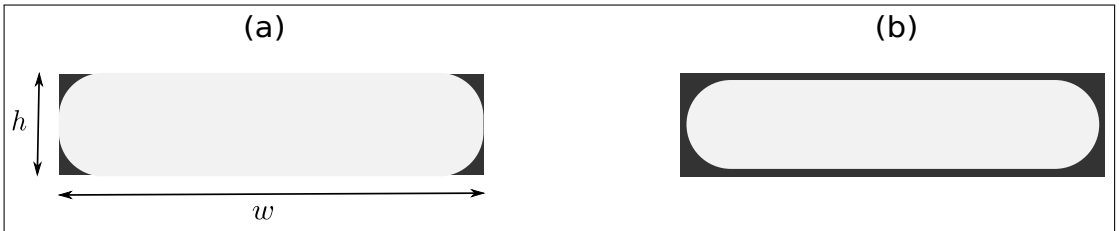

Figure 4.15 – Esquisse de la section de la bulle d'air à l'arrière du pont liquide: (a) Quand la vitesse adimensionnée $Ca \to 0$ (régime de dépôt de film liquide statique).
(b) $Ca \gtrsim Ca_c$ (régime de dépôt de film liquide dynamique).
En noir: liquide, blanc: air.

transition de régime de dépôt de film liquide sur la dynamique des ponts liquides. Pour cela nous avons étudié expérimentalement la propagation et la rupture de ponts liquides dans un canal rectangulaire soumis à des forçages en pression unidirectionnels et d'amplitudes différentes.

Les observations expérimentales confirmées par la notre modèle théorique montrent que dans le régime de dépôt statique, l'évolution du nombre capillaire Ca et de la taille du pont liquide est quasi linéaire à cause du film liquide qui est déposé principalement dans les bords du canal. Cette fraction de liquide est estimée par une valeur constante qui dépend du rapport d'aspect. Dans le régime de dépôt dynamique, la loi de dépôt ne dépend plus seulement du rapport d'aspect, mais aussi du nombre capillaire. Cette rétroaction est à l'origine de l'accélération massive du pont liquide qui conduit à une diminution rapide de sa taille quand le nombre capillaire dépasse le nombre capillaire critique $Ca > Cac$ (voir Fig. 4.16). Ce phénomène rappelle ce qu'on a précédemment observé dans les tubes capillaires où le régime de dépôt statique n'existe pas.

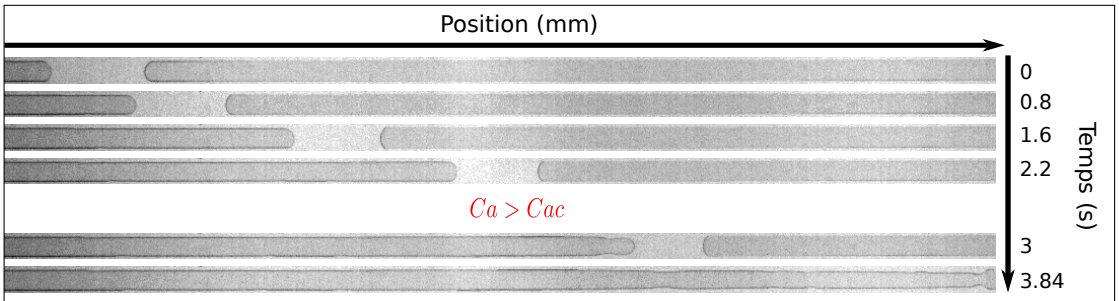

Figure 4.16 – Chronographie montrant l'évolution d'un pont liquide dans un canal rectangulaire soumis à un forçage en pression unidirectionnel de la forme : $\Delta P_t = 1000e^{-3e^{-10t}} Pa$

Dans un deuxième temps, nous avons soumis les ponts liquides à un forçage en pression cyclique. Dans ce cas nous montrons que les ponts liquides vont osciller de façon quasi stable tant qu'ils restent dans le régime statique ($Ca < Cac$) durant le premier cycle. Autrement, les ponts liquides vont accélérer progressivement dans le cycle et finalement casser. À partir de ces observations, nous avons pu dériver une expression théorique de la longueur critique qui nous permet de prédire dans quel régime va principalement évoluer le pont liquide.

Étant donné la difficulté de fabrication de systèmes microfluidiques de section cycliques par exemple des réseaux connectés mimant un arbre pulmonaire, cette étude nous permet d'analyser et de transposer les résultats obtenus de la géométrie rectangulaire vers la géométrie cylindrique et de comprendre la pertinence et les limites d'une telle comparaison.

Chapitre 4 : Dynamique cycliques des ponts liquides dans des réseaux en arbre

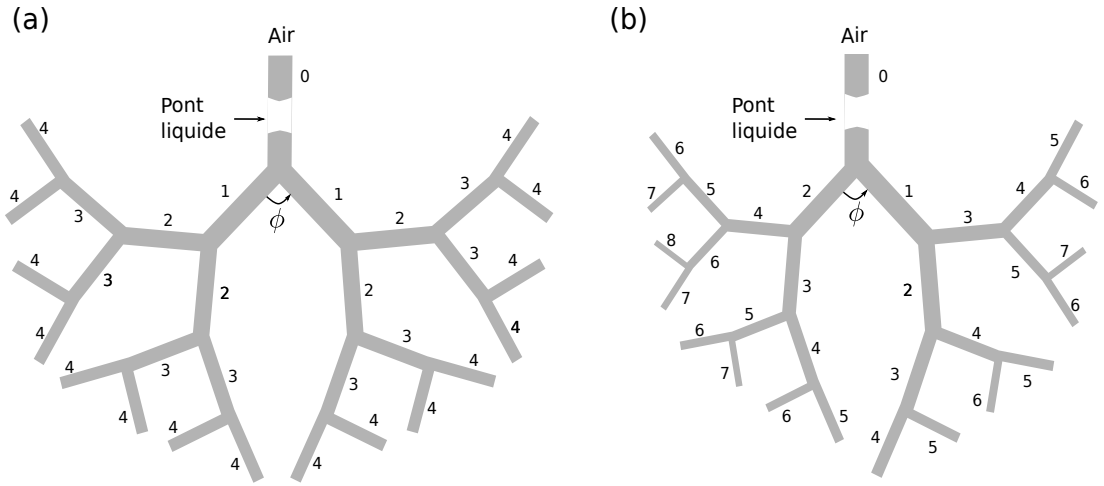

Figure 4.17 – Modèles de 5 générations d'un réseau en arbre obstrués par un pont liquide. La première branche numérotée 0 se divise successivement :
(a) Modèle symétrique : chaque branche dans une génération se divise de façon dichotomique en branches filles successives.
(b) Modèle asymétrique : chaque branche dans une génération donne naissance au 2 branches filles suivantes.

La dynamique des ponts liquides soumis à des forçages cycliques de différentes amplitudes dans des réseaux fractals en arbres (symétrique et asymétrique),

IEMN
Laboratoire central – Cité scientifique - Avenue Poincaré – CS 60069 – 59652 Villeneuve d Asca Cedex – France

nous avons pu identifier trois régimes associés à une diminution de l'amplitude de forçage : (i) un premier régime associé à une amplitude de forçage élevée et dans lequel tous les ponts liquides seront détruits avant d'entrer dans le cycle, (ii) le second régime dans lequel au moins une branche du réseau est réouverte pendant la première demi-période et les autres ponts liquides qui auront survécu vont osciller jusqu'à la rupture et enfin (iii) le troisième régime dans lequel aucun pont liquide ne va casser durant le premier cycle et tous les ponts liquides vont entrer dans le mouvement cyclique. Chacune de ces transitions étant associée à une augmentation spectaculaire du temps de réouverture total du réseau.

En comparant la dynamique des ponts liquides dans les réseaux symétriques et asymétriques, nous observons que les régimes d'évolution sont similaires exceptés le temps de réouverture qui est quasiment doublé dans le réseau asymétrique. Une explication à cela serait la réduction rapide des sections d'une génération à une autre dans l'arbre asymétrique comparé à l'arbre symétrique (voir Fig. 4.17). Ce qui conduit à une évolution plus rapide de la résistance du réseau et ainsi un ralentissement de la propagation des ponts liquides dans le cas asymétrique.

La connaissance du volume réouvert en fonction du temps est d'une importance fondamentale pour les maladies pulmonaires parce qu'elle donne des informations essentielles sur l'évolution des congestions pendant la respiration. Nous avons pu obtenir ces informations en fonction des amplitudes de forçage mais nous n'avons pas eu le temps d'analyser toutes les tendances.

Conclusion

La motivation principale de cette thèse était la compréhension de la dynamique des ponts de mucus durant la respiration : Est ce qu'ils finissent par être détruits ou bien persistent-ils dans l'arbre pulmonaire? Quelle est l'influence de la pression de forçage ou encore de l'épaisseur de mucus sur la dynamique de ces ponts de mucus?

L'étude de la réponse des ponts liquides soumis à des forçages cycliques nous a dévoilé plusieurs phénomènes physiques intéressants : (i) le rôle essentiel de l'histoire du film liquide déposé, (ii) l'existence d'états stables avec des oscillations périodiques de ponts liquides dans les tubes prémouillés, (iii) l'influence de la transition entre le dépôt de film statique et dynamique sur la dynamique des ponts liquides dans les canaux rectangulaires. Nous avons aussi pu mettre en évidence le rôle clé de l'épaisseur de la couche de liquide recouvrant les parois du poumon sur la stabilité des ponts liquides ainsi que la nécessité de pression de forçage plus élevée pour rouvrir les voies respiratoires plus distales.

Ce travail soulève plusieurs questions (quelle est l'influence des propriétés

non Newtoniennes du mucus? peut-on dériver un modèle théorique complet pour le réseau? quelles sont les conditions de forçages réelles dans les branches intermédiaires de l'arbre pulmonaire? quel est le rôle de l'élasticité des parois sur la dynamique des ponts de mucus? ...) et ne fournit que quelques réponses. Cependant, nous espérons que le travail fournit dans cette thèse ajoutera une autre pierre au puzzle complexe que représente les écoulements pulmonaires.

IEMN
Laboratoire central – Cité scientifique - Avenue Poincaré – CS 60069 – 59652 Villeneuve d Asca Cedex – France